The Dissertation Committee for Shriram Sethuraman Certifies that this is the approved version of the following dissertation:

Combined Intravascular Ultrasound and Photoacoustic Imaging

Committee:

Stanislav Y. Emelianov, Supervisor

Salavat R. Aglyamov

Richard W. Smalling

Thomas E. Milner

Xiaojing Zhang

Combined Intravascular Ultrasound and Photoacoustic Imaging

by

Shriram Sethuraman, B.E., M.Sc., M.S.E

Dissertation

Presented to the Faculty of the Graduate School of
The University of Texas at Austin
in Partial Fulfillment
of the Requirements
for the Degree of

Doctor of Philosophy

The University of Texas at Austin
August 2007

Dedication

This dissertation is dedicated to my loving parents, Sethuraman and Banu, my sweet little sister, Sudakshna, and my dearest Nitya.

Acknowledgements

First and foremost, I gratefully thank my parents Sethuraman and Banu and my sister Sudakshna for their never-ending love, support, wisdom and patience. They have stood by me and constantly encouraged me all my life. For being there for me in times of need and encouraging me through the whole process, I thank my best friend Shalu, Ankur and my dearest Nitya.

As a friend, advisor and mentor Dr. Emelianov (Stas) has given me the knowledge, valuable encouragement and guided me through my entire research. His reassurance and excellent mentorship made it easier for me to pursue my goal. Stas has played a major role in shaping my career and has been my guardian away from home. Thank you Stas.

For their countless influential discussions, guidance and mentorship, I thank Salavat and Andrei. The support from my friends and lab mates, Jignesh, Suhyun, Valli, Bo and Mohammad has been invaluable.

I was fortunate to be associated with the collaborative work with Dr. Smalling and his group at University of Texas Medical School at Houston. I thank Jim, Dr. Litovsky, Patty and Cezar for helping me through the animal research studies. I owe special thanks to Dr. Milner for guiding me through my M.S. research as well as being involved in this work as a member of my Ph.D. dissertation committee. For valuable inputs on my thesis and research work, I thank and acknowledge the contributions of Dr. Zhang.

Monetary support through research assistantships, teaching assistantships and the University Continuing Fellowship Award from The University of Texas at Austin has allowed me to concentrate on my research work and helped alleviate any financial burden. I would also like to acknowledge Boston Scientific, Inc. for the supply of catheters.

Support from faculty and staff in the Department of Biomedical Engineering especially from Dr. Schmidt, Dr. Roy, Dr. Welch, Maggi, Ann, Joni, Heidi and Majid was invaluable throughout my graduate studies. I express my gratitude to my lab, department and the university for providing me with all the facilities through my graduate studies.

Finally, my appreciation and thanks go to my family, friends and colleagues who have helped me in the successful completion of my doctoral studies.

Combined Intravascular Ultrasound and Photoacoustic Imaging

Publication No._____________

Shriram Sethuraman, Ph.D.
The University of Texas at Austin, 2007

Supervisor: Stanislav Y. Emelianov

The primary focus of the work was to evaluate the capability of intravascular photoacoustic (IVPA) imaging in combination with intravascular ultrasound (IVUS) to detect and differentiate atherosclerotic plaques. The composition rather than structural narrowing of the arteries is a major indicator of the propensity of a vascular lesion to rupture. Consequently, intravascular imaging of these high-risk plaques is required to exactly determine the vulnerable plaque constituents for appropriate follow-up therapy. Our multi-modality imaging approach aims to utilize the high resolution structural assessment abilities of IVUS and the optical contrast of IVPA imaging and is capable of differentiating the lipid, fibrous and fibro-cellular components of an inflammatory lesion.

To test the hypothesis, we developed an IVUS catheter based laboratory prototype of a combined IVUS/IVPA imaging system. The performance of the synergistic combination of IVUS and IVPA imaging was evaluated through tissue mimicking phantom studies. Further, to test the ability of the combined imaging to detect plaques, excised samples of an aorta were utilized from a specifically designed animal model of atherosclerosis. Ex-vivo IVPA imaging studies were performed using a 532 nm laser

excitation to detect the lipids in the plaque. In addition, multi-wavelength spectroscopic IVPA imaging studies were evaluated to differentiate plaques. Finally, an ultrasound based temperature estimation method was utilized to demonstrate and confirm safety of IVPA imaging for clinical intravascular applications.

Upon analysis of the results of our investigation, we believe that IVPA imaging offer numerous potential advantages when integrated with clinical IVUS imaging. The IVUS imaging system with integrated IVPA imaging capability could play a major role in interventional cardiology.

Table of Contents

List of Tables

List of Figures

Chapter 1: Introduction

1.1 CORONARY HEART DISEASE - SIGNIFICANCE

The cardiovascular system is one of the most important physiological systems performing vital circulatory functions required for the normal functioning of the human body. The major components of the cardiovascular system include, 1) blood, a medium for the transportation of nutrients to and from cells, 2) blood vessels, that provide the channel for blood flow and 3) heart, that pumps and provides the pressure required for the blood flow throughout the body. The pathologies resulting from an abnormal function pose potentially fatal health risks. An example of an abnormality with systemic implications is atherosclerosis – a cardiovascular disease originating in the walls of the arteries. The disease affects major arteries in the human body including the coronary arteries that supply blood and nutrients to the heart muscle.

Coronary heart disease (CHD) includes acute myocardial infarction, acute ischemic (coronary) heart disease, atherosclerotic cardiovascular disease and other forms of chronic ischemic coronary disease. CHD continues to be a public health burden in the United States and comprises more than half of all cardiovascular events in men and women under the age of 75 (Fig. 1.1). In 2004 alone, 1 of every 5 deaths was caused by CHD with a total reported mortality of 650,000 (National Center for Health Statistics). The increase in CHD is also reflected in an enormous increase (334% from 1979 to 2004) in cardiac catheterization procedures. In addition, the disease is a major economic burden; the direct and indirect costs involved with coronary heart disease in 2007 are estimated to be 151.6 billion dollars (Source: National Heart, Lung and Blood Institute) [1]. Therefore, there is an urgent clinical need for imaging techniques to help understand and evaluate the disease, aid in early detection and assist therapy.

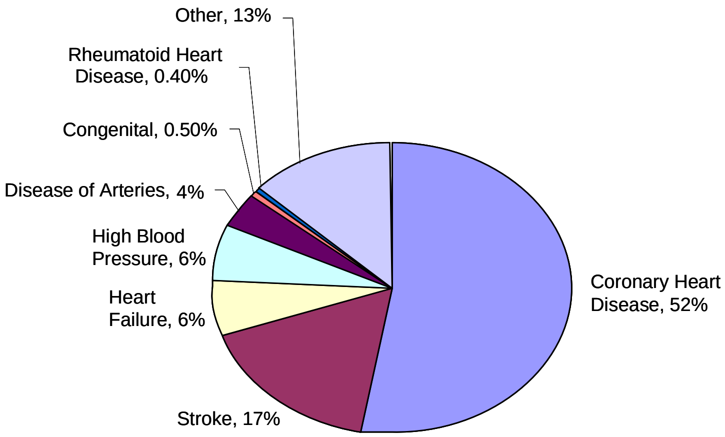

Figure 1.1: Percentage breakdown of deaths from Cardiovascular Disease (United States: 2004) [1].

1.2 ATHEROSCLEROSIS – THE DISEASE

A normal arterial wall contains well-defined layers comprised of cellular elements and an extra cellular matrix [2]. Figure 1.2 illustrates the three distinct layers, intima, tunica media and adventitia demarcated by an internal and external elastic lamina. The innermost layer facing the luminal blood contains a single layer lining of the endothelium. The media is the middle layer containing vascular smooth muscle cells that synthesize the extra cellular matrix. The adventitia is the outmost layer containing smooth muscle cells, collagen and fibrous connective tissue.

A diseased artery on the other hand is accompanied by the deposition of plaques containing predominantly fatty material in the intima. The onset of the disease is characterized by a dysfunction of the endothelium and increase in permeability of the arterial wall to lipoproteins and adhesiveness to monocytes and T lymphocytes. The early lesions known as “fatty streaks” consist of macrophages and T cells embedded in a thin layer of lipids. The inflammatory response responsible for the increase in macrophage foam cells lead to an increase in the thickness of the inner lining of the artery. The lesions with a soft lipid pool, primarily cholesterol, smooth muscle cells and connective tissues covered by a thin fibrous tissue are called the vulnerable plaque [3-7].

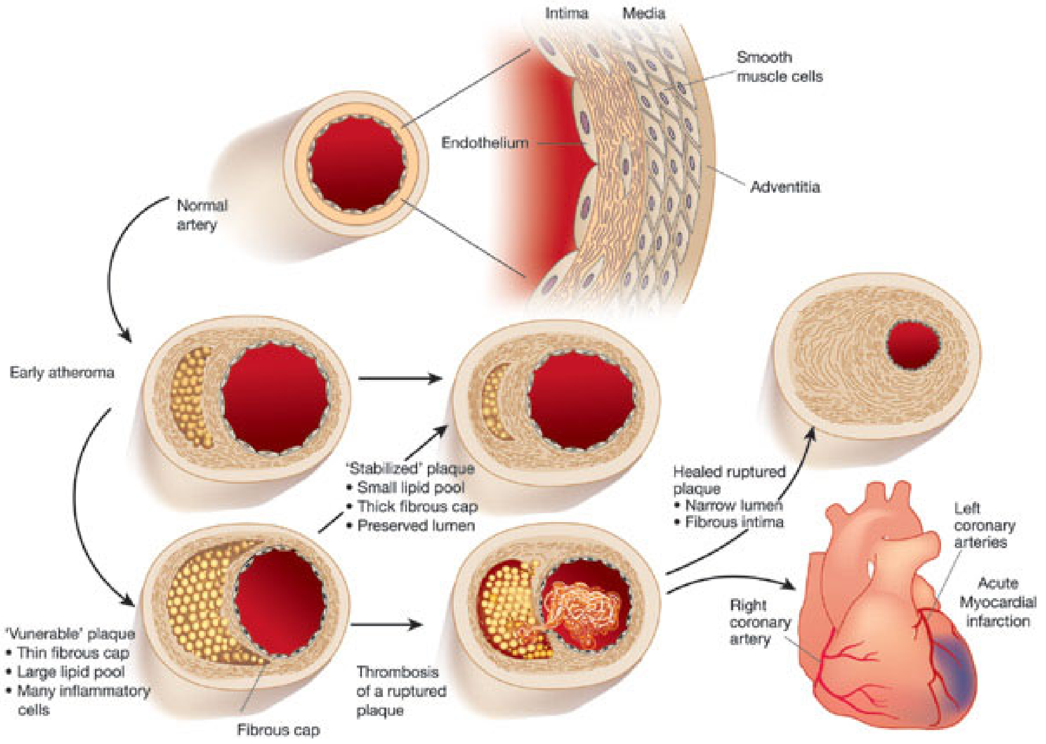

Figure 1.2: Illustration of the process of atherosclerosis. The progression of an early atheroma could lead to either a stabilized plaque or a complicated vulnerable lesion (adapted by permission from Macmillan Publishers Ltd: [Nature] (Libby, P., Inflammation in Atherosclerosis, p. 872, vol. 420) copyright (2002)[8]).

1.3 INFLAMMATION IN ATHEROSCLEROSIS

Atherosclerosis is primarily considered an inflammatory disease in which immune mechanisms interact with metabolic risk factors to initiate, propagate and activate lesions in the artery. Inflammation per se, acute or chronic, is believed to be primarily defensive or protective initiating the process of tissue repair [6, 9]. Inflammatory infiltrates are found in region overlying the plaque and are not found in relation to the normal arterial vessel [10, 11]. The response of monocytes, T-lymphocytes and macrophages to the invading agents governs the stage and progression of plaque growth.

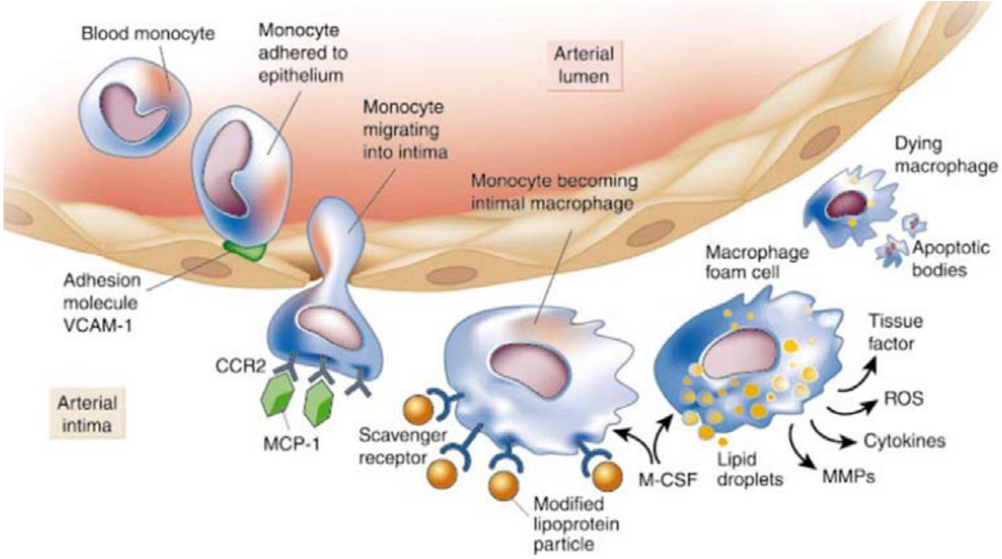

Figure 1.3: Initiation of inflammation (adapted by permission from Macmillan Publishers Ltd: [Nature] (Libby, P., Inflammation in Atherosclerosis, p. 869, vol. 420) copyright (2002) [8]).

1.3.1 Initiation of inflammation by LDL infiltration

The high cholesterol levels in the blood cause focal activation of the endothelium in large and medium sized arteries [12]. At preferential sites guided by high levels of hemodynamic strain, the low density lipoproteins (LDL) infiltrate the arterial wall and subsequently initiates the process of inflammation [13, 14]. In the intima, the LDL is modified either by oxidation or through enzymatic action with the release of phospholipids. The endothelial cells activated by the phospholipids express several types of leukocyte adhesion molecules leading to a surface adhesion of blood cells on the site of activation [15]. The adhesion takes place through a preferential binding of cell specific counter-receptors to the vascular cell adhesion molecule 1 (VCAM-1) [16]. Following adhesion, the chemokines produced in the intima stimulate the migration of the cells into the sub-endothelial space (Fig. 1.3).

1.3.2 Role of Macrophages

The macrophages are produced when the monocytes in the intima differentiate in the presence of cytokines and other growth factors (Fig. 1.3). These macrophage cells are responsible for the destruction of the oxidized LDL and other apoptotic cell fragments. However, the cholesterol derived from the uptake of the oxidized LDL could accumulate in the macrophage cells body and the cell is transformed into a "foam cell". The macrophage foam cells are typical cellular constituents of early plaque development. The toll-receptors also play a major role in activating the macrophages through a signaling cascade to produce inflammatory cytokines, proteases and cytotoxic oxygen and nitrogen radical molecules [17].

1.3.3 T-Cell activation and inflammation

The response of the immune system to the early lesion development may be responsible for promoting inflammation during atherosclerosis. Immune cells such as T cells are almost always present in atherosclerotic lesions. The type 1 helper T (Th1) response activates macrophages and initiates an inflammatory response in defense against intracellular pathogens. Specifically, the cytokines in the lesion promote the Th1 response and activated T cells differentiate into Th1 effector cells [18]. These cytokines are also responsible for producing many inflammatory and cytotoxic molecules in macrophages and vascular cells [12].

1.4 CLASSIFICATION OF ATHEROSCLEROTIC LESIONS

According to the criteria of the American Heart Association Committee on Vascular Lesions, lesion types depend in part on the phase of progression [19]. As illustrated in the Fig. 1.4, the precursor lesion is divided into 3 morphological stages. Type I lesions represent the initial stages with an increase in macrophage infiltration and the appearance of macrophages filled with lipid droplets – foam cells. Type II lesions are visible fatty streaks with layers of macrophage cells and extracellular lipids. Type III (intermediate) lesions are a morphological bridge between the fatty streaks and advanced lesions and are characterized by an intimal thickening and progressive increase in extracellular lipid deposits. These initial stages of plaque are small and clinically silent and could regress back to a normal artery. The advanced lesions constitute the plaque where the fat accumulates and forms a lipid core. In type IV lesions, the fibrous intima may still be intact and the size of the lipid pool may start increasing. Depending on the amount of lipid content, the plaque could also cause luminal constriction. Type V lesions contain rich smooth muscle cells in the intimal cap and the intima thickens with an increase in collagen fibers. The type VI plaque may contain thrombus with significant amount of surface defects. The plaque could regress back to type V with a transformation of hematoma to fibromuscular tissue and a subsequent increase in the thickness of the intimal cap. The reduction in the lipids in the advanced stages and an increase in thick plaque collagen and calcium could lead to stages VII and VIII.

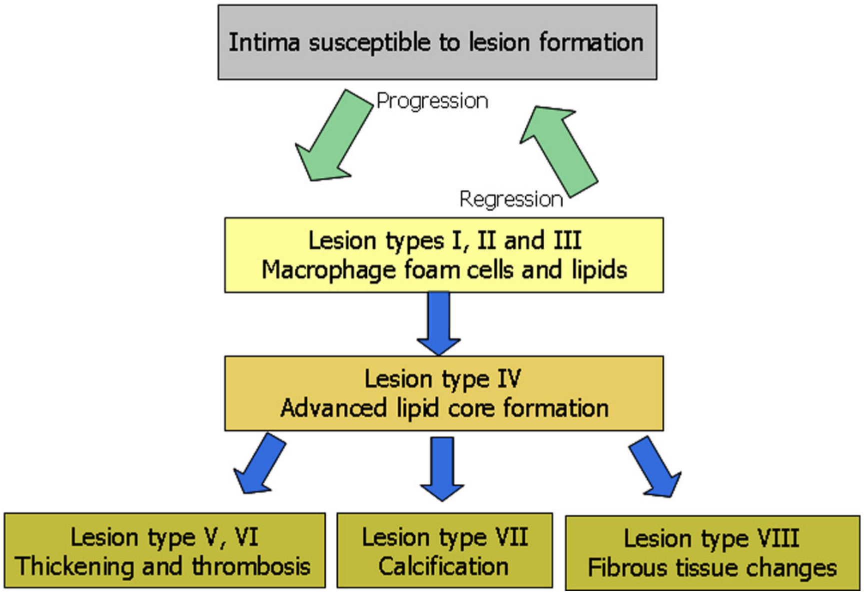

Figure 1.4: Classification of atherosclerotic lesions (adapted from Stary (2000) [20]).

1.5 ATHEROSCLEROSIS – IMAGING AND TREATMENT STRATEGIES

1.5.1 Imaging vulnerable plaque morphology and composition

Results from extensive research on atherosclerosis have helped to identify and classify plaques based on the size and structure of the lumen, pathological genesis of the lesion and molecular composition. Further, the concept of a lesion with a high-risk of rupture, also called vulnerable plaques have gained importance (Fig 1.5). Most, but not all such plaques, have high lipid content and a very thin fibrous cap. However, there are other types of vulnerable plaques containing extensive calcification, inflammation with infiltrating macrophages, endothelial erosion and thrombosis, intra-plaque hemorrhage leading to neo-vascularization and endothelial denudation causing superficial aggregation of red blood cells. Therefore, detection and diagnosis of atherosclerosis would require imaging techniques capable of presenting a comprehensive interrogation of plaque structure as well as composition.

Therefore, there is a need for imaging techniques that possess high resolution capabilities to detect the thin fibrous cap, sufficient contrast to differentiate the lipid core, ability to quantify the calcium score, detect structural changes in the vessel wall and detect macrophage and matrix metalloproteinase (MMP) activity. The success of diagnostic imaging is also measured by the ability to guide therapeutic strategies. Treatment options could depend on the characteristics of vulnerable plaque. Dominant risk factors could occur both at the system and localized level. Therefore, the imaging technique should be capable of identifying multiple instances of the risk for plaque rupture.

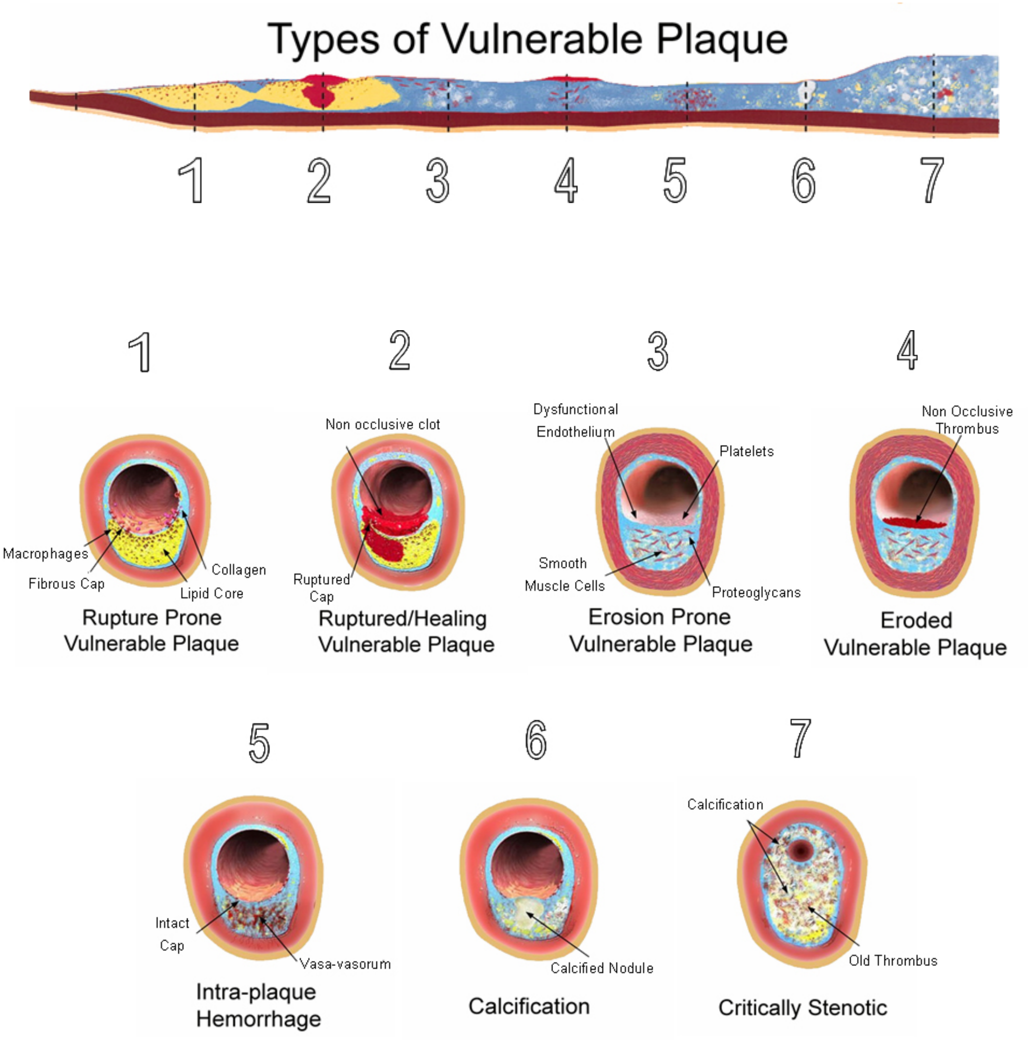

Figure 1.5: Illustration of various types of vulnerable plaques as underlying cause of acute coronary syndromes (adapted from Naghavi et. al., (2003) [21]).

1: Rupture prone vulnerable plaque with large lipid core and a thin fibrous cap infiltrated by macrophages. 2: Ruptured plaque with sub-occlusive thrombus and early organization. 3: Erosion-prone plaque with proteoglycan matrix in a smooth muscle cell-rich plaque. 4: Eroded plaque with sub-occlusive thrombus. 5: Intraplaque hemorrhage secondary to a leaking vasa vasorum. 6: Calcific nodule protruding into the vessel lumen. 7: A critically stenotic plaque with may contain the debris of extensive calcification and thrombus.

1.5.2 Current therapeutic approaches

Percutaneous coronary intervention (PCI): PCI is an interventional procedure aimed at stabilizing the plaque by increasing luminal diameter, direct plaque compression and disruption of thrombus [22]. An example of such a technique is balloon angioplasty where a balloon is inflated to push the plaque towards the vessel wall to increase the luminal diameter. The effectiveness of PCI could be temporary in nature and may lead to restenosis. Indeed, the growth of new tissues could reduce the luminal area and increase the chances of recurrence of stenosis. However, restenosis can be moderated by using drug eluting stents. PCI for acute myocardial infarction is also limited by a higher rate of recurrent ischemia and hemorrhage complications.

Coronary artery by-pass graft surgery (CABG): CABG is a well established treatment for stable symptomatic atherosclerotic plaques. The surgical procedure creates new routes around narrowed and blocked arteries, allowing sufficient blood flow. The procedure is performed on critically ill patients with well established symptoms [23].

Lipid lowering drugs: The most common lipid lowering technique is the use of statin therapy. Statins are drugs developed to inhibit HMG CoA-reductase in the liver reducing hepatic cholesterol synthesis. Statin administration has also shown clinical improvements in the endothelial function [23].

Anti-platelet agents: Several drugs that prevent the aggregation of platelets and also reduce the inflammation have the potential to minimize the progression of thrombus following vulnerable plaque disruption. The use of aspirin, thienopyridines and platelet GP IIb/IIIa inhibitor therapy are some of the documented methods used to reduce platelet aggregation [23].

1.5.3 Current imaging techniques

Non-invasive imaging of blood vessels from outside the body is desirable. However, such an imaging process is only limited to the vessels close to the surface of the skin, for example, carotid arteries are routinely examined non-invasively using a linear array ultrasound transducer. The size and proximity of other vessels like the coronary arteries makes it impossible to image them non-invasively with acceptable resolution. The most common manifestation of atherosclerosis is a progressive constriction of the blood vessels affecting blood flow. Generally, the structural change caused by luminal narrowing is observed through angiographic images of the artery and stenosis has been a standard diagnostic indicator of the disease. However, the ability of X-ray angiography to detect vulnerable plaques is minimal [24, 25]. These radiographic images present a silhouette of the vessel with no clear information on the type and content of the plaque. Therefore, catheter based invasive imaging of the arterial cross-section with high resolution is gaining prominence. Moreover, the catheter based techniques could also be used to guide cardiac interventional procedures. Common imaging techniques are being adapted for intravascular imaging and possess advantages as well as fundamental limitations to detect and differentiate the rupture prone atherosclerotic lesion.

Intravascular Ultrasound Imaging (IVUS): An ultrasound transducer element (or array of elements) is placed at the tip of a flexible catheter to transmit and receive the high frequency sound waves from the arterial tissue and plaque. IVUS provides high resolution, real-time *in vivo* images (intensity of backscattered ultrasound echoes) of the artery and has become particularly useful in delineating plaque morphology and distribution and providing a rationale to guide trans-catheter interventions. High frequency IVUS (typically 40 MHz) imaging is known to provide images with a radial (axial) resolution of about 100 μm – 150 μm. Backscattered ultrasound echoes are generated as a result of difference in acoustic impedance of tissue structures. Therefore, hard calcified plaques with bright echoes accompanied with acoustic shadowing are easier to detect in IVUS images. Radiofrequency IVUS analysis is also capable of imaging the vulnerable plaque with a lipid core, a fissured plaque and plaque with detectable stenosis. However, the reliability of IVUS imaging in predicting these lipid filled lesions is limited [26-28]. The inclusion of add-on techniques like intravascular strain elastography (intravascular palpography) has increased the utility of IVUS imaging [29].

Optical Coherence Tomography (OCT): OCT utilizes an interferometric light detection mechanism to create high resolution intensity images from light reflected from tissue micro structures [30]. Intravascular OCT has high resolution (<10μm) and is capable of delineating the intimal cap and differentiating fibrous, fibro-calcific and lipid filled plaques [31]. Recent findings have suggested the possibility to detect macrophages [32]. However, the penetration depth in OCT is limited to around 1 mm by the two-way scattering of light. Furthermore, the lumen needs to be flushed with saline or blocked temporarily to create a blood free environment.

Angioscopy: Intra-coronary angioscopy facilitates direct visualization of the plaque surface, presence of thrombus and macroscopic features of the arterial wall [33]. The observed color of the surface (red, yellow and white) indicates the presence of possible plaque components (thrombus, plaque or none) [34]. Direct visualization permits detection of structural irregularities caused by a degraded endothelium or fissures. The technique does not provide a morphological depth dependent assessment of the plaque and vessel. Furthermore, angioscopy is insensitive to subtle differences in the composition of the plaque.

Intravascular thermography: Thermography is catheter-based technique to detect the thermal heterogeneity in the plaque caused by the increase in temperature during inflammation using small heat sensors [35]. Temperature differences correlate well with macrophage cell density, which may be a positive predictor of plaque disruption and impending thrombosis [36, 37]. However, there is no clear evidence linking temperature difference with plaque vulnerability. The independent role of thermography as n interventional plaque imaging technique is limited without structural information.

Raman Spectroscopy: Raman spectroscopy is an intravascular optical technique for analyzing the chemical composition of the arterial tissue. The molecular characteristics of the lipids and calcium salts observed from the scattered light makes Raman spectroscopy highly sensitive for plaque detection [38]. The technique is one dimensional, but a combination with other imaging techniques like IVUS could be useful in localizing and quantifying cholesterol and calcium salts in atherosclerotic plaques [39].

Intravascular Magnetic Resonance Imaging (IVMRI): MRI characterizes components on the basis of biophysical and biochemical parameters (water content, molecular motion, chemical composition and concentration). Although, MRI has emerged as a leading non-invasive imaging modality for characterizing the carotid plaques [40], imaging of deeper arteries is difficult, because of poor signal to noise ration and insufficient resolution. Therefore, the distance between the detector and coil is minimized in an intravascular implementation of the technique [41]. IVMRI yields adequate resolution to discriminate plaque components, including, lipid, collagen, thrombus and calcium based on biochemical properties [42]. Limitations exist in the coil designs requiring multiple catheter positions and repeated imaging as well as reduction in quality of the image due to misalignment of the coil with the external magnet [32].

A summary of the comparison between the vulnerable plaque intravascular imaging techniques is presented in Table 1.1. The review of the capabilities of the various imaging techniques suggests the need for multi-modality imaging to combine the advantages of the various methods.

Table 1.1: Comparison of vulnerable plaque imaging techniques [32, 42]

Intravascular imaging techniques	Spatial Resolution (µm)	Penetration Depth (mm)	Vulnerable Plaque Features					
			Structural Image of Wall	Fibrous Cap	Lipid Core	Inflammation	Calcium	Thrombus
Intravascular Ultrasound	50 – 100	10	X	X	X	-	X	X
Angioscopy	-	-	X	-	-	-	X	X
Optical Coherence Tomography (OCT)	2-30	1-2	-	X	X	-	X	X
Thermography	500	Surface	-	-	-	X	-	-
Raman Spectroscopy	N.A.	1-1.5	-	X	X	X	X	-
Intravascular MRI	160	Good	-	X	X	-	X	X

1.6 PHOTOACOUSTIC IMAGING

The clinical need for improved diagnostic information has motivated the research on new imaging techniques. Traditionally, medical imaging has been dominated by ultrasound, MRI and X ray computed tomography. However, certain fundamental limitations motivated the search for additional imaging techniques to supplement existing methods. For example, ultrasound has excellent penetration depth, provides real-time images, is easy to handle, provides vital structural information and can be used for imaging a wide spectrum of biological tissues. Nevertheless, the ultrasound images suffer from limited contrast and may not provide comprehensive image information required for accurate diagnosis. Among the various imaging techniques currently being developed, photoacoustic imaging presents multiple advantages based on the fundamental principle that bridges optics and ultrasound.

The photoacoustic effect was first observed by Alexander Graham Bell in his research work on a photo-phone [43]. He observed that sound could be produced if rapidly interrupted light is incident on a solid sample. The improvement in electronics and laser technology in the late 1970s led to a surge in photoacoustic applications. Consequently, biomedical photoacoustic imaging utilizing pulsed electromagnetic excitation underwent a tremendous growth in the past decade. Typically, non-ionizing electromagnetic excitation including optical and microwave frequencies are utilized in photoacoustic or thermoacoustic imaging with potential for obtaining images with excellent contrast and resolution [44-49].

1.6.1 Generation of photoacoustic transients - theory

The principle behind the generation of photoacoustic pressure signals involves the rapid transformation of optical energy into heat and mechanical stress. Photoacoustic imaging of biological tissues involves time-resolved detection of laser-induced acoustic waves generated under the optical irradiation conditions of temporal pressure confinement [44]. The general steps in photoacoustic imaging of biological tissues follow from the optical-thermal process of stress generation and is described in this section.

Optical excitation: Generally, in biomedical photoacoustic imaging, the tissue is irradiated with a short pulsed-laser source. The laser energy E (mJ/cm^2) incident on an area A (cm^2) creates a radiant exposure of optical fluence ϕ_0 (mJ/cm^2).

$$\phi_o = \frac{E}{A} \tag{1.1}$$

The selection of the duration of the laser pulse width τ_p is an important criterion determining the efficiency of photoacoustic signal generation and the resolution of photoacoustic images. The direct and efficient conversion of optical energy to pressure is possible if the acoustic transient does not leave the heated region during the heating process. The condition is called "stress confinement" and is satisfied if the duration of the laser pulse-width τ_p is shorter than the propagation time of the acoustic transient through the region of distance d and acoustic velocity c.

$$\tau_p << \frac{d}{c} \tag{1.2}$$

The size of the region of laser-tissue interaction d is calculated based on the extent of the smallest absorbing object or the effective penetration depth of the optical excitation. Therefore, the selection of the laser source is partially determined by the stress confinement criterion. Figure 1.6 compiled by Steven Jacques details the list of laser sources in the thermal and stress confinement regimes [50]. A Q-switched pulsed Nd:YAG laser source with a short pulse-width (ns) and sufficient penetration depth is commonly employed in certain biomedical photoacoustic imaging applications.

1. <u>Laser-tissue optical interaction:</u> The light incident on the tissue goes through multiple absorption and scattering events. The interaction of the light with the tissues is dependent on the optical properties (μ_a, μ_s and μ_{eff}). The distribution of photon energy in the tissue can be modeled using Monte Carlo methods [51, 52]. Analytical solutions of the light distribution in scattering dominated tissues can be arrived at by utilizing the diffusion approximation [53]. The effect of the absorption and reduced scattering lead to an effective attenuation coefficient μ_{eff} given by,

$$\mu_{eff} = \sqrt{3\mu_a\left(\mu_a + \mu_s^{'}\right)} \tag{1.3}$$

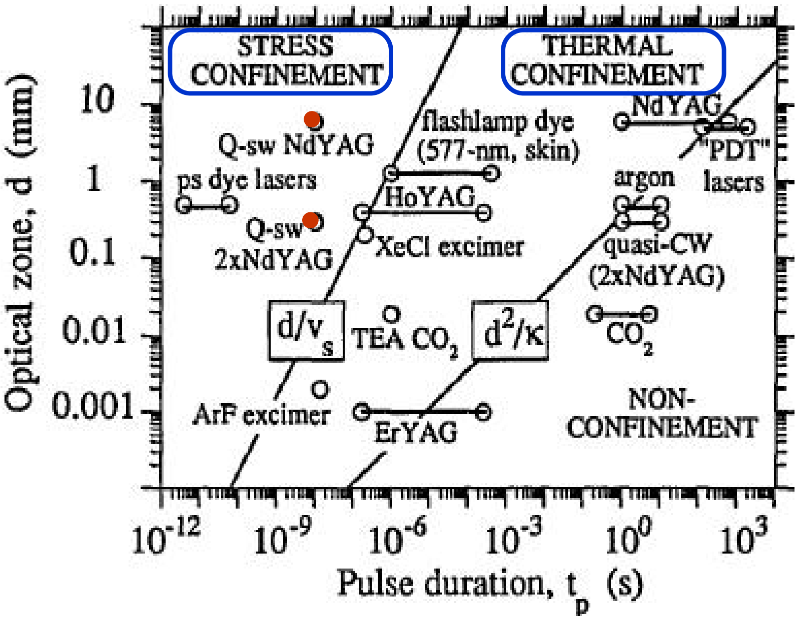

Figure 1.6: Spatial confinement of thermal and stress energy for various lasers. [50]. (Adapted by permission from Optical Society of America)

Generally, the radiant exposure ϕ (mJ/cm^2) decreases exponentially with depth z (cm). Photoacoustic signals are generated only in the regions of absorption. Therefore, the energy density W (J/cm^3) deposited in a given volume with spatial coordinates x, y and z is given by,

$$W = \mu_a(x, y, z) \cdot \phi(x, y, z) \tag{1.4}$$

2. Laser-tissue thermal interaction: The energy deposited in a given volume with density ρ and specific heat Cp is followed by an increase in temperature ΔT given by,

$$\Delta T = \frac{W}{\rho \cdot C_p} \tag{1.5}$$

The increase in temperature causes a thermoelastic expansion in the medium and under the conditions of stress confinement produces stress transients given by,

$$\Delta P = \frac{1}{\gamma} \cdot \frac{\Delta V}{V} = \frac{1}{\gamma} \cdot \beta \cdot \Delta T(z) = \frac{1}{\gamma} \cdot \beta \cdot \frac{W(z)}{\rho \cdot C_p} = \Gamma \cdot \mu_a \cdot \phi(z) \tag{1.6}$$

In the equation 1.6, the photoacoustic pressure ΔP is proportional to the optical absorption coefficient, optical fluence and the thermal coefficient of volume expansion β (K^{-1}). The thermoelastic efficiency, Γ, also called the Grüneisen parameter is a dimensionless, temperature-dependent factor proportional to the fraction of the thermal energy converted into mechanical stress. The propagated stress can be detected using an ultrasound detector placed outside the irradiated volume.

1.6.2 Contrast in photoacoustic imaging

The contrast in photoacoustic imaging is primarily determined by difference in the optical absorption coefficient of various types of tissues. Equation (1.6) explains the direct dependence of the magnitude of the photoacoustic pressure on the optical absorption. Therefore, in addition to the selection of the laser based on the stress confinement criterion, another important parameter taken into consideration is the optical excitation wavelength. Indeed, the absorption coefficient of the imaging target will determine the wavelength of optical excitation. A compilation of the absorption and extinction coefficients of common types of biological tissues is presented in Fig. 1.7 [54]. Several key observations come to light from the spectral variation of absorption of the tissues. First, the absorption of light by blood (oxy and de-oxy hemoglobin) is dominant in the spectral region between 400 and 600 nm. In the region between 700 and 900 nm the optical penetration increases. The increased penetration is attributed to a decrease in the absorption by blood that forms the major constituent of blood vessels.

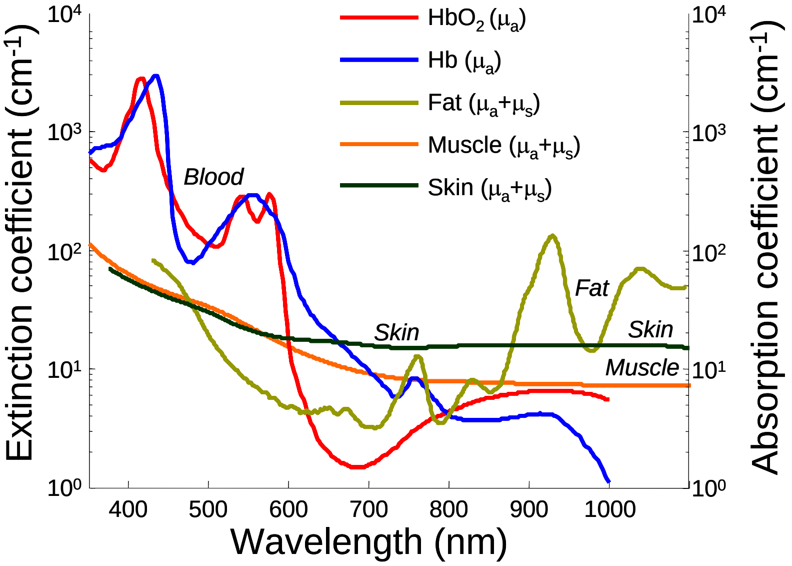

Figure 1.7: Optical absorption and extinction coefficients of common biological tissues (adapted from [54]).

1.7 ORGANIZATION OF THE THESIS

The aim of the research described in this thesis is to develop and evaluate an intravascular photoacoustic imaging device that may present a unique and potentially important imaging tool needed during coronary artery interventions. The research work is documented and organized into six chapters.

CHAPTER 2 describes the components of the laboratory prototype of the intravascular photoacoustic (IVPA) imaging system and the method to obtain cross-sectional photoacoustic images using an IVUS imaging catheter. The custom-built intravascular imaging system is capable of obtaining simultaneous ultrasound and photoacoustic cross-sectional images of the arterial wall. We evaluate and test the ability of the combined system to obtain IVUS and IVPA images using tissue mimicking arterial phantoms. Some results presented in this chapter were published in the journal - IEEE Transactions on Ultrasonics, Ferroelectrics and Frequency Control as an article titled

“Intravascular Photoacoustic Imaging Using an IVUS Imaging Catheter” vol. 54, No. 5, pp. 978-986 (2007). Copyright© 2007 IEEE. Some relevant figures are reprinted with permission from IEEE.

The subsequent task ***(CHAPTER 3)*** was to determine the ability of IVPA imaging to detect plaques. Ex vivo animal imaging studies were performed on an aorta tissue obtained from a well characterized rabbit model of atherosclerosis. The combined IVUS/IVPA imaging system utilized for these studies comprised of a 532 nm pulsed laser source and a 40 MHz, 2.5-French, IVUS imaging catheter detector. The results of these studies will be submitted as an article for publication.

The arterial tissue and vulnerable plaques are heterogeneous in composition. Each of the tissue and lesion components is expected to possess a characteristic optical wavelength dependent absorption. The change in optical absorption and therefore photoacoustic response may help identify plaque composition. Therefore, we investigate ***(CHAPTER 4)*** the ability of spectroscopic photoacoustic imaging to differentiate vulnerable atherosclerotic plaques. The results of these studies will be submitted as an article for publication.

Photoacoustic response is generated by the absorption of pulsed laser light and localized thermal confinement of energy. The width of the laser pulse is shorter than the time required for the diffusion of stress and heat out of the irradiated volume. Therefore, there will be no damage to the surrounding tissues. However, there are no guidelines for the safety of intravascular photoacoustic imaging. There is an essential need to determine the temperature at the site of laser-tissue interaction. In our combined imaging system, both, IVUS and IVPA are performed simultaneously. Therefore, we present ***(CHAPTER 5)*** an IVUS based method to remotely monitor the temperature following pulsed laser excitation and confirm safety in IVPA imaging. The results of these studies were accepted for publication in Ultrasound in Medicine and Biology.

In ***CHAPTER 6*** we summarize the results of our work, address the limitations of the imaging system, draw conclusions and recommend areas of future work.

1.8 REFERENCES

[1] W. Rosamond, K. Flegal, G. Friday, K. Furie, A. Go, K. Greenlund, N. Haase, M. Ho, V. Howard, B. Kissela, S. Kittner, D. Lloyd-Jones, M. McDermott, J. Meigs, C. Moy, G. Nichol, C. J. O'Donnell, V. Roger, J. Rumsfeld, P. Sorlie, J. Steinberger, T. Thom, S. Wasserthiel-Smoller, Y. Hong, and S. for the American Heart Association Statistics Committee and Stroke Statistics, "Heart Disease and Stroke Statistics--2007 Update: A Report From the American Heart Association Statistics Committee and Stroke Statistics Subcommittee," *Circulation*, vol. 115, pp. e69-171, 2007.

[2] Y. C. Fung, *Biomechanics: Mechanical properties of living tissues*, 2nd ed. New York: Springer-Verlag, 1993.

[3] P. Libby, "Current Concepts of the Pathogenesis of the Acute Coronary Syndromes," *Circulation*, vol. 104, pp. 365-372, 2001.

[4] M. J. Davies, "The pathophysiology of acute coronary syndromes," *Heart*, vol. 83, pp. 361-6, 2000.

[5] R. Ross and J. A. Glomset, "Atherosclerosis and the arterial smooth muscle cell: Proliferation of smooth muscle is a key event in the genesis of the lesions of atherosclerosis," *Science*, vol. 180, pp. 1332-9, 1973.

[6] R. Ross, "Atherosclerosis--an inflammatory disease," *N Engl J Med*, vol. 340, pp. 115-26, 1999.

[7] R. Virmani, A. P. Burke, F. D. Kolodgie, and A. Farb, "Pathology of the thin-cap fibroatheroma: a type of vulnerable plaque," *J Interv Cardiol*, vol. 16, pp. 267-72, 2003.

[8] P. Libby, "Inflammation in atherosclerosis," *Nature*, vol. 420, pp. 868-74, 2002.

[9] R. S. Cotran, V. Kumar, S. L. Robbins, and F. J. Schoen, "Inflammation and repair," in *Pathologic basis of disease*. Philadelphia: WB Saunders Company, 1994, pp. 51-93.

[10] L. Jonasson, J. Holm, O. Skalli, G. Bondjers, and G. K. Hansson, "Regional accumulations of T cells, macrophages, and smooth muscle cells in the human atherosclerotic plaque," *Arteriosclerosis*, vol. 6, pp. 131-8, 1986.

[11] C. J. Schwartz and J. R. Mitchell, "Cellular infiltration of the human arterial adventitia associated with atheromatous plaques," *Circulation*, vol. 26, pp. 73-8, 1962.

[12] G. K. Hansson, "Immune mechanisms in atherosclerosis," *Arterioscler Thromb Vasc Biol*, vol. 21, pp. 1876-90, 2001.

[13] K. Skalen, M. Gustafsson, E. K. Rydberg, L. M. Hulten, O. Wiklund, T. L. Innerarity, and J. Boren, "Subendothelial retention of atherogenic lipoproteins in early atherosclerosis," *Nature*, vol. 417, pp. 750-4, 2002.

[14] N. Leitinger, "Oxidized phospholipids as modulators of inflammation in atherosclerosis," *Curr Opin Lipidol*, vol. 14, pp. 421-30, 2003.

[15] E. E. Eriksson, X. Xie, J. Werr, P. Thoren, and L. Lindbom, "Importance of primary capture and L-selectin-dependent secondary capture in leukocyte accumulation in inflammation and atherosclerosis in vivo," *J Exp Med*, vol. 194, pp. 205-18, 2001.

[16] M. I. Cybulsky and M. A. Gimbrone, Jr., "Endothelial expression of a mononuclear leukocyte adhesion molecule during atherogenesis," *Science*, vol. 251, pp. 788-91, 1991.

[17] C. A. Janeway, Jr. and R. Medzhitov, "Innate immune recognition," *Annu Rev Immunol*, vol. 20, pp. 197-216, 2002.

[18] J. Frostegard, A. K. Ulfgren, P. Nyberg, U. Hedin, J. Swedenborg, U. Andersson, and G. K. Hansson, "Cytokine expression in advanced human atherosclerotic plaques: dominance of pro-inflammatory (Th1) and macrophage-stimulating cytokines," *Atherosclerosis*, vol. 145, pp. 33-43, 1999.

[19] H. C. Stary, A. B. Chandler, S. Glagov, J. R. Guyton, W. Insull, Jr., M. E. Rosenfeld, S. A. Schaffer, C. J. Schwartz, W. D. Wagner, and R. W. Wissler, "A definition of initial, fatty streak, and intermediate lesions of atherosclerosis. A report from the Committee on Vascular Lesions of the Council on Arteriosclerosis, American Heart Association," *Circulation*, vol. 89, pp. 2462-78, 1994.

[20] H. C. Stary, "Natural history and histological classification of atherosclerotic lesions: an update," *Arterioscler Thromb Vasc Biol*, vol. 20, pp. 1177-8, 2000.

[21] M. Naghavi, P. Libby, E. Falk, S. W. Casscells, S. Litovsky, J. Rumberger, J. J. Badimon, C. Stefanadis, P. Moreno, G. Pasterkamp, Z. Fayad, P. H. Stone, S.

Waxman, P. Raggi, M. Madjid, A. Zarrabi, A. Burke, C. Yuan, P. J. Fitzgerald, D. S. Siscovick, C. L. de Korte, M. Aikawa, K. E. Juhani Airaksinen, G. Assmann, C. R. Becker, J. H. Chesebro, A. Farb, Z. S. Galis, C. Jackson, I. K. Jang, W. Koenig, R. A. Lodder, K. March, J. Demirovic, M. Navab, S. G. Priori, M. D. Rekhter, R. Bahr, S. M. Grundy, R. Mehran, A. Colombo, E. Boerwinkle, C. Ballantyne, W. Insull, Jr., R. S. Schwartz, R. Vogel, P. W. Serruys, G. K. Hansson, D. P. Faxon, S. Kaul, H. Drexler, P. Greenland, J. E. Muller, R. Virmani, P. M. Ridker, D. P. Zipes, P. K. Shah, and J. T. Willerson, "From vulnerable plaque to vulnerable patient: a call for new definitions and risk assessment strategies: Part I," *Circulation*, vol. 108, pp. 1664-72, 2003.

[22] J. M. Ahmed, G. S. Mintz, N. J. Weissman, A. J. Lansky, A. D. Pichard, L. F. Satler, and K. M. Kent, "Mechanism of lumen enlargement during intracoronary stent implantation: an intravascular ultrasound study," *Circulation*, vol. 102, pp. 7-10, 2000.

[23] L. Kritharides, D. Brieger, S. B. Freedman, and H. C. Lowe, "Treatment of vulnerable plaques - current and future strategies," in *High risk atherosclerotic plaques - mechanisms, imaging, models and therapy*, L. M. Khachigian, Ed. New York: CRC Press, 2004.

[24] J. A. Ambrose, M. A. Tannenbaum, D. Alexopoulos, C. E. Hjemdahl-Monsen, J. Leavy, M. Weiss, S. Borrico, R. Gorlin, and V. Fuster, "Angiographic progression of coronary artery disease and development of myocardial infarction," *J. Am. Col. Cardiol.*, vol. 12, pp. 56-62, 1998.

[25] W. C. Little, M. Constantinescu, R. J. Applegate, M. A. Kutcher, M. T. Burrows, F. R. Kahl, and W. P. Santamore, "Can coronary angiography predict the site of a subsequent myocardial infarction in patients with mild-to-moderate coronary artery disease?," *Circulation*, vol. 78, pp. 1157-66, 1988.

[26] S. E. Nissen and P. Yock, "Intravascular Ultrasound : Novel Pathophysiological Insights and Current Clinical Applications," *Circulation*, vol. 103, pp. 604-616, 2001.

[27] N. Komiyama, G. J. Berry, M. L. Kolz, A. Oshima, J. A. Metz, P. Preuss, A. F. Brisken, M. Pauliina Moore, P. G. Yock, and P. J. Fitzgerald, "Tissue characterization of atherosclerotic plaques by intravascular ultrasound radiofrequency signal analysis: an in vitro study of human coronary arteries," *Am Heart J*, vol. 140, pp. 565-74, 2000.

[28] F. Prati, E. Arbustini, A. Labellarte, B. Dal Bello, L. Sommariva, M. T. Mallus, A. Pagano, and A. Boccanelli, "Correlation between high frequency intravascular ultrasound and histomorphology in human coronary arteries," *Heart*, vol. 85, pp. 567-70, 2001.

[29] C. L. de Korte, G. Pasterkamp, A. F. van der Steen, H. A. Woutman, and N. Bom, "Characterization of plaque components with intravascular ultrasound elastography in human femoral and coronary arteries in vitro," *Circulation*, vol. 102, pp. 617-23, 2000.

[30] J. G. Fujimoto, S. A. Boppart, G. J. Tearney, B. E. Bouma, C. Pitris, and M. E. Brezinski, "High resolution in vivo intra-arterial imaging with optical coherence tomography," *Heart*, vol. 82, pp. 128-33, 1999.

[31] H. Yabushita, B. E. Bouma, S. L. Houser, H. T. Aretz, I. K. Jang, K. H. Schlendorf, C. R. Kauffman, M. Shishkov, D. H. Kang, E. F. Halpern, and G. J. Tearney, "Characterization of human atherosclerosis by optical coherence tomography," *Circulation*, vol. 106, pp. 1640-5, 2002.

[32] B. D. MacNeill, H. C. Lowe, M. Takano, V. Fuster, and I. K. Jang, "Intravascular modalities for detection of vulnerable plaque: current status," *Arterioscler Thromb Vasc Biol*, vol. 23, pp. 1333-42, 2003.

[33] Y. Uchida, F. Nakamura, T. Tomaru, T. Morita, T. Oshima, T. Sasaki, S. Morizuki, and J. Hirose, "Prediction of acute coronary syndromes by percutaneous coronary angioscopy in patients with stable angina," *Am Heart J*, vol. 130, pp. 195-203, 1995.

[34] A. Itoh, S. Miyazaki, H. Nonogi, S. Daikoku, and K. Haze, "Angioscopic prediction of successful dilatation and of restenosis in percutaneous transluminal coronary angioplasty. Significance of yellow plaque," *Circulation*, vol. 91, pp. 1389-96, 1995.

[35] L. Diamantopoulos, "Arterial wall thermography," *J Interv Cardiol*, vol. 16, pp. 261-6, 2003.

[36] W. Casscells, B. Hathorn, M. David, T. Krabach, W. K. Vaughn, H. A. McAllister, G. Bearman, and J. T. Willerson, "Thermal detection of cellular infiltrates in living atherosclerotic plaques: possible implications for plaque rupture and thrombosis," *Lancet*, vol. 347, pp. 1447-51, 1996.

[37] C. Stefanadis, L. Diamantopoulos, C. Vlachopoulos, E. Tsiamis, J. Dernellis, K. Toutouzas, E. Stefanadi, and P. Toutouzas, "Thermal heterogeneity within human atherosclerotic coronary arteries detected in vivo: A new method of detection by application of a special thermography catheter," *Circulation*, vol. 99, pp. 1965-71, 1999.

[38] J. F. Brennan, 3rd, T. J. Romer, R. S. Lees, A. M. Tercyak, J. R. Kramer, Jr., and M. S. Feld, "Determination of human coronary artery composition by Raman spectroscopy," *Circulation*, vol. 96, pp. 99-105, 1997.

[39] T. J. Romer, J. F. Brennan, 3rd, G. J. Puppels, A. H. Zwinderman, S. G. van Duinen, A. van der Laarse, A. F. van der Steen, N. A. Bom, and A. V. Bruschke, "Intravascular ultrasound combined with Raman spectroscopy to localize and quantify cholesterol and calcium salts in atherosclerotic coronary arteries," *Arterioscler Thromb Vasc Biol*, vol. 20, pp. 478-83, 2000.

[40] T. Leiner, S. Gerretsen, R. Botnar, E. Lutgens, V. Cappendijk, E. Kooi, and J. van Engelshoven, "Magnetic resonance imaging of atherosclerosis," *Eur Radiol*, vol. 15, pp. 1087-99, 2005.

[41] E. Larose, Y. Yeghiazarians, P. Libby, E. K. Yucel, M. Aikawa, D. F. Kacher, E. Aikawa, S. Kinlay, F. J. Schoen, A. P. Selwyn, and P. Ganz, "Characterization of human atherosclerotic plaques by intravascular magnetic resonance imaging," *Circulation*, vol. 112, pp. 2324-31, 2005.

[42] Z. A. Fayad and V. Fuster, "Clinical imaging of the high-risk or vulnerable atherosclerotic plaque," *Circ Res*, vol. 89, pp. 305-16, 2001.

[43] A. G. Bell, "art. XXXIV on the production and reproduction of sound by light," *Am. J. Sci.*, vol. 20, pp. 305-324, 1880.

[44] A. A. Oraevsky and A. A. Karabutov, "Optoacoustic Tomography," in *Biomedical Photonics Handbook*, T. Vo-Dinh, Ed.: CRC Press, 2003, pp. 34-1 - 34-34.

[45] P. C. Beard and T. N. Mills, "Characterization of post mortem arterial tissue using time-resolved photoacoustic spectroscopy at 436, 461 and 532 nm," *Phys Med Biol*, vol. 42, pp. 177-98, 1997.

[46] S. Y. Emelianov, S. R. Aglyamov, J. Shah, S. Sethuraman, W. G. Scott, R. Schmitt, M. Motamedi, A. Karpiouk, and A. Oraevsky, "Combined ultrasound, optoacoustic and elasticity imaging," *Proceedings of the 2004 SPIE Photonics West Symposium: Photons Plus Ultrasound: Imaging and Sensing*, vol. 5320, pp. 101-112, 2004.

[47] R. A. Kruger, D. R. Reinecke, and G. A. Kruger, "Thermoacoustic computed tomography--technical considerations," *Med Phys*, vol. 26, pp. 1832-7, 1999.

[48] A. A. Oraevsky, S. L. Jacques, and F. K. Tittle, "Determination of tissue optical properties by time-resolved detection of laser-induced stress waves," presented at Proc. of SPIE, 1993.

[49] X. Wang, Y. Pang, G. Ku, X. Xie, G. Stoica, and L. V. Wang, "Noninvasive laser-induced photoacoustic tomography for structural and functional in vivo imaging of the brain," *Nat Biotechnol*, vol. 21, pp. 803-6, 2003.

[50] S. L. Jacques, "Role of tissue optics and pulse duration on tissue effects during high-power laser irradiation," *Journal of applied optics*, vol. 32, 1993.

[51] S. L. Jacques and L. V. Wang, "Monte Carlo modelling of light transport in tissues," in *Optical-Thermal Response of Laser-Irradiated Tissue*, A. J. Welch and M. J. van Gemert, Eds. Newyork: Plenum, 1995, pp. 73-100.

[52] M. Keijzer, S. L. Jacques, S. A. Prahl, and A. J. Welch, "Light distributions in artery tissue: Monte Carlo simulations for finite-diameter laser beams," *Lasers Surg Med*, vol. 9, pp. 148-54, 1989.

[53] S. A. Prahl, "The diffusion approximation in three dimensions," in *Optical-Thermal Response of Laser-Irradiated Tissue*, A. J. Welch and M. J. van Gemert, Eds. Newyork: Plenum, 1995, pp. 207-231.

[54] S. Y. Emelianov, S. R. Aglyamov, A. B. Karpiouk, S. Mallidi, S. Park, S. Sethuraman, J. Shah, R. W. Smalling, J. M. Rubin, and W. G. Scott, "Synergy and applications of combined ultrasound, elasticity and photoacoustic imaging," *Proceedings of the 2006 IEEE International Ultrasonics Symposium*, pp. 405-415, 2006.

Chapter 2: Combined Intravascular Ultrasound and Photoacoustic Imaging

2.1 INTRODUCTION

Photoacoustic imaging technology, in principle, merges two imaging fields – ultrasound and optics. The technique has the ability to image the optical contrast at ultrasonic resolution. Owing to strong optical absorption of hemoglobin, photoacoustic imaging has been a natural choice for the investigation of blood oxygenation and imaging the angiogenesis. In addition to the above applications, a recent surge of research forecasts the impact and suitability of biomedical photoacoustic imaging in the fields of blood-vessel investigation, tumor diagnostics, inflammation, mammography and dermatology [1-6].

One application that needs immediate screening, diagnostic and therapeutic attention is the disease of the arteries. The concept of the vulnerable plaque, introduced and discussed in chapter 1, was described based on histopathological description of culprit lesions. Among the several invasive and non-invasive imaging techniques investigated for plaque detection, there is yet no clear consensus on a standard reference method for imaging of atherosclerosis. Therefore, large scale investigations are currently underway in search of a technique that could detect plaques with reasonable sensitivity or specificity [7].

The current concept of a vulnerable plaque focuses on the characterization of the structure and behavior of the plaque lesion. An intraluminal assessment of the vulnerable plaque composition will most likely provide the necessary information to predict the occurrences of acute coronary events. In addition, a multi-modal imaging approach could possibly improve diagnosis and provide information for appropriate management of atherosclerosis. Therefore, we develop an intravascular photoacoustic (IVPA) imaging technique and assess the performance of the system in combination with intravascular ultrasound (IVUS) imaging.

In this chapter, we investigate and test the feasibility of performing intravascular photoacoustic (IVPA) imaging using a clinical IVUS imaging catheter. A custom-designed laboratory prototype of an intravascular imaging system was developed to obtain IVUS and IVPA images simultaneously. The performance of the combined imaging system was evaluated by obtaining tomographic IVUS and IVPA images of arterial tissue mimicking phantoms. Further, we quantify and compare the difference in the resolution (axial and lateral) of IVUS and IVPA imaging using the IVUS imaging catheter.

2.2 COMBINED IVUS/IVPA IMAGING SYSTEM

Intravascular ultrasound (IVUS) refers to a minimally invasive catheter-based ultrasonic imaging modality. In IVUS imaging, an access catheter on a conventional guide wire is used to advance the IVUS catheter to the distal portion of the artery under examination. The tissue is imaged using a high frequency ultrasound beam transmitted to and received from a particular direction. The time between transmission of the ultrasound pressure pulse and reception of the backscattered wave is directly related to the distance between the source and the reflector within the tissue. The constructive and destructive interference of the scattered ultrasound echoes within a resolution volume is indicative of the microscopic tissue inhomogeneities. Therefore, IVUS imaging is capable of providing information on arterial tissue morphology.

In intravascular photoacoustic (IVPA) imaging the thermoelastic response from the tissue irradiated with a short laser pulse is detected with an ultrasound detector. The photoacoustic response depends on the optical absorption properties of the tissue components and could be an indicator of the pathological state of the tissue. The decision to perform combined IVUS and IVPA imaging is based on the following factors.

- Diagnostic information obtained using IVPA imaging may supplement as well as complement IVUS imaging.
- The IVUS imaging catheter as a common detector for both IVUS and IVPA imaging makes the integration feasible.
- Excellent morphological assessment capability of IVUS may help spatial localization of photoacoustic response.
- The combined imaging is performed simultaneously (interrogating the same azimuthal location in the artery). Therefore, no additional registration of images is required.

The development of the IVPA imaging system was undertaken bearing in mind the necessity for future integration with a clinical IVUS imaging system. Therefore, except for the optical excitation, IVPA imaging shared all the imaging components of the IVUS imaging. The main components of the combined IVUS/IVPA imaging system include an optical excitation module for photoacoustic imaging, scanning and imaging module for obtaining co-registered IVUS and IVPA images, ultrasound signal detection probe and associated electronic components. The block diagram of the laboratory prototype of the IVUS/IVPA imaging system is presented in Fig. 2.1.

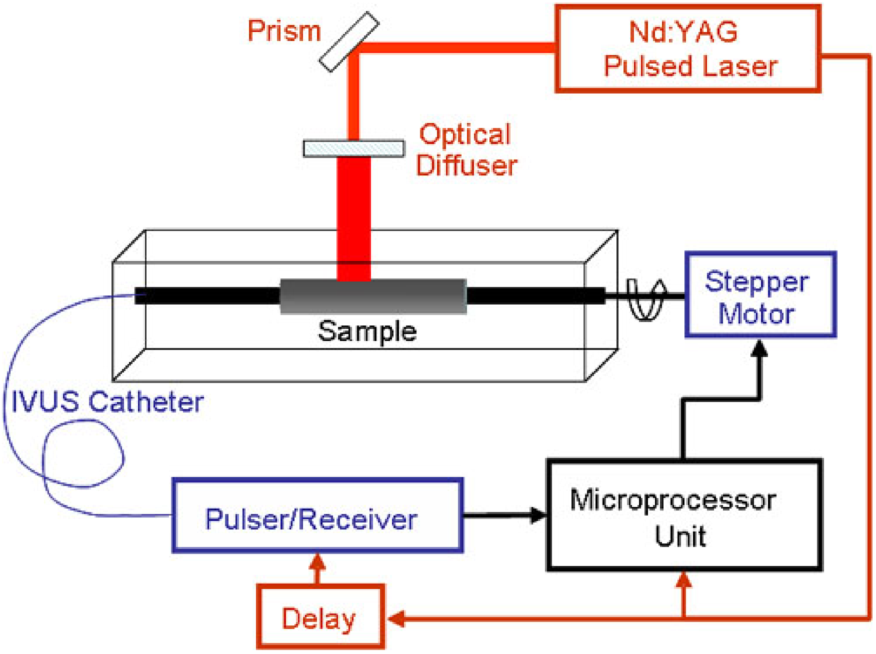

Figure 2.1: Experimental setup for the combined IVUS and IVPA imaging.

2.2.1. Optical excitation

The optical excitation for IVPA imaging was provided by a Q-switched pulsed laser. The choice of the laser was based on the optical excitation wavelength and the duration of the laser pulse. A cost-effective, flash lamp pumped, Q-switched, pulsed Nd:YAG laser (Polaris II, New Wave Research, Inc.) operating at an optical excitation of 1064 nm and harmonic generation at 532 nm was utilized for the preliminary arterial phantom and tissue studies. The 4-5 ns long laser pulse was ideal for IVPA imaging as it satisfied the stress confinement criteria. The laser was capable of a maximum energy of 27 mJ per pulse and a pulse repetition rate of 20 Hz. The selection of the laser excitation wavelength is based on the optical absorption coefficient of the imaged target. The measurements of the optical absorption coefficients of the aorta and other relevant tissue types are quite variable and offer only an approximate guide to the optical behavior of the plaque and arterial wall. In the longer wavelength range between 2000 – 3000 nm, water is a dominant optical absorber. On the other end of the spectrum, strong optical absorption by proteins at the ultraviolet wavelength (200 – 300 nm) limits the optical penetration. The optical diagnostic window between 600 – 1000 nm is ideal for IVPA imaging as the optical absorption by blood and tissue is modest, optical contrast between tissue components is high and there is an increase in the optical absorption of lipids. Therefore, we utilized an Nd:YAG pumped optical parametric oscillator (OPO) pulsed laser source (Vibrant B, Opotek Inc.) tunable between 680 – 950 nm.

Laser light was delivered to the sample from the outside using a prism. Diffused optical excitation was achieved by delivering light through a ground glass optical diffuser. The spot size of the optical beam was increased from 4 mm to 20 mm using the diffused light. Consequently, the total energy fluence per optical pulse incident on the sample was reduced (<20 mJ/cm^2) to conform to laser safety standards (ANSI) [8].

2.2.2. Ultrasonic pulse-echo excitation

The excitation for IVUS pulse-echo imaging was provided by an ultrasound pulser (Panametrics 5073PR, Olympus, Inc.). The pulser provided a negative impulse (-100V) excitation to the high frequency ultrasound element in the IVUS catheter. Indeed, the negative impulse pulser optimizes a broadband response and near surface resolution with fast recovery times. The selection of appropriate pulse energy (2 μJ or 4 μJ) and damping value (50 Ω) are critical for efficient excitation with a low pulse rise-time (2 ns).

2.2.3. Detector

The IVUS transducer element in the catheter also serves as the detector for the IVUS echo and IVPA response. Currently, there are 2 major types of clinical IVUS imaging systems differing in the type of ultrasound detector utilized for imaging – single element mechanical transducer versus multi-element solid state array transducer. Our laboratory prototype of the IVUS/IVPA imaging system utilizes the single element transducer for the following reasons. First, the single element IVUS catheters are available at a higher frequency (40 MHz) compared to the multi-element array based catheters (20 MHz). Indeed, a higher frequency translates into better image resolution which is essential for imaging of coronary plaques. Second, the mechanical single element transducers do not require any additional electronics for the beamforming circuitry. The lack of range dynamic focusing and limited flexibility in scan geometries in a single element transducer do not have a significant impact on the current goal of this research. In our imaging system, the ultrasound echoes and the photoacoustic response were detected using a single element, high frequency (40 MHz), unfocused IVUS imaging catheter (2.5 French, 0.84 mm). The transducer element in the IVUS catheter (Atlantis™ SR PLUS, Boston Scientific Inc.) measured approximately 600 μm in diameter and could be rotated inside the catheter sheath. The photograph of the IVUS catheter and the dimensions are presented in Fig. 2.2.

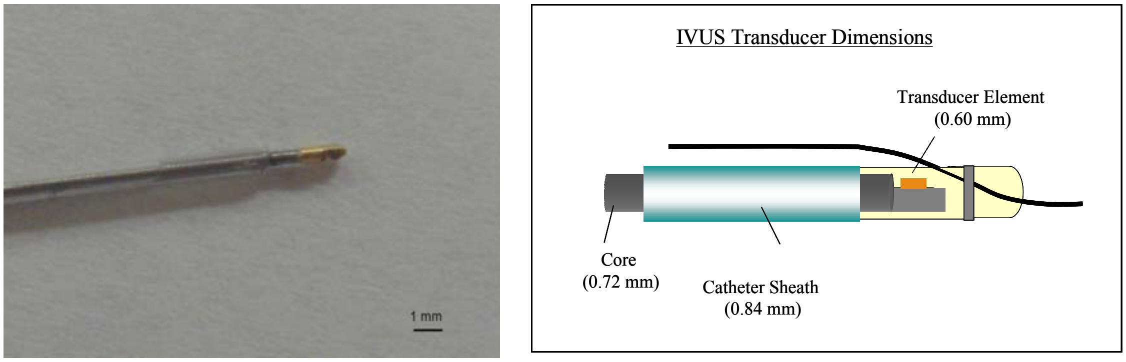

(a) (b)

Figure 2.2: IVUS imaging catheter (Boston Scientific, Inc.). (a) Photograph of the ultrasonic detector at the tip of the IVUS imaging catheter, (b) Illustration of the IVUS catheter and its dimensions.

2.2.4. Combined image acquisition and scanning

Prior to imaging the sample, the catheter was inserted in the lumen and flushed to remove any air bubble trapped between the detector and the catheter sheath. Subsequently, the optical beam and the detector were somewhat aligned. The alignment process involved rotation and horizontal movement of the catheter to a position that produced the maximum photoacoustic response. The entire image acquisition was controlled by an external trigger from the Q-switch of the laser as represented in a typical timing diagram in Fig. 2.3. The same trigger signal, after a delay exceeding the time-of-flight from the deepest structure from the sample was sent to the ultrasonic pulser. For example, a vessel sample with a radius of 15 mm will produce photoacoustic response spanning 10 μs. Therefore, the trigger signal to initiate IVUS imaging could be delayed by a time period of 10 μs. Indeed, the delay period is variable and depends on the size of the vessel sample. The user-defined time delay to separate and produce temporally consecutive IVPA and IVUS signals was generated using a digital delay generator (PDG 2515, Directed Energy, Inc.).

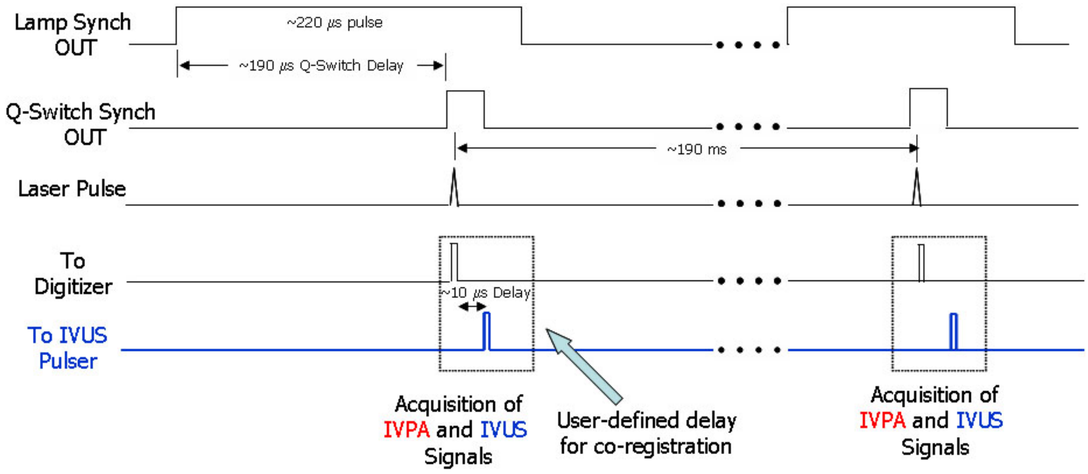

Figure 2.3: A typical timing diagram representing the triggering scheme in our IVUS/IVPA imaging system.

The IVUS pulse-echo and the IVPA signals were obtained from the IVUS catheter through a custom-designed catheter interface. The receiver included an amplifier (0-39 dB) and a bandpass filter (5 – 75 MHz) for signal conditioning. The same receiver captured the photoacoustic signal followed by the ultrasound pulse-echo signal (Fig. 2.4(a)). Generally, the time-of-flight response of the photoacoustic wave is half that of a pulse-echo IVUS response due to near instantaneous propagation of light. The signal-conditioned (amplified and filtered) IVUS and IVPA signals were acquired and digitized using a high speed, 14-bit, 200 MHz analog to digital converter (CS14200, Gage Applied Inc.).

To obtain an IVPA and IVUS image of the cross-section, we rotated the cylindrical sample. A single record contained IVPA and IVUS signals from approximately same azimuthal location on the sample (Fig. 2.4(b)). The laser excitation was from outside illuminating a portion of the sample, therefore we approximately aligned the optical beam with the face of the single-element IVUS transducer to obtain co-registered IVUS and IVPA images. In the clinical system, an intravascular light delivery system will provide simultaneous illumination of the entire cross-section of the artery. Therefore, no additional alignment would be required. A micro-stepping motor (Lin Engineering, Inc.) was employed to incrementally rotate the sample. The motor was controlled using a 2-axis stepper motion-controller (NI-7342, National Instruments, Inc.) and amplifier. The micro-stepper motor and the encoder was configured for a total of 25,000 steps/revolution and 4000 steps/revolution, respectively. The motor drive (Compumotor E-DC, Parker Hannifin, Inc.) was interfaced to the National Instruments stepper motor controller through an interface (UMI-7764). To satisfy the Nyquist sampling and to remain consistent with commercial IVUS imaging systems, we collected 250 IVUS and IVPA beams for one complete rotation. Therefore, each A-line was acquired at an increment of 100 steps of the stepper motor.

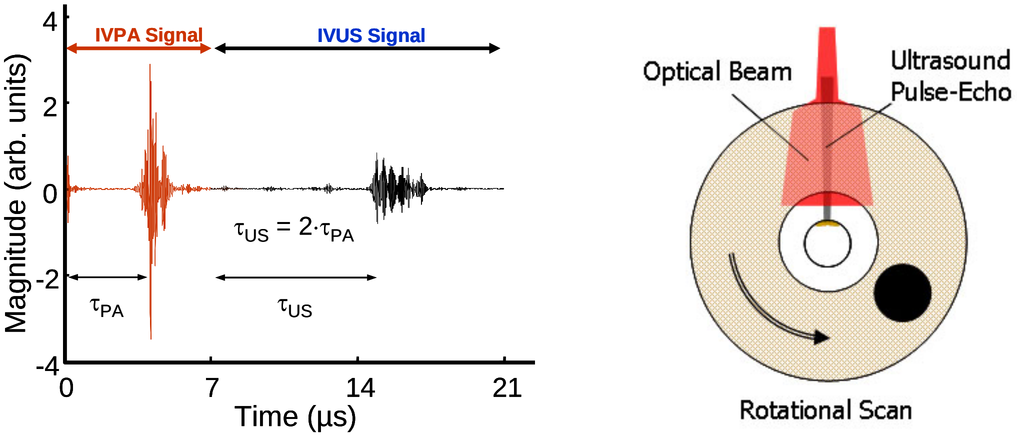

(a) (b)

Figure 2.4: Combined IVUS/IVPA imaging. (a) Representative A-line containing IVPA response followed by a delayed IVUS pulse-echo signal. (b) Illustration of the scanning mechanism.

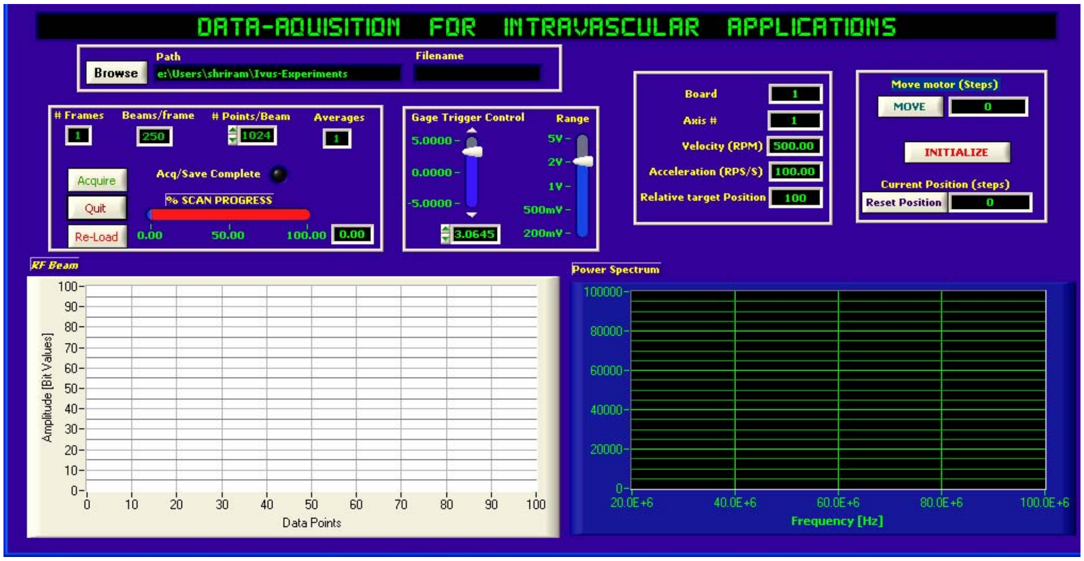
DATA-AQUISITION FOR INTRAVASCULAR APPLICATIONS

Path: e:\Users\shriram\Ivus-Experiments
Filename:
Frames: 1
Beams/frame: 250
Points/Beam: 1024
Averages: 1
% SCAN PROGRESS: 0.00
Gage Trigger Control: 3.0645
Board: 1
Axis #: 1
Velocity (RPM): 500.00
Acceleration (RPS/S): 100.00
Relative target Position: 100
Move motor (Steps): 0
Current Position (steps): 0

Figure 2.5: Software control of the IVUS/IVPA imaging system.

2.2.5 Software control and interface

The entire acquisition sequence was controlled by custom-designed software written in ANSI-C based LabWindows CVI (National Instruments, Inc.). A screen-shot of the user-interface is shown in Fig. 2.5. The graphical interface contained provisions for specifying the acquisition parameters (beams, frames, samples per beam and number of averages) as well as the motion control parameters (velocity, acceleration and the relative target position of the stepper motor). A multiple-record mode of acquisition was employed; where the digitizer acquires a specified number of samples and then waits to re-arm the control for the next trigger. The method decreases the total size of the acquisition and is further useful for acquiring data at high repetition frequencies. For example, in real time IVUS imaging, the images are obtained at the rate of 30 Hz, i.e., 30 frames per second. Therefore, assuming a total of 256 A-lines per image, the pulse repetition frequency of the ultrasonic pulser is 7.68 KHz. The time between 2 successive ultrasonic trigger events is about 130 μs. However, most of the useful information from arterial tissues lies within 10 μs of acquisition time (equivalent to 15 mm of radial extent of the arterial tissue). In a multiple-record mode, samples equivalent to 10 μs of acquisition time can be acquired and transferred to the digitizer memory and the acquisition control can re-arm itself to respond to the next trigger event. Therefore, in a scenario involving high speed imaging, additional A-lines can be obtained without the need for additional memory.

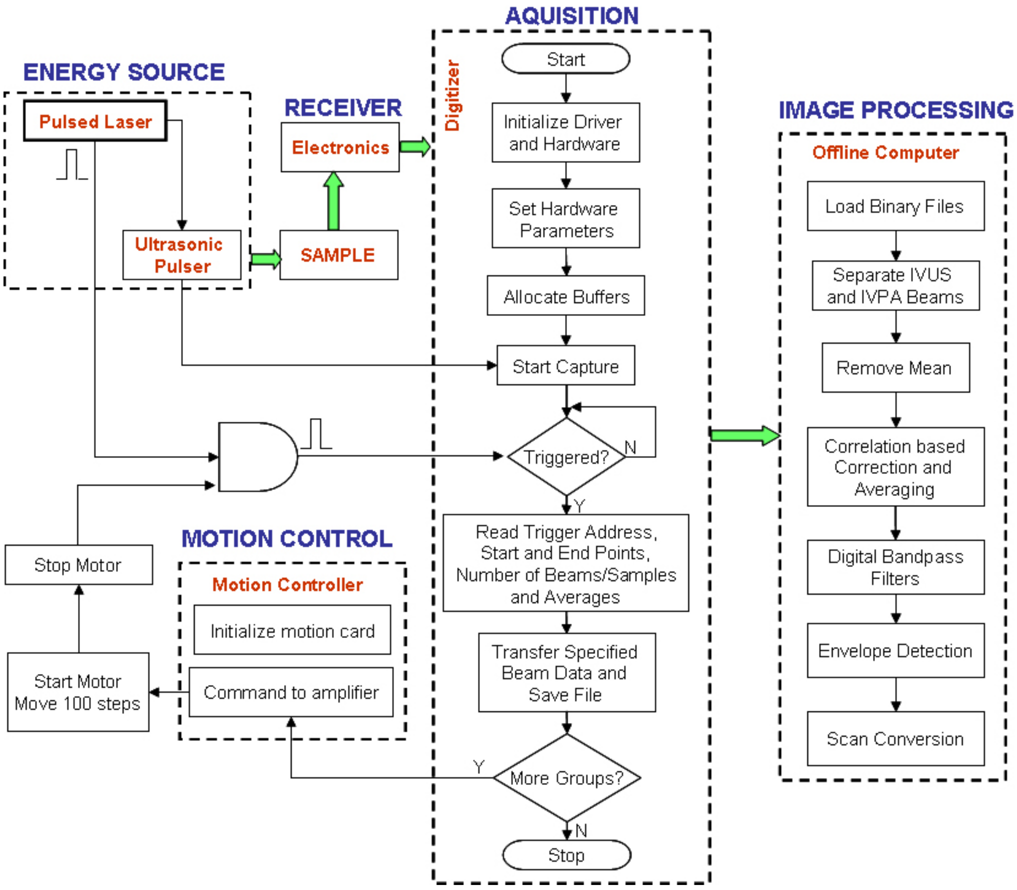

Figure 2.6: An overview of the control flow in the laboratory prototype of a combined IVUS/IVPA imaging system.

2.2.6 Post-acquisition image processing

The IVUS and IVPA radiofrequency signals were acquired and stored as files in the binary format. The images were processed through the following steps (Fig. 2.6). Initially, the ultrasound and the photoacoustic radiofrequency signals in the acquired records were separated using the delay employed in the experiment. Then, the mean of the unprocessed signals were subtracted from the original data. In our experiments, we acquired multiple A-lines at the same spatial location for averaging (typically 20). A sub-sample shift in the signals during the digitization process could alter and degrade the quality of the radiofrequency signals giving rise to image artifacts. Therefore, we utilized a cross-correlation based method to identify the sub-sample shift and align the signals. Following the correction and alignment of the signals, averaging was performed on the A-lines. The cross-correlation method of averaging reduced the image artifacts by preserving the amplitude of the ultrasound and photoacoustic signals. Subsequently, the signals were filtered using finite impulse response digital band pass filters. The passband for the filters was chosen based on the bandwidth of the signals. Indeed, a broad passband (22 MHz – 45 MHz) was utilized for a broadband photoacoustic response that contained a lot of low frequency components. The pass-band employed for the IVUS echoes was smaller (28 MHz – 45 MHz) due to a narrower bandwidth of the ultrasound signals. The envelope detection process of the filtered signals involved the use of a Hilbert transformer to obtain the analytical signals. One way to visualize the image is to display the image in the polar system of coordinates. However, the analytical signals need to be displayed in a format consistent with the scanning geometry. Therefore, the signals were scan-converted through interpolation to the cartesian system of co-ordinates.

In addition to the general IVUS and IVPA image formation method, other techniques were employed to further process the IVPA images. The photoacoustic response from the tissues may occur at regions outside the structural boundary. A reason for these additional signals could be the ringing effect due to a strong optical absorber. Therefore, there was a need to spatially localize the photoacoustic response within the structural content of the artery. To identify the structure of the arterial tissue, a boundary detection algorithm was applied to the IVUS image. The photoacoustic signals outside the boundary were masked based on the structure identified in the IVUS image. Further, to compensate for the near exponential attenuation of light due to absorption and scattering effects, time gain compensation (TGC) was applied to the photoacoustic response. The effective attenuation coefficient to determine the TGC curve was chosen based on the values of absorption coefficient and reduced scattering coefficient reported in the literature [9-12].

2.3 EVALUATION OF THE COMBINED IVUS/IVPA IMAGING SYSTEM

2.3.1 Phantoms

Several phantoms were designed to evaluate the performance of our IVUS/IVPA imaging system. A carbon fiber with a diameter measuring 9 μm was chosen as the wire phantom for the studies to determine the axial and lateral resolution of IVUS and IVPA imaging (Fig. 2.7(a)). The carbon fiber was chosen by reason of its size, strong absorber of light and reflector of ultrasonic waves.

The custom-built imaging system was further evaluated using an arterial vessel mimicking phantom with an embedded inclusion. Poly vinyl alcohol (PVA) cryogel was chosen as the material for arterial vessel phantoms since PVA can be easily molded into preferred shapes, is non-toxic and durable with a long shelf life. The superfine PVA crystals (Celvol 165SF, Celanese Chemicals) were mixed in water and heated to 90°C with constant stirring. Several weight percentages were tested and 8% PVA solution was used to produce elastic and durable phantoms. The 8% PVA solution was poured and molded into the desired arterial vessel shape by freezing and thawing for 4 cycles (each cycle consisted of freezing at -15ºC for 12 hours and thawing at room temperature for 12 hours). The number of freeze-thaw cycles affects the strength of polymerization. Silica particles (0.4% and 15 µm diameter) were added to the PVA solution to mimic the ultrasound and optical scattering properties of tissues [13]. Areas of optical absorption were created by embedding a 1.9 mm diameter cylindrical PVA inclusion of 0.08%, 30 µm fine graphite particles. The fabricated 8 mm diameter phantom with a 3 mm diameter lumen is shown in Fig. 2.7(b).

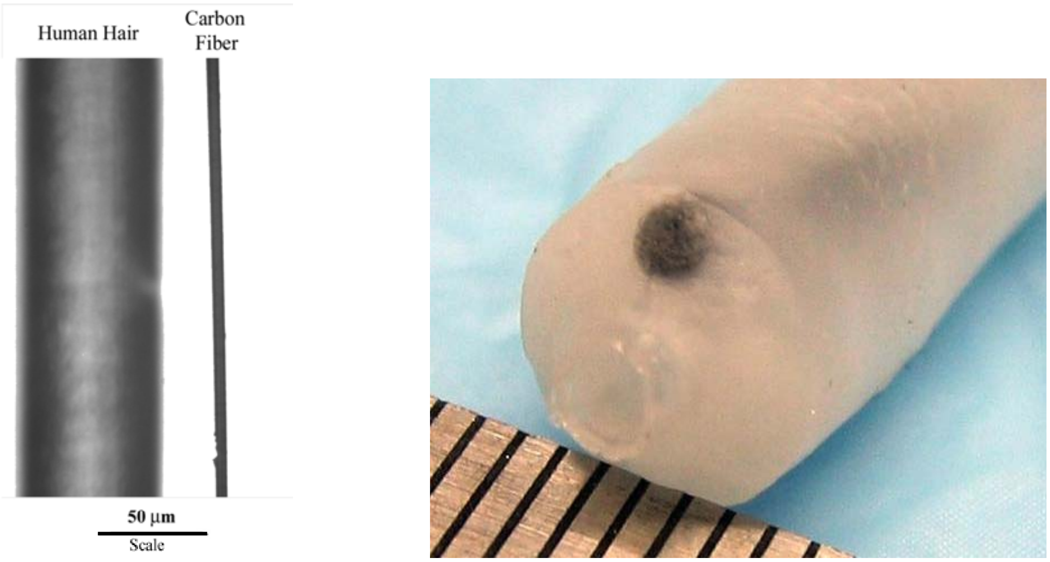

(a) (b)

Figure 2.7: Phantoms for the imaging and performance evaluation of the combined IVUS/IVPA imaging system. (a) A microscopic image (40x) of a carbon fiber “wire” phantom with a diameter of 9 µm and, (b) Photograph of the 8 mm diameter PVA vessel phantom with a 1.8 mm graphite inclusion embedded in the wall.

2.3.2 IVUS and IVPA imaging of a wire phantom

The performance of our combined IVUS and IVPA imaging system was determined by scanning a specially designed "wire" phantom where a cross-section of a 9 μm diameter carbon fiber was used to approximate a point target for photoacoustic and ultrasound impulse response measurements. The carbon fiber acts as both an optical absorber and an ultrasound reflector. The fiber, placed parallel to the imaging catheter at a depth of 3 mm, was directly irradiated by a 3 mm diameter laser beam. The laser beam was oriented such that it would not interfere directly with the IVUS transducer. A cross-sectional, combined IVUS and IVPA scan was obtained simultaneously by rotating the transducer in the catheter using a stepper motor. One complete rotational scan contained 500 A-lines of combined IVPA/IVUS response. The trigger for the image acquisition was provided by the laser source operating at 20 pulses per second. The radiofrequency IVPA and IVUS signal from the wire phantom are presented in Fig. 2.8.

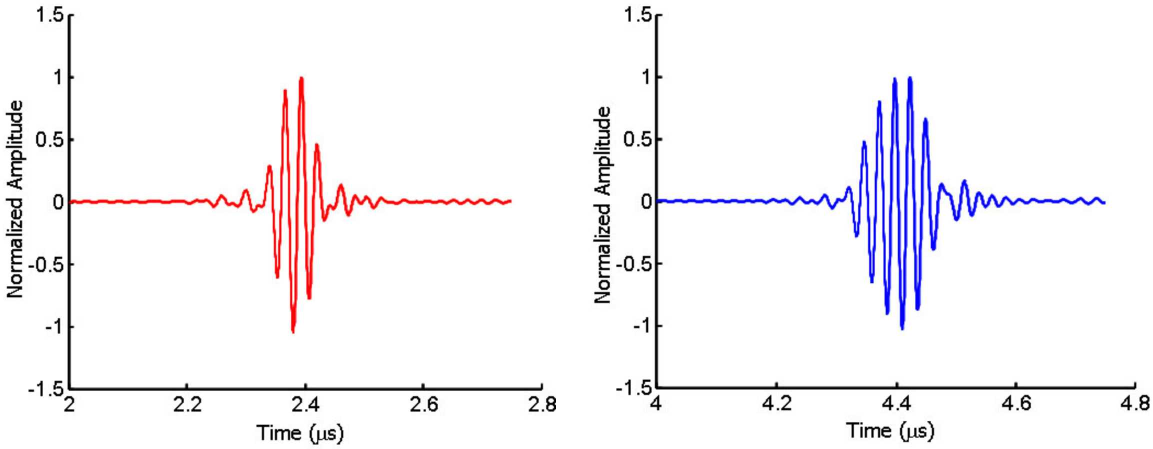

(a) (b)

Figure 2.8: Representative (a) IVPA and (b) IVUS radiofrequency signals from a wire phantom.

The IVUS and IVPA B-Scan images of the wire phantom are presented in Fig. 2.9 and Fig. 2.10, respectively. The images in the polar (R,θ) system of coordinates are shown in Fig. 2.9(a) and Fig. 2.10(a). These images cover a radial distance of 4.5 mm and a lateral angular coverage of 360° corresponding to one complete rotation of the transducer element. The IVPA and IVUS images after being scan converted to the cartesian (x,y) system of coordinates are presented in Fig. 2.9(b) and Fig. 2.10(b) respectively. As can be observed from these images (both in the polar and cartesian system of coordinates) there is diffraction limited lateral over-estimation of the point target. Figures 2.9(c) and 2.10(c) represent the magnified IVUS and IVPA images of the signal from the carbon fiber. The axial (vertical) profile of the IVUS echo and IVPA response from the wire target is plotted in the Figs. 2.9(d) and 2.10(d), respectively. The full-width-half-maximum (FWHM) for both the ultrasound and photoacoustic axial profiles gives an estimate of the resolution.

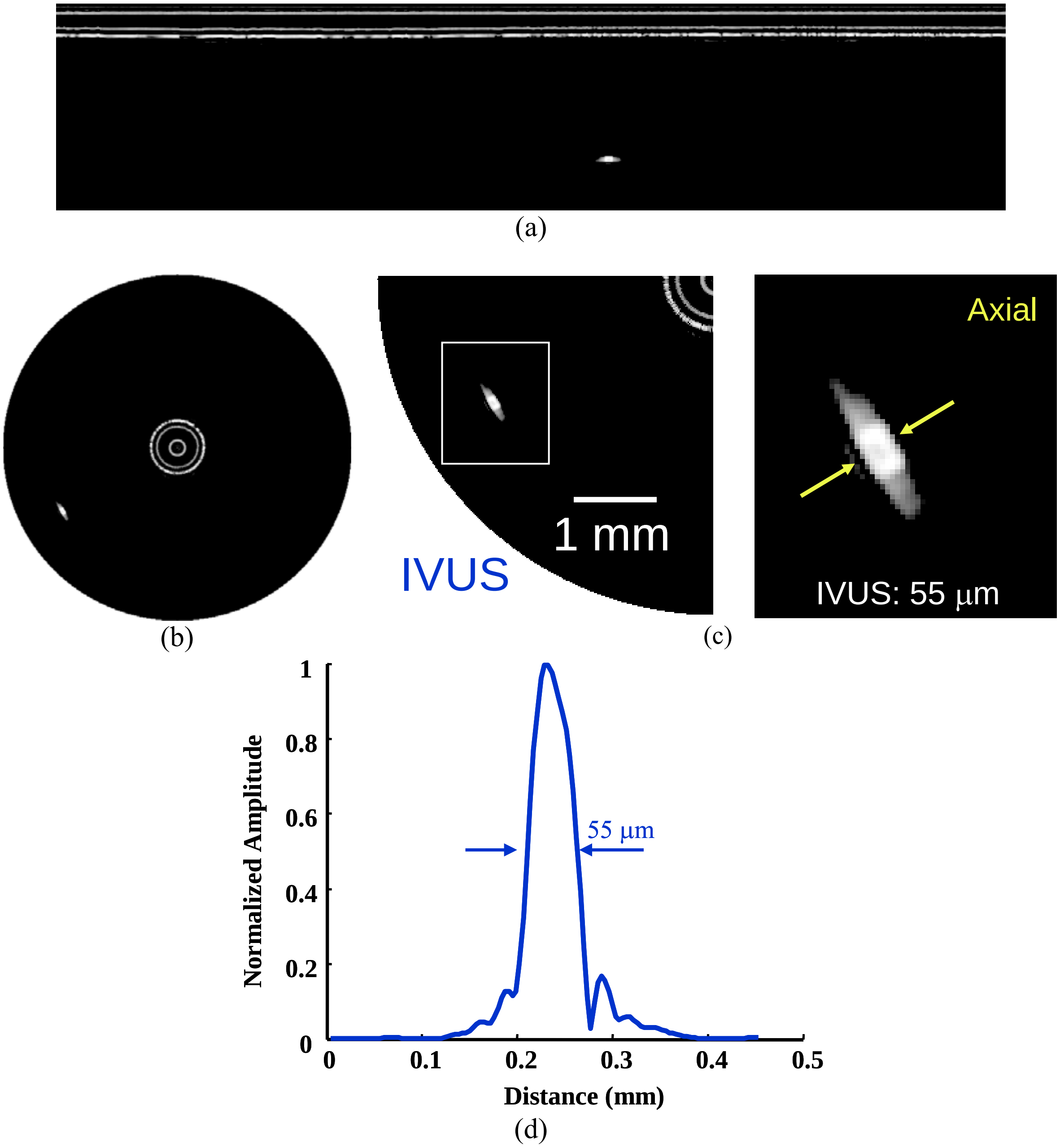

Figure 2.9: Intravascular ultrasound imaging of the wire phantom. (a) B-Scan IVUS image in the polar system of co-ordinates, (b) Scan converted B-Scan IVUS image in the Cartesian system of co-ordinates, (c) The magnified image of the wire phantom and (d) plot of the vertical profile of the signal from the wire phantom.

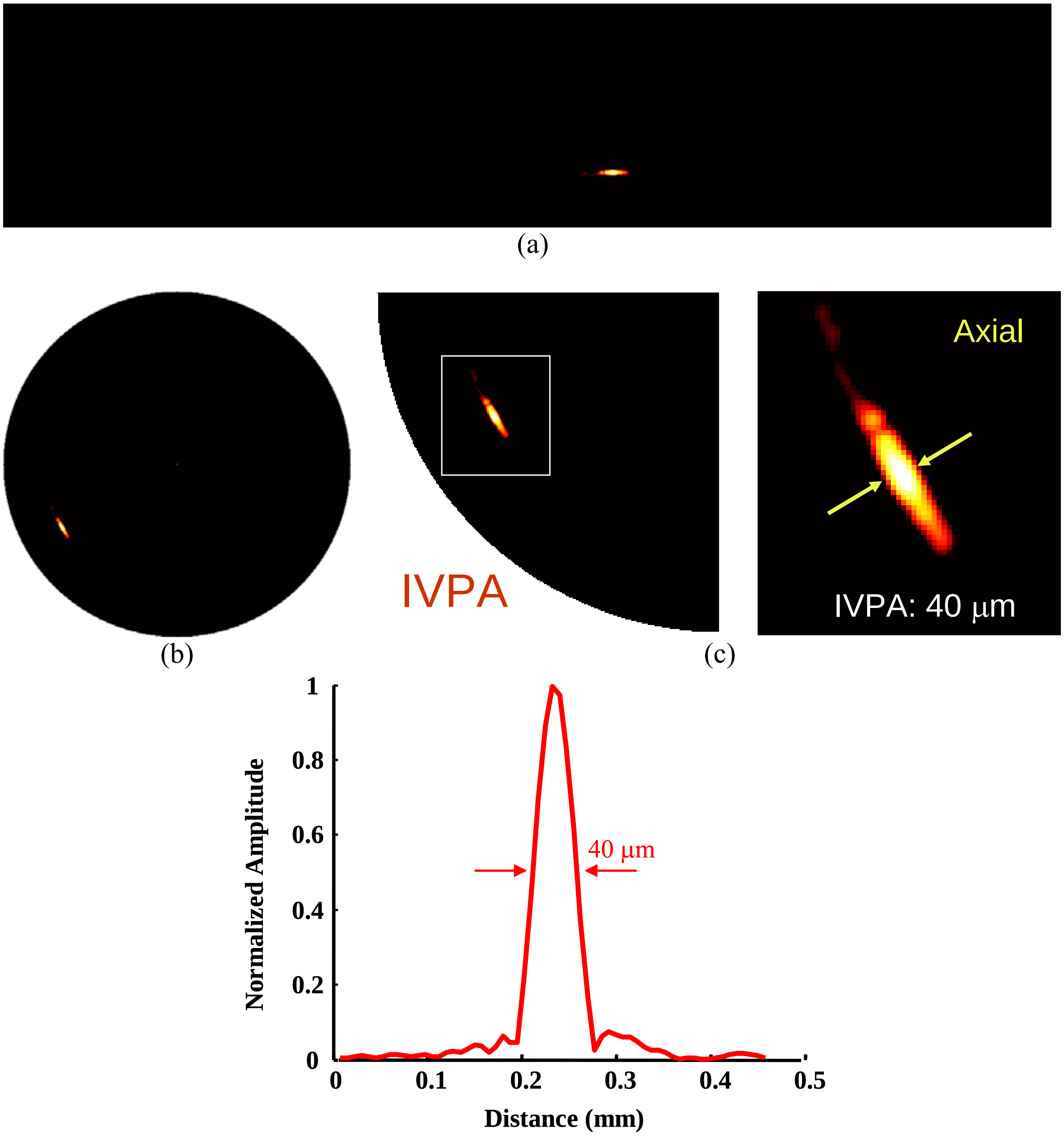

(a)

(b)

(c)

(d)

Figure 2.10: Intravascular photoacoustic imaging of the wire phantom. (a) B-Scan IVPA image in the polar system of co-ordinates, (b) Scan converted B-Scan IVPA image in the Cartesian system of co-ordinates, (c) The magnified image of the wire phantom and (d) plot of the vertical profile of the signal from the wire phantom.

2.3.3 IVUS/IVPA imaging of arterial phantom

The arterial vessel phantom was placed inside a water tank. An IVUS imaging catheter was inserted into the lumen of the phantom while the laser irradiated the vessel from outside.

As described previously, the alignment of the ultrasonic and the laser beams is critical to obtain co-registered images. The graphite inclusion in the PVA phantom absorbs the laser light and produces photoacoustic signals. Initially, the phantom was positioned such that the inclusion was in the direct path of the optical beam. Subsequently, alignment was performed by observing the position at which the maximum amplitude of the photoacoustic signal is observed. Following the alignment, scanning was performed by incrementally rotating the phantom.

The delay between IVPA and IVUS imaging modes was chosen such that there was no overlap between the photoacoustic signal from the inclusion and the ultrasound response. Digital bandpass filter was applied to the A-scans to remove noise. The envelope detected signals were scan converted to produce spatially co-registered IVUS and IVPA images containing at least 250 beams.

The results of intravascular photoacoustic (IVPA) and intravascular ultrasound (IVUS) imaging of the arterial vessel mimicking phantom are presented in Fig. 2.11. All images in the figure are displayed over a 10 mm field of view, i.e., each image has a radius of 5 mm. The cross-sectional IVUS image of the cylindrical phantom is shown in Fig. 2.11(a) at a display dynamic range of 40 dB. The bright echo in the center of the image corresponds to ultrasound signal reflected from the catheter sheath. The nearly uniform IVUS image clearly shows the geometry of the phantom and variations of the wall thickness. However, there is no sufficient acoustic contrast to differentiate the inclusion from the rest of the phantom in the IVUS image. Also noticeable in this image are motion artifacts where there is an abrupt difference between two adjacent beams (e.g., at ~7 o'clock and 8:30 o'clock) – these artifacts are related to irregular rotation of the elastic phantom.

In contrast to the IVUS image, the IVPA image of the phantom in Fig. 2.11(b) displayed with a dynamic range of 35 dB clearly shows the inclusion located between 9 o'clock and 10:30 o'clock. The photoacoustic response from the inclusion with elevated optical absorption dominates the image while the other parts of the phantom that are predominantly scattering have small or no photoacoustic signal. In this specific case, the IVPA image, therefore, demarcates the inclusion but does not display the structural features depicted in the IVUS image. The circle at the center of the IVPA image in Fig. 2.11(b) indicates photoacoustic signal produced by the laser pulses that directly interacts with the surface of the transducer element. Indeed, the metal coating of the transducer absorbs light and produces measurable photoacoustic signal.

The IVPA and IVUS images are inherently co-registered, as it is clearly evident from the experimental methodology. The co-registered combined IVPA and IVUS images may better portray inclusion with higher optical absorption in the context of the structure of the vessel phantom. In Fig. 2.11(c), the photoacoustic image is overlaid on top of the IVUS B-Scan, i.e., B-Scan value is displayed if the photoacoustic signal is smaller than user-defined threshold, and vise versa. Indeed, the position and extent of the inclusion is clearly identified in the combined image.

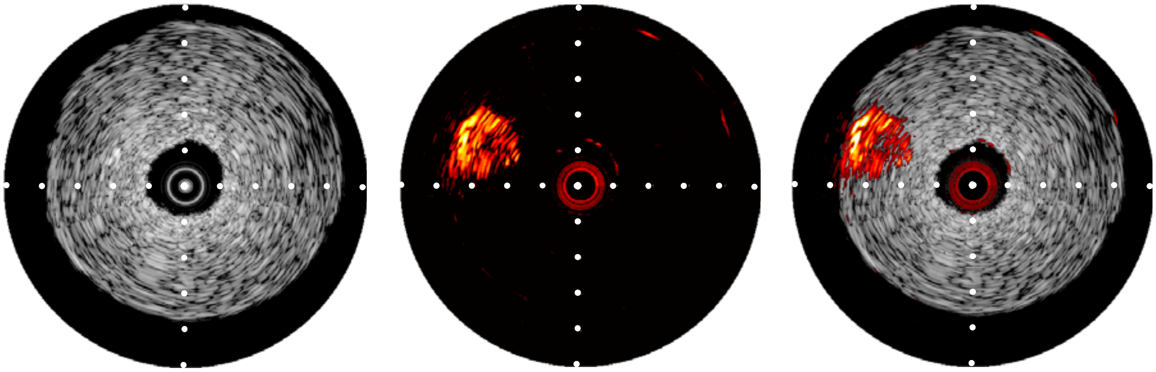

(a) (b) (c)

Figure 2.11: IVUS, IVPA and combined images of the PVA phantom with an inclusion. (a) Intravascular ultrasound (IVUS) image showing the structure of the vessel phantom. The inclusion is not clearly visible in the IVUS image. (b) Intravascular photoacoustic (IVPA) image highlights the inclusion although the underlying structure of the phantom is no longer visible. (c) Combined image demonstrating complementary nature of IVPA and IVUS. The field of view of these images is 5 mm in radius and each image consists of 250 A-lines.

2.3.4 Resolution

The axial resolution of IVPA and IVUS imaging is primarily dependent on the frequency characteristics of the transducer. Axial resolution is determined by the bandwidth, measured as the full-width-half-maximum (FWHM) of the frequency profile of an impulse response, and the acoustic wavelength [14]. As a generalization, the axial resolution can be approximated using the following relationship,

$$\Delta x_{IVUS} \propto \frac{1}{2} \cdot \frac{c}{\Delta f_{IVUS}} \tag{2.1}$$

$$\Delta x_{IVPA} \propto \frac{c}{\Delta f_{IVPA}} \tag{2.2}$$

where c is the speed of sound in the medium, Δx is the axial resolution and Δf is the bandwidth of the signal. Indeed, the above relationships in equations 2.1 and 2.2 suggest better axial resolution in IVUS imaging compared to IVPA imaging. However, the inference remains good only for a linear system where the response of the transducer element is the same for the signal transmit and receive modes. Generally, the frequency response in ultrasound and photoacoustic imaging depends on the signal transmit and receive characteristics.

In our IVUS imaging system, a -100V impulse excitation generates ultrasound with a resonance at 40 MHz determined by the finite bandwidth of the transducer. The bandwidth of the transmitted IVUS signals is significantly lower in comparison to the broadband photoacoustic response (asymmetric with larger low frequency content). The acoustic echoes generated by optical excitation (IVPA) are broadband in nature. The efficiency of photoacoustic signal generation depends on the width of the laser pulse. Short laser pulses are essential for stress confinement and generation of acoustic transients in the region of optical excitation. The duration of the laser pulse determines the bandwidth of the photoacoustic response generated from the resolution target.

Both, the ultrasound and the photoacoustic signals are received by the same IVUS transducer. However, the sensitivity of the transducer to these signals is different. In pulse-echo IVUS imaging, both transmit and receive characteristics of the transducer narrows the frequency response. In IVPA imaging, the higher sensitivity of the transducer to the lower frequencies may lead to a broader frequency bandwidth.

Therefore, the axial resolution is determined by the round-trip effect as shown in the equations 2.1 and 2.2 and the transducer transmit-receive characteristics in the IVUS and IVPA imaging modes. If the effect of sensitivity of the transducer is predominant, then IVPA may have better resolution. On the other hand, a higher ultrasound transmit efficiency combined with the round-trip effect may result in better resolution in IVUS imaging.

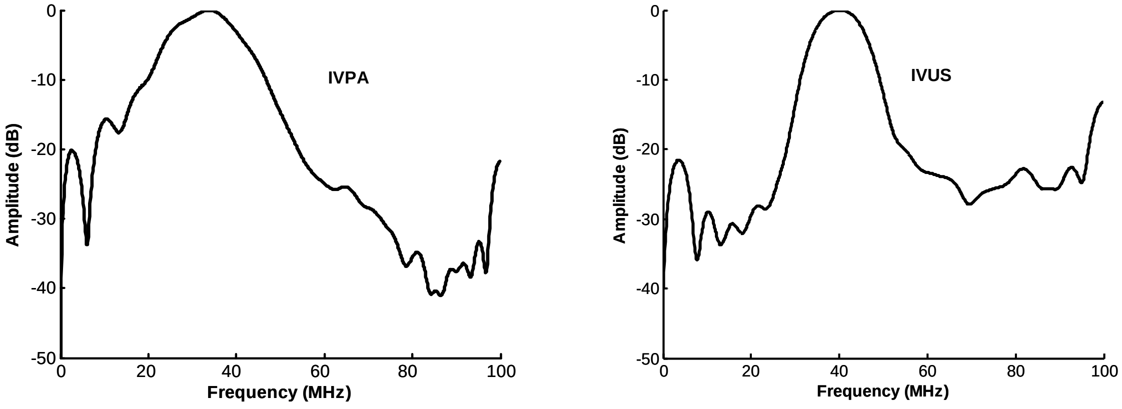

(a) (b)

Figure 2.12: Frequency spectrum of an (a) IVPA impulse response. The axial resolution as measured by the fractional bandwidth of the photoacoustic frequency spectrum of an impulse response is 38 μm. (b) IVUS impulse response. The axial resolution as measured by the fractional bandwidth of the ultrasound impulse response is 54 μm.

The frequency profile of the impulse response in IVPA and IVUS imaging from our wire-phantom studies is presented in Figs. 2.12(a) and Fig. 2.12(b) respectively. The fractional bandwidth calculated from the −6 dB width of the IVPA frequency spectrum is 63% which corresponds to 38 μm axial resolution. The fractional bandwidth for the IVUS impulse response is 37% which corresponds to an axial resolution of 54 μm. The axial resolution can also be estimated by measuring the -6 dB width of the spatial axial signal from the carbon fiber. By using this method we obtained axial resolutions of 40 μm for IVPA imaging and 55 μm for IVUS imaging respectively. Clearly, both methods resulted in similar measurements and confirmed that the axial resolution of the IVPA imaging is generally higher than that of IVUS imaging.

The IVPA/IVUS signals from the rotational scan of the wire phantom were used to obtain the beam pattern. The lateral resolution was estimated by calculating the angular width at −6 dB of the lateral beam profile. In IVUS imaging, an acoustic pulse from the IVUS transducer was backscattered from the carbon fiber and detected by the same element. In IVPA imaging, a broadband acoustic pulse was generated by interaction of laser irradiation with carbon fiber.

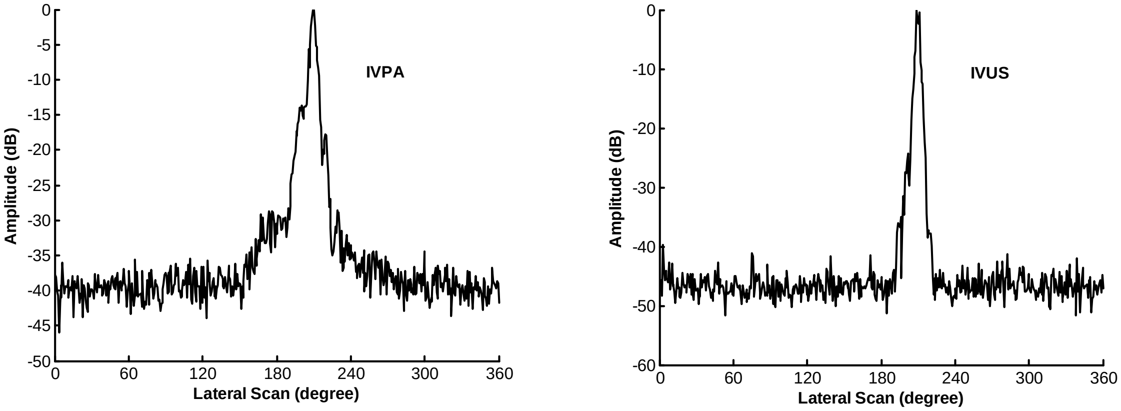

(a) (b)

Figure 2.13: Lateral scans of the wire phantom in the (a) IVPA imaging scheme, and (b) IVUS imaging scheme, plotted as the maximum signal along the respective beams. The lateral resolution as given by the −6 dB width of the lateral scan profile is 5.5^{o} in IVPA imaging and 3.2^{o} in IVUS imaging.

Lateral resolution in IVPA and IVUS imaging is diffraction limited. Since the bandwidth of a broadband IVPA signal is limited by the frequency characteristics of the IVUS transducer, the detected IVPA signal has larger frequency bandwidth centered at the lower frequency compared to IVUS signal. Therefore, the effective wavelength is increased leading to a decrease in lateral resolution of IVPA imaging. Hence, at a particular imaging depth the lateral resolution of IVUS images is expected to be better than IVPA images. The lateral resolution can be estimated from the beam profile of the signal from the point target during one complete lateral (angular) rotation. The beam profiles in the IVPA and IVUS imaging regimes are presented in Figs. 2.13(a) and 2.13(b), respectively. The −6 dB width is calculated from the respective lateral profiles. The IVPA imaging has a lateral resolution of 5.5 degrees. Due to reduced angular directivity (transmit and receive directivities) in IVUS imaging, the lateral resolution is better than IVPA imaging (receive directivity only). The lateral resolution for IVUS imaging is 3.2 degrees. Indeed, the difference in the IVUS and IVPA beam profiles was expected due to the difference in frequency content of signals detected by the transducer element.

In addition, we performed phantom imaging studies to qualitatively compare the resolution difference obtained using IVUS imaging catheters available at 20 MHz, 30 MHz and 40 MHz. Another PVA phantom with 2 inclusions embedded in the vessel wall was utilized for these studies. The scanning was performed to obtain IVUS and IVPA images from the same cross-section in the phantom. The phantom was left undisturbed throughout the entire experiment. The catheters were inserted into the lumen and the element in the IVUS catheter was pulled back a fixed distance to image the same cross-section of the phantom.

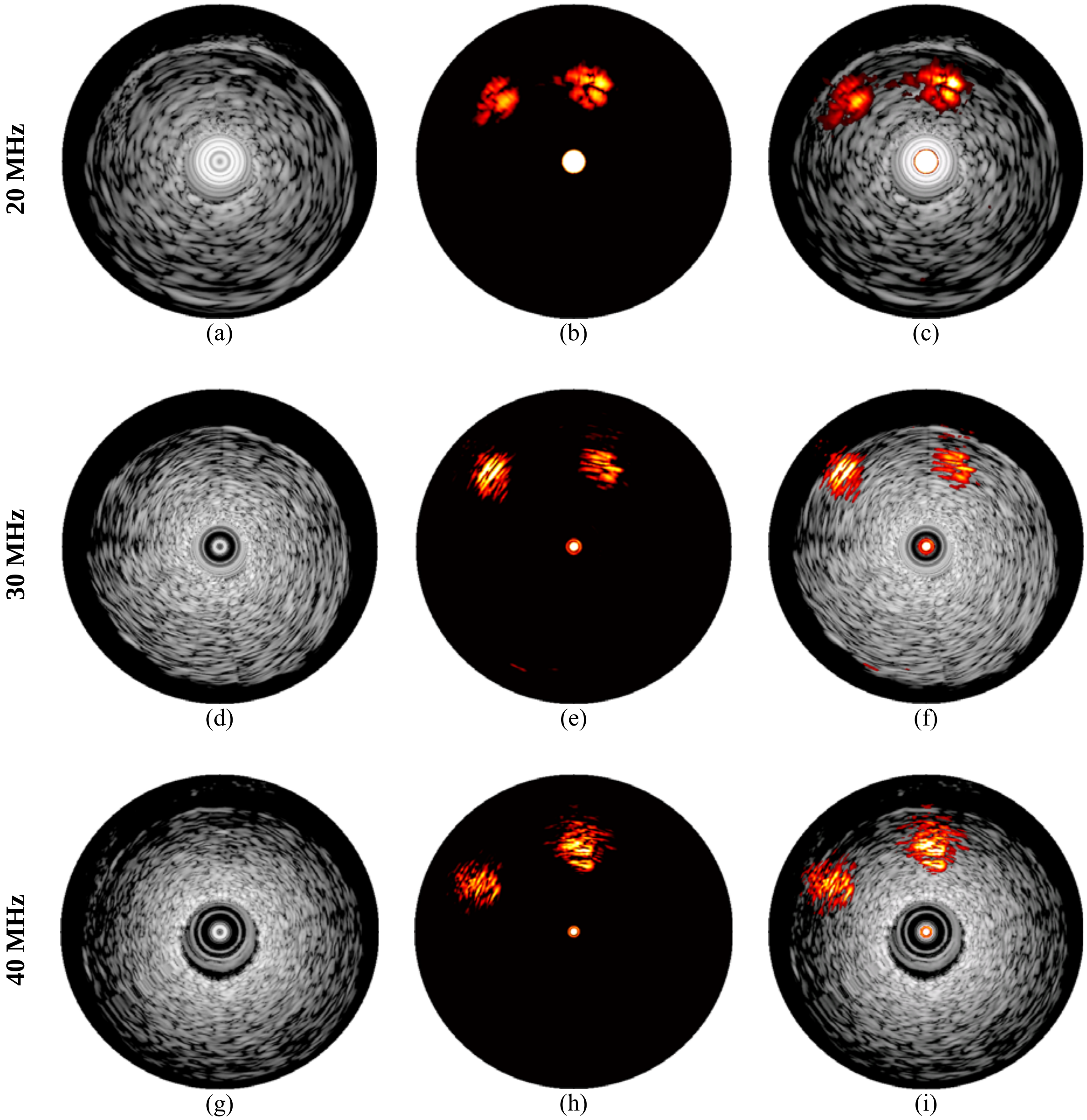

Figure 2.14 Cross-sectional IVUS (left panel), IVPA (middle panel) and combined (right panel) images of the phantom with two inclusions. Images were obtained using 20 MHz (top panel), 30 MHz (center panel) and 40 MHz (bottom panel) IVUS imaging catheters and displayed over a field of view of 9 mm in diameter.

The IVUS and IVPA images obtained using the 20, 30 and 40 MHz IVUS imaging catheters are presented in Fig. 2.14. All the images are displayed over a field of view of 9 mm, i.e., each image has a radius of 4.5 mm. The inclusions are not clear in the IVUS images, whereas the IVPA images at imaging frequencies of 20, 30 and 40 MHz clearly indicated the presence of the inclusion. Also noticeable is a difference in the magnitude of the photoacoustic signal generated on the surface of the catheter. The photoacoustic signals from the inclusion and the surface of the catheter is maximum in the Fig. 2.14(b) obtained using the 20 MHz catheter. As expected, both the ultrasound and photoacoustic images obtained with higher frequency probes (30 and 40 MHz) have better resolution compared to the IVUS probe with a lower frequency (20 MHz). The IVPA frequency spectrum plotted in Fig. 2.12(a) indicate that the photoacoustic response is dominated by low frequency content. Therefore, the signals obtained with the low frequency catheter contained higher magnitude of photoacoustic response.

The choice of the IVUS imaging catheter is an important issue for IVPA imaging. An observation not evident in these studies would be an increase in the penetration depth at lower center frequencies. The results of these studies indicate the suitability of 40 MHz IVUS imaging catheters for imaging of small sized arteries with higher resolution to visualize the plaque. However, 20 MHz catheters may be useful in studies involving large sized and thicker aortas where the penetration depth may be critical.

2.4. SUMMARY

A combined IVUS/IVPA imaging system capable of obtaining IVUS and IVPA cross-sectional images was successfully built. The IVUS catheter based intravascular photoacoustic imaging system included a pulsed laser excitation incident on the sample from outside. Therefore, at present the prototype is capable of imaging phantoms and excised samples of arterial vessel tissues. We tested the system through phantom imaging studies and determined the spatial resolution characteristics.

2.5. REFERENCES

[1] J. J. Niederhauser, M. Jaeger, and M. Frenz, "Comparison of lsaer-induced and classical ultrasound," *Proceedings of the SPIE The International Society for Optical Engineering*, vol. 4960, pp. 118-23, 2003.

[2] X. Wang, Y. J. Pang, G. Ku, G. Stoica, and L. V. Wang, "Three-dimensional laser-induced photoacoustic tomography," *Optics Letters*, vol. 28, pp. 1739-41, 2003.

[3] J. A. Viator, B. Choi, M. Ambrose, M. Spanier, and J. S. Nelson, "In vivo port-wine stain depth determination with a photoacoustic probe," *Applied Optics*, vol. 42, pp. 3215-24, 2003.

[4] R. G. M. Kolkman, E. Hondebrink, W. Steenbergen, and F. F. M. de Mul, "In vivo photoacoustic imaging of blood vessels using an extreme-narrow aperture sensor," *IEEE Journal of Selected Topics in Quantum Electronics*, vol. 9, pp. 343-6, 2003.

[5] C. G. A. Hoelen, F. F. M. de Mul, R. Pongers, and A. Dekker, "Three-dimensional photoacoustic imaging of blood vessels in tissue," *Optics Letters*, vol. 23, pp. 648-50, 1998.

[6] A. A. Oraevsky, A. A. Karabutov, S. V. Solomatin, E. V. Savateeva, V. A. Andreev, Z. Gatalica, H. Singh, and R. D. Fleming, "Laser optoacoustic imaging of breast cancer in vivo," *Biomedical Optoacoustics II in the Proceedings of the SPIE*, vol. 4256, pp. 6-15, 2001.

[7] Z. A. Fayad and V. Fuster, "Clinical imaging of the high-risk or vulnerable atherosclerotic plaque," *Circ Res*, vol. 89, pp. 305-16, 2001.

[8] ANSI, *American National Standard for Safe Use of Lasers, ANSI Z136.1*. Orlando: Laser Institute of America, 2000.

[9] M. J. C. van Gemert, A. J. Welch, S. L. Jacques, Q. F. Cheong, and W. M. Star, "Light distribution, optical properties, and cardiovascular tissues," in *Lasers in cardiovascular medicine and surgery: Fundamentals and techniques*, G. S. Abela, Ed. Norwell, MA: Kluwer Academic Publishers, 1990.

[10] M. J. van Gemert, R. Verdaasdonk, E. G. Stassen, G. A. Schets, G. H. Gijsbers, and J. J. Bonnier, "Optical properties of human blood vessel wall and plaque," *Lasers Surg Med*, vol. 5, pp. 235-7, 1985.

[11] "Optical properties of aorta compiled by Steven Jaques, Oregon Medical Laser Center," http://omlc.ogi.edu/spectra/aorta/index.html.

[12] W. Cheong, S. A. Prahl, and A. J. Welch, "A review of optical properties of biological tissue," *IEEE J. Quantum Electronics*, vol. 26, pp. 2166-2183, 1990.

[13] A. Kharine, S. Manohar, R. Seeton, R. G. Kolkman, R. A. Bolt, W. Steenbergen, and F. F. de Mul, "Poly(vinyl alcohol) gels for use as tissue phantoms in photoacoustic mammography," *Phys Med Biol*, vol. 48, pp. 357-70, 2003.

[14] N. A. Cohn, S. Y. Emelianov, M. A. Lubinski, and M. O'Donnell, "An elasticity microscope. Part 1: Methods," *IEEE Trans Ultrason Ferroelectr Freq Control*, vol. 44, pp. 1304-1319, 1997.

Chapter 3: Intravascular Photoacoustic Imaging: *ex vivo* studies

3.1 ABSTRACT

Assessment of the composition of high risk plaques is essential to select appropriate treatment options for atherosclerosis. Current research efforts are aimed at improving the image resolution as well as providing functional information required to identify vulnerable plaques. High frequency intravascular ultrasound (IVUS) imaging has been successful in obtaining high resolution tomographic images of the arterial vessel wall and plaque. However, the ability of IVUS to identify the composition and spatially localize the vulnerable plaque has been limited. Combined with IVUS, intravascular photoacoustic (IVPA) imaging may improve plaque detection and differentiation. The contrast in IVPA imaging arises from the difference in optical absorption between the different tissue constituents. In these ex vivo tissue studies, we evaluate the ability of IVPA imaging to image a lipid filled atherosclerotic lesion. At an optical illumination wavelength of 532 nm, the IVPA image could detect the lipid rich plaque. The results correlated well with histology and also showed promise in the identification of the fibrous cap and the plaque containing foamy macrophage cells.

3.2 INTRODUCTION

Generation of acoustic waves by absorbed photons – the photoacoustic effect [1] can be employed to interrogate the structure and assess composition of biological tissues. The thermoelastic effect in response to the deposition of optical energy by a short-pulsed laser generates photoacoustic transients. A photoacoustic (or optoacoustic) image is obtained by ultrasonically detecting the laser induced acoustic waves [2-4]. The optical absorption distribution in a photoacoustic image is often indicative of the physiological and pathological state of the tissue. For example, the higher absorption of light by hemoglobin in the proliferative neovasculature compared to the adjacent tissues may be useful in detecting tumors [5]. The high resolution localization of tissue structures by the photoacoustic technique could also find useful application in the imaging of vulnerable atherosclerotic plaques [6].

Generally, during hypercholesterolemic conditions, atherosclerotic plaques build up on the wall of the arteries and cause a stricture in the lumen. The resulting stenosis is visualized on an angiogram through radiographic images. However, angiographic studies have also demonstrated the ambiguity in the relationship between the culprit lesion and stenosis that cause fatal outcomes [7, 8]. Indeed, plaque rupture leading to acute coronary syndrome (ACS) could also occur in arteries not revealing significant stenosis in an angiogram. These high risk plaques, also called vulnerable plaques are usually characterized by the endothelial dysfunction, lipid deposition, the presence of a fragile fibrous cap and the accumulation of inflammatory cells [9, 10].

The initiation of the disease involves the elevation and modification of low density lipoproteins (LDL) causing injury to the endothelium and underlying smooth muscle. The internalization of the modified LDL by macrophages and subsequent accumulation of cholesterol esters gives rise to the formation of foam cells [11, 12]. The inflammatory reaction in the blood vessel wall can result in weakening and rupture of the fibrous cap and is associated with clinical complications resulting in either myocardial infarction or stroke [13-15]. The recruitment of monocyte-derived macrophages and lymphocytes from the blood and the release of hydrolytic enzymes, cytokines, chemokines and growth factors may aggravate the inflammatory process[16, 17]. The enzymes released during inflammation could digest the extracellular matrix proteins that would further accentuate the process. Furthermore, the presence of metalloproteinase [18] and collagen [19] may influence the stability of an atherosclerotic plaque. Therefore, important criteria in the diagnosis of atherosclerosis include detection of the lipids, the amount and type of collagen in the fibrous cap and presence of inflammatory macrophage cells. The treatment options are largely dependent on the type and composition of the vulnerable plaques. Consequently, imaging techniques are required not only to detect the plaques based on structural changes but also to differentiate them with respect to activity and composition [9].

Currently several imaging techniques including optical coherence tomography, magnetic resonance imaging, ultrafast computed tomography, thermography, angioscopy, Raman spectroscopy and intravascular palpography are under development to study the high risk plaques and each one has several advantages and limitations [20]. However, none of the techniques have made a significant clinical impact and angiography continues to be the gold standard for plaque identification. Although intravascular ultrasound (IVUS) appears to be the most advanced and clinically applicable tool for plaque imaging, the technique needs improvement in the ability to assess vulnerable plaques. Intravascular photoacoustic (IVPA) imaging may have the potential to distinguish arteries with rupture-prone plaques from normal vessels. Tomographic cross-sectional photoacoustic images of the arterial wall using a high frequency intravascular ultrasound (IVUS) imaging catheter have already been demonstrated [21]. Atherosclerotic plaque components may include lipid, macrophage, elastin, collagen, calcium, and hemoglobin. The plaque components exhibit unique wavelength-dependent optical absorption. Therefore, the resulting variation in the magnitude of the photoacoustic response may provide the contrast necessary for the detection of vulnerable plaques. Further, a combination of IVUS and IVPA imaging is expected to help in the morphological and functional assessment of atherosclerotic plaques and enhance the utility of IVUS imaging

[22]. In this study, the prototype IVPA imaging system was utilized to obtain photoacoustic cross-sectional images of the aorta. Specifically, we performed *ex vivo* imaging studies and evaluated the ability of the IVPA technique to detect vulnerable plaque. For this purpose, an animal model of atherosclerosis with lesions containing lipids internalized as macrophage foam cells was utilized. The imaging was also performed on the control tissue samples.

3.3 MATERIALS AND METHODS

3.3.1 Animal model of atherosclerosis

The IVPA imaging experiments were performed on a well characterized animal model of atherosclerosis. Cholesterol-fed rabbits are classical models for the study of lipoproteins and atherosclerosis [23]. Generally, the variation in the dietary regimen will induce lesions with varying severity. In rabbits susceptible to hypercholesterolemia, lesion development starts with the early increase of focal arterial low density lipoproteins, followed by sub-endothelial deposits of extracellular lipids and cytosolic lipid droplets of smooth muscle cells. The initial fatty streaks quickly develop into intimal lesions containing macrophage derived lipid-filled foam cells. In three months, the lesion progresses to advanced fatty streaks with equal number of foam cells and spindle shaped cells and finally to more complex fibrous plaques and advanced atheromatous lesions.

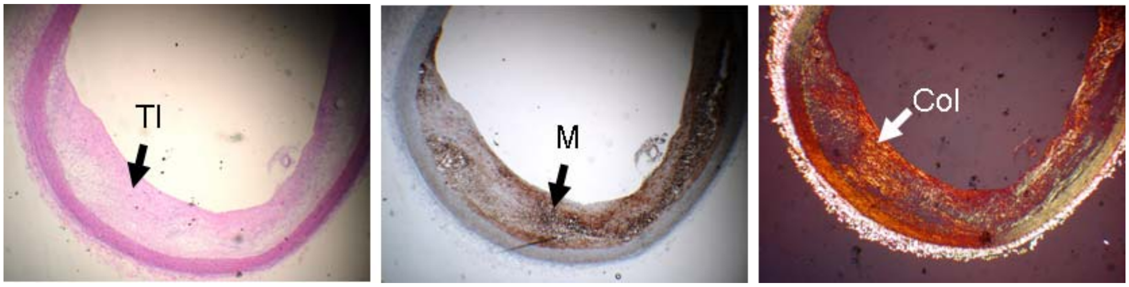

Figure 3.1: Rabbit model of atherosclerosis. Histological sections (H&E, RAM11 and Picrosirius red) of the rabbit thoracic aorta with plaque. The rabbit subjected to a 1-year, low cholesterol dietary regimen contained intermediate plaques with a lipid laden thickened intima (TI), macrophage foam cells (M) and fibrous collagen type I (Col).

The degree and type of lesions depends on the dietary regimen administered to the rabbit models. A high cholesterol diet (1-4% or more) result in rapid development of lesions with a lipid core and macrophage enriched foamy lesions. The lesions originate in the aortic arch and are also found in the thoracic aorta. A milder dietary regimen (<0.2% cholesterol) fed over a longer period of time (5-6 months) induce more complex lesions that more closely resemble those found in humans. The lesions have extracellular matrix development, large number of smooth muscle cells, and cholesterol crystals typical of advanced human atherosclerotic and vulnerable plaques [24-26]. These lesions could end up as a mixed plaque with fibrous and cellular components in addition to lipid deposits. In this study, we chose a mild dietary regimen where the rabbits were fed on a low cholesterol diet (0.15%) over a long period of time (12 months) [24, 25, 27, 28]. The 1 year old New Zealand rabbits were placed on a cholesterol diet to produce proliferative fibro-cellular lesions [29]. The histological cross-section of the atherosclerotic rabbit aorta utilized in our studies is presented in Fig. 3.1. Typically, our animal model of atherosclerosis developed diffused plaques with a thickened intima, lipids encapsulated in macrophages as well as some free lipids and fibrous collagen of type I. In addition, a control rabbit was placed on a normal diet for the same period of time.

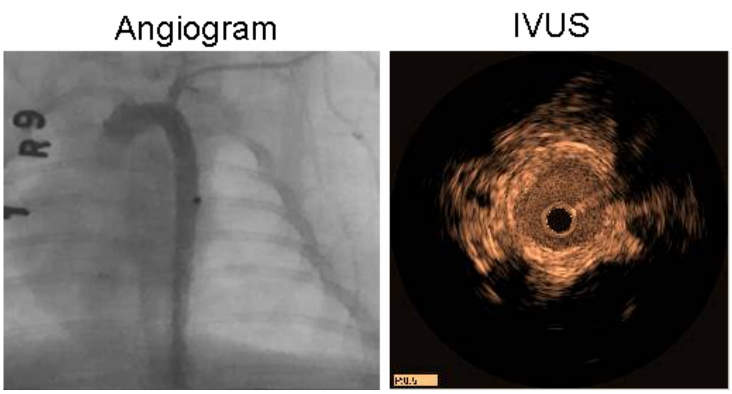

Figure 3.2: Representative images of the angiogram and real-time IVUS scan performed prior to the ex vivo IVUS/IVPA imaging of plaques.

The rabbits were pre-anesthetized and placed on a small animal laboratory ventilator. An IVUS imaging catheter on a guide wire was inserted through a 4-French sheath placed in the femoral artery. The imaging transducer was positioned below the aortic arch visualized with the help of a contrast-enhanced angiogram. Following the catheterization procedure, an IVUS pull-back imaging was performed (Galaxy-2 IVUS imaging system, Boston Scientific Corporation) from the thoracic to the renal region to locate the presence of suspected plaque deposition. The pull-back imaging allowed us to perform a longitudinal IVUS examination of the arterial vessel *in vivo*. Areas of pathological interest were identified and their locations noted using anatomical landmarks in the vicinity of major arterial branches. Figure 3.2 presents representative images of the angiogram and an IVUS B-scan obtained prior to euthanizing the rabbit. The rabbits were euthanized using approved protocol and the arterial sections (5 cm long) containing suspected plaques were obtained for *ex vivo* IVUS/IVPA imaging. Prior to the *ex vivo* imaging studies, the sectioned tissues were stored in saline for about 5 hours.

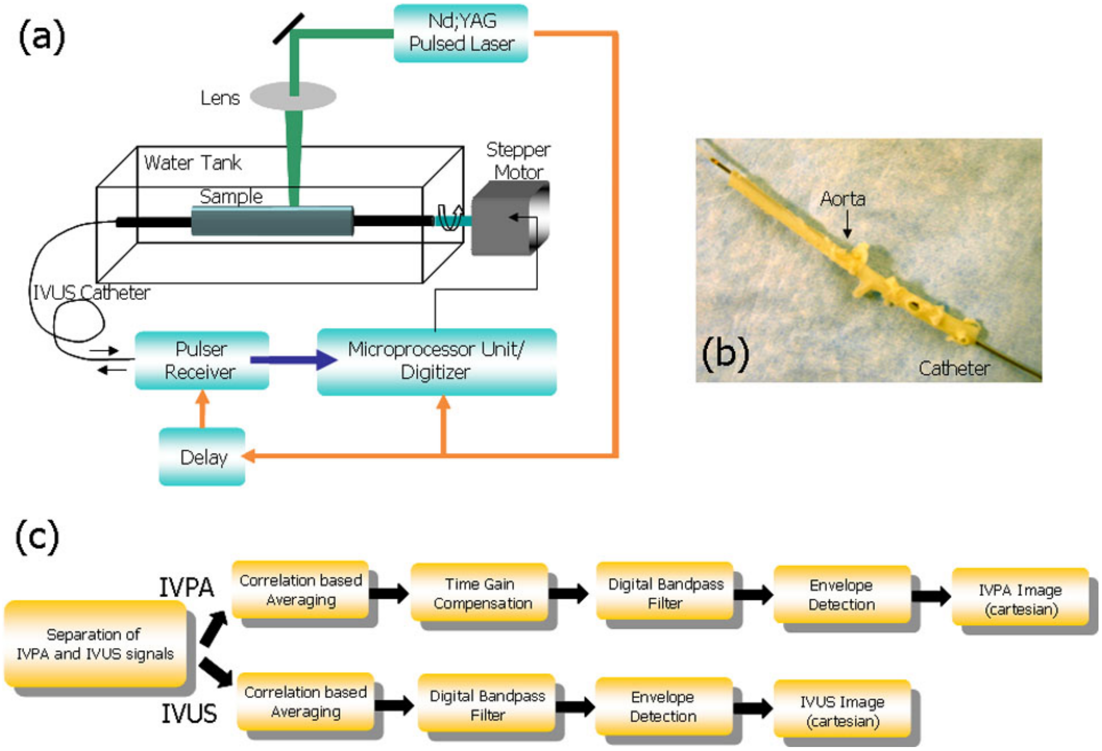

Figure 3.3: *Ex vivo* imaging of a rabbit aorta. (a) Illustration of the experimental set-up for performing ex vivo IVPA imaging in combination with IVUS imaging, (b) A photograph of the representative excised aorta with the IVUS imaging catheter inserted in the lumen and (c) Block diagram representation of the post-processing algorithm to form an IVPA image.

3.3.2 Combined IVUS/IVPA imaging of excised aorta samples

The experimental set up for the ex vivo imaging of atherosclerotic plaques is illustrated in Fig. 3.3(a). The custom-designed IVUS/IVPA imaging system is comprised of five major components, namely, the optical excitation, ultrasonic excitation, ultrasound/photoacoustic detection, motion control and signal acquisition systems.

The arterial tissue sample was immersed in a water tank to ensure acoustic coupling. A Q-switched Nd:YAG laser (Polaris II, New Wave Research, Inc.) provided optical illumination at a wavelength of 532 nm. The laser was capable of providing a maximum energy of 27 mJ per pulse and operating at a maximum repetition frequency of 20 Hz. Optical pulses for photoacoustic imaging were delivered to the artery specimen using a mirror and lens and thereby illuminating the sample from outside. The pulsed light was focused and directed to the sample such that the tissue was within the focus allowing a broad concentrated zone of illumination. The photoacoustic transients generated by the absorption of laser pulses were detected using a 2.5F, 40 MHz, single element intravascular ultrasound transducer (Atlantis™ SR PLUS, Boston Scientific Inc.) inserted in the lumen of the arterial tissue. The IVUS imaging catheter served as a common detector for both IVUS and IVPA imaging.

An ultrasonic pulser/receiver (5073PR, Panametrics, Inc.) was interfaced with the imaging system. The ultrasonic pulser provided a broadband negative electrical impulse of approximately -100V to the transducer element for IVUS imaging. The broadband spike excitation is typically employed with high frequency transducers where fast recovery time (less than 2 ns) and broadband response are required. The pulse repetition frequency (PRF) of the ultrasound pulser was controlled by the laser repetition rate. The ultrasound response was further optimized by selecting an appropriate value (2 μJ) of pulse energy. The ultrasound echoes and photoacoustic response were amplified and filtered in the analog receiver component of the pulser/receiver. The gain was adjusted to 39 dB and the pass band was set at 5 MHz - 75 MHz before the signals were digitized at a sampling frequency of 200 MHz (CS14200, Gage Applied, Inc.). The entire imaging process was initiated and controlled by the laser trigger. In addition, a delay of the ultrasound pulse for IVUS imaging using a digital delay generator allowed temporal separation of IVUS and IVPA signals. Therefore, the system was capable of obtaining simultaneous IVUS and IVPA signals from the same spatial location on the sample. After the acquisition of a single radial line of the IVUS and IVPA signal from the artery, the transducer was rotated in the azimuthal direction to the next location using a stepper motor. In this manner, a complete 360^{o} rotation was achieved to obtain the IVUS and IVPA cross-sectional image consisting of 250 radial lines.

The IVUS and IVPA signals were continuously acquired and stored for further offline processing. The steps involved in the processing of the signals to obtain IVUS and IVPA images are presented in Fig. 3.3(b). Multiple signals were obtained and averaged at each azimuthal location to improve the signal to noise ratio. In our studies, 20 averages were sufficient to detect the ultrasound echoes and photoacoustic response from the arterial tissue. The averaged signals were filtered using a finite impulse response digital bandpass filter. Pass band cut-off frequencies (25 MHz – 45 MHz) were selected based on the detection bandwidth of the transducer element. Further, the signals were envelope detected by creating the analytical signal of the input using a Hilbert transformer and then taking the absolute value of the analytical signal. During photoacoustic imaging, the distribution of optical energy in the tissue generally follows an exponential Beer's law attenuation. As a result, the magnitude of photoacoustic signal was small at spatial locations farther away from the laser incidence. An exponential time gain compensation (TGC) was applied to compensate for the decrease in the photoacoustic signal magnitude. Finally, the image in the polar (R-θ) system of co-ordinates was scan converted to the cartesian (X-Y) system of co-ordinates using a cubic interpolation method. The IVUS and IVPA images were inherently co-registered during the experimental procedure as the image acquisition was synchronized to obtain information from the same spatial location. The IVPA image was overlaid on the IVUS image to evaluate the photoacoustic response from the plaque in the context of the structure of the aortic tissue.

3.3.3 Histology of arterial tissue

After the imaging experiments, the tissue samples were marked at the location of the imaged cross-section, fixed in 10% buffered formaldehyde solution and dissected. The arterial segments were subsequently processed for routine paraffin embedding and sections of the artery were sliced at 5 μm intervals close to the imaged spot. For each segment, cross-sections were stained for collagen with Picrosirius red stain, for macrophages with RAM-11 and general morphology with Hematoxylin & Eosin (H&E). The macrophages were identified in the sections as antibodies stained brown by RAM-11. The H&E and RAM-11 stained sections were observed under the bright field microscope. The collagen is naturally birefringent due to the arrangement of the fibers and this property is enhanced by the Picrosirius Red dye. Under a polarized light, the fibers (collagen type I and III) can be distinguished based on the colored appearance. As the fiber thickness increases, the color changes from green through yellow to orange. The histological photomicrographs were correlated with the visual assessment of the IVUS and IVPA images.

3.4 RESULTS

The IVUS, IVPA and histological cross-sectional images of the aorta excised from the cholesterol fed rabbit are shown in Fig. 3.4. The 6.75 mm diameter IVUS B-scan in Fig. 3.4(a) identifies the presence of a diffused concentric plaque all along the inner circumference of the vessel. The advanced heterogeneous lesion manifests itself as thickened intima with hypo-echoic regions. The lipid-filled plaque also increases the thickness of the vessel wall. The mean thickness of the arterial wall and the diameter of the lumen are 1.4 mm and 3 mm respectively. However, the extent and the composition of the lesion are unclear. The IVPA image in Fig. 3.4(b) illustrates the photoacoustic response from the atherosclerotic aorta. A significant feature in the IVPA image is the bright signals along the surface of the plaque close to the lumen corresponding to areas of strong optical absorption in the lesion. The photoacoustic response from the lipid in the plaque is less compared to the surrounding tissue. Therefore, the lipid regions in the plaque are observed as dark regions in the intima and intimal-medial boundary. The fibrous tissue components mainly comprised of collagen is observed as bright signals. The co-registered IVUS/IVPA image is presented in Fig. 3.4(c). The combined image shows excellent correspondence between the dark regions in the IVPA image and the hypoechoic regions in the IVUS image. The histology images were obtained as close as possible to the imaged cross-section to help in understanding the IVPA response in the context of the actual composition of the plaque. The increase in the thickness of the intima with the formation of the plaque was confirmed by the Hematoxylin and Eosin (H&E) stained cross-section in Fig. 3.4(d). Further, the free lipid deposits are seen as white unstained regions in the H&E image. The higher expression of the RAM-11 antigen (dark brown) in Fig. 3.4(e) confirms the presence of dense macrophage aggregation throughout the plaque.

The polarization photomicrograph (Fig. 3.4(f)) of the tissue section stained with Picrosirius red suggests the presence of normal and thin Type III collagen (dark green) all along the vessel and focally dense deposits of the thick Type I collagen (yellow to red) in the plaque. The location of the red and orange spots in the superficial regions of the plaque may suggest the presence of a fibrous cap overlying the lipid. The histological report analysis also suggests that the plaque appears to be more cellular (lipid filled macrophage cells) than fibrous (collagen).

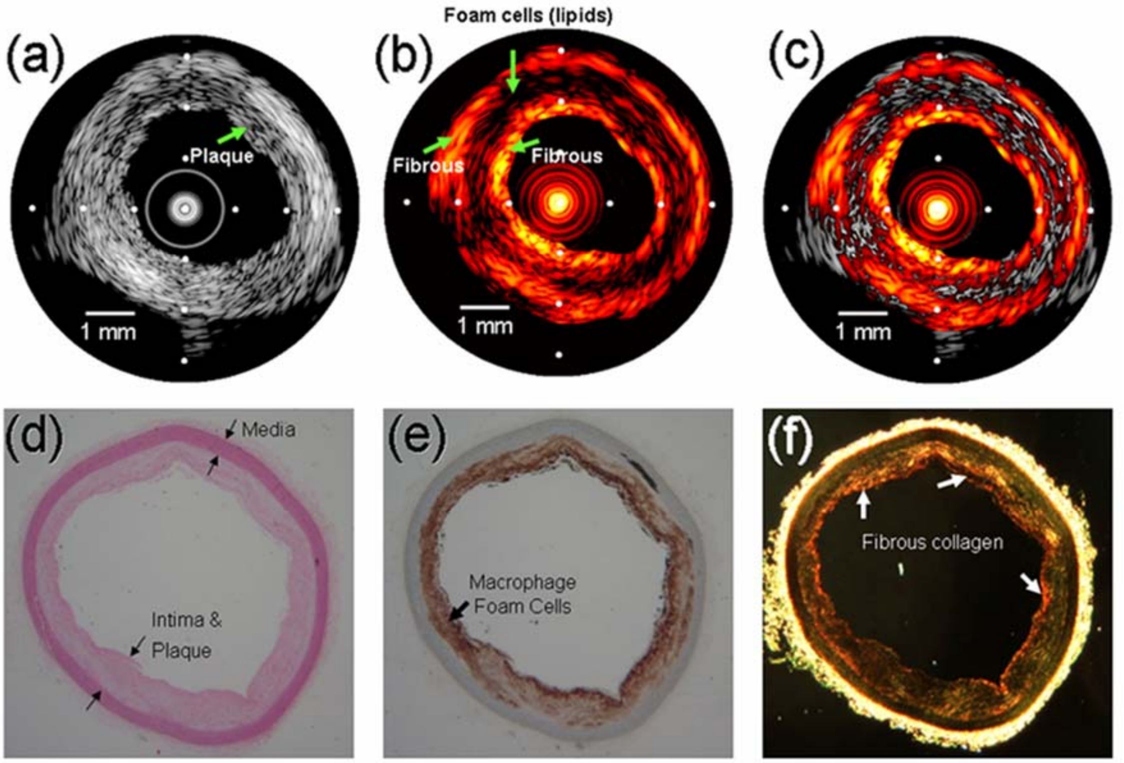

Figure 3.4: *Ex vivo* IVUS/IVPA images and histology of an advanced plaque.

(a) The IVUS image of the arterial cross-section shows a hypoechoic concentric plaque with significant structural thickening of the intima. (b) The IVPA image at 532 nm optical excitation with lipids in the plaque indicated by low photoacoustic signals. The higher photoacoustic response from the rest of the plaque corresponds to the presence of the fibrous collagenous cap infiltrated with macrophages. (c) Co-registered IVUS and IVPA image. (d) H&E stained histology image. (e) RAM-11 stained image showing the highly expressed RAM-11 antigen (dark brown) with intense macrophages embedded in the plaque. (f) Polarized image of the Picrosirius red stained cross-section showing the presence of focally dense collagen in the plaque. The overall field of view of the IVUS and IVPA image is 6.75 mm in diameter.

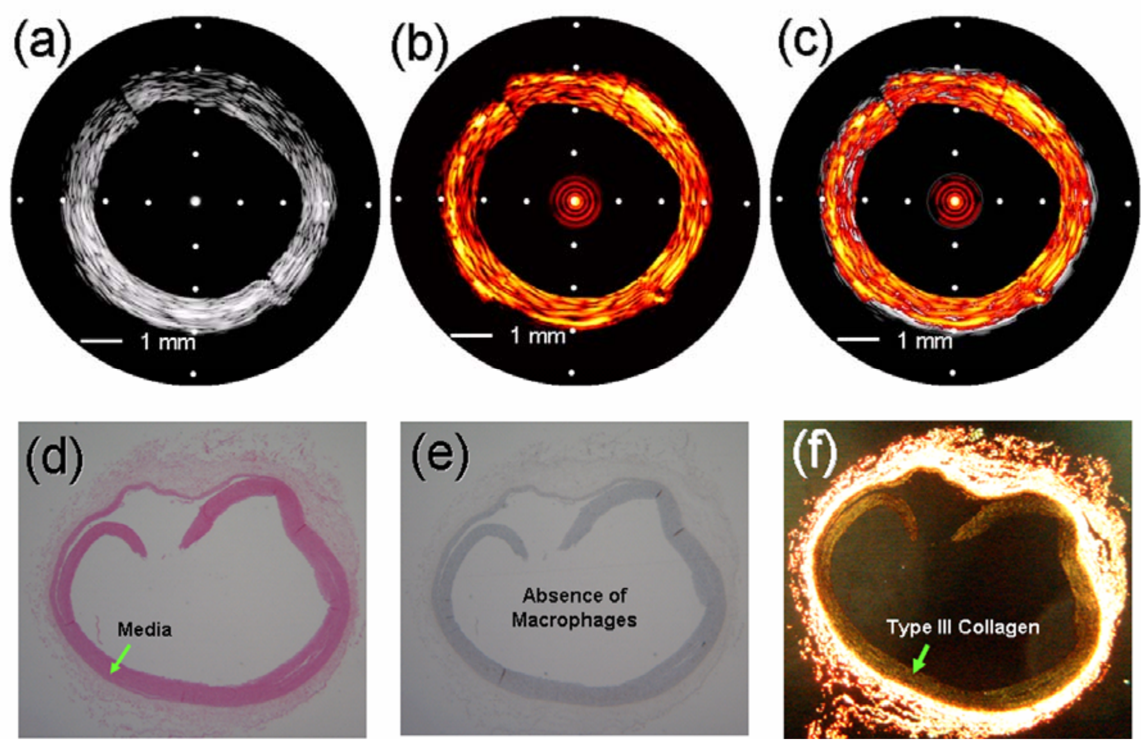

Figure 3.5: IVUS and IVPA images and the histology of the cross-section of the aorta from the control rabbit.

(a) The IVUS image of the normal rabbit aorta with no plaques. The lumen of the normal aorta is larger than the plaque-filled aorta. (b) The IVPA image details uniform photoacoustic signals from the fibrous tissue (elastin and collagen) layers. (c) The co-registered IVUS and IVPA image. (d-f) The histological images stained with Hematoxylin-Eosin (H&E), RAM-11 and Picrosirius red. The histology confirms the absence of the plaque. The overall field of view of the IVUS and IVPA images are 8.25 mm in diameter.

The IVUS/IVPA images of the normal aorta from the control rabbit, presented in Fig. 3.5, confirmed the absence of plaques. The IVUS image in Fig. 3.5(a) presents the ultrasound B-scan of the aorta. The mean thickness of the wall of the normal aorta measured 0.8 mm and was smaller compared to the plaque laden aorta. The luminal diameter measured from the IVUS image was approximately 4.5 mm. The thin wall of the aorta made it difficult to mechanically rotate and perform the scan and therefore artifacts resulting from irregular motion are evident in the IVUS B-scan at locations 11 o'clock and 5 o'clock. The photoacoustic response was relatively homogeneous from all parts of the tissue in the IVPA image presented in Fig. 3.5(b). The signals indicate the presence of normal fibrous tissue components. The combined image in Fig. 3.5(c) shows the IVPA image overlaid on the IVUS B-scan. The field of view of the images in Fig. 3.5(a-c) is 8.25 mm in diameter. The normal aortic section stained by H&E in Fig. 3.5(d) was characterized by a thin intima composed of an endothelial cell layer with an underlying media composed of elastic fibers and smooth muscle cells. The absence of macrophages is clearly indicated by the RAM-11 stained image in Fig. 3.5(e). The polarization microscopy image of the tissue section stained with Picrosirius red in Fig. 3.5(f) demonstrates the presence of the normal thin collagen of type III.

3.5 DISCUSSION

In this work, we performed ex vivo imaging studies on a rabbit model of atherosclerosis. Photoacoustic images of the artery with plaque and control arteries were obtained using the combined IVUS/IVPA imaging system. The studies were aimed at testing the ability of photoacoustic imaging to detect plaques. Results presented in this chapter underscore the importance of functional imaging of plaques. The structural IVUS image of the plaque vaguely suggested the presence of cholesterol indicated by a degradation of the ultrasound speckles in the vicinity of the tissue layer close to the lumen. There was also a morphological indication of the presence of the plaque with a thickening of the intima (inner most layer of the artery). However, the contrast in the IVUS images was insufficient to ascertain the presence of any additional markers of plaque vulnerability. In contrast, the IVPA image at 532 nm could identify the spatial extent of the plaque and established the presence of lipids and focally dense deposits of collagen. The IVPA response from the aorta of the control rabbit was nearly homogeneous with no plaques. The imaging results were confirmed with histology with reasonable correlation.

3.5.1 Photoacoustic signals from the plaque

The photoacoustic response is a consequence of the wavelength dependent optical absorption characteristics of the heterogeneous tissues and plaque. As is evident from the histology images in Fig. 3.2, the principal plaque components in our animal model of atherosclerosis include lipids, macrophage foam cells, a mixture of thick collagen fibers and stabilizing smooth muscle cells. The magnitude of signals in the IVPA image relies on the wavelength of laser light used for excitation. For example, in Fig. 3.4(b), the laser-induced acoustic response from the lipid filled plaque was generally low in comparison to the signal from the rest of the fibrous tissue. Indeed, the optical absorption coefficient of mammalian fat indicate low absorption (μ_a=0.01 cm^{-1}) at 532 nm [30] while the maximum absorption coefficient (μ_a=0.1 cm^{-1}) occurs at 920 nm [30, 31]. Nevertheless, the low photoacoustic signal regions in our results were useful and provided the contrast to distinguish the plaque from the adjoining tissue. Another component of the vulnerable plaque that has significant implications on the plaque stability is the monocyte derived macrophage cells that could trigger an inflammatory response. We observed a spatial correspondence of the high photoacoustic response with the positive expression of RAM-11 antigen throughout the plaque. Therefore IVPA imaging may have the capability to identify macrophage infiltration in the plaque. However, since the optical properties of macrophage cells are not well documented, additional experiments are required to corroborate this observation. The histology describes the lesion to be predominantly cellular in nature. This stage of plaque development could contain a heterogeneous mixture of macrophage cells invading the plaque and smooth muscle cells laying down collagen that strengthen the fibrous cap. The likelihood of the high photoacoustic signal being contributed by hemoglobin absorption due to blood staining of the lumen wall cannot be completely eliminated.

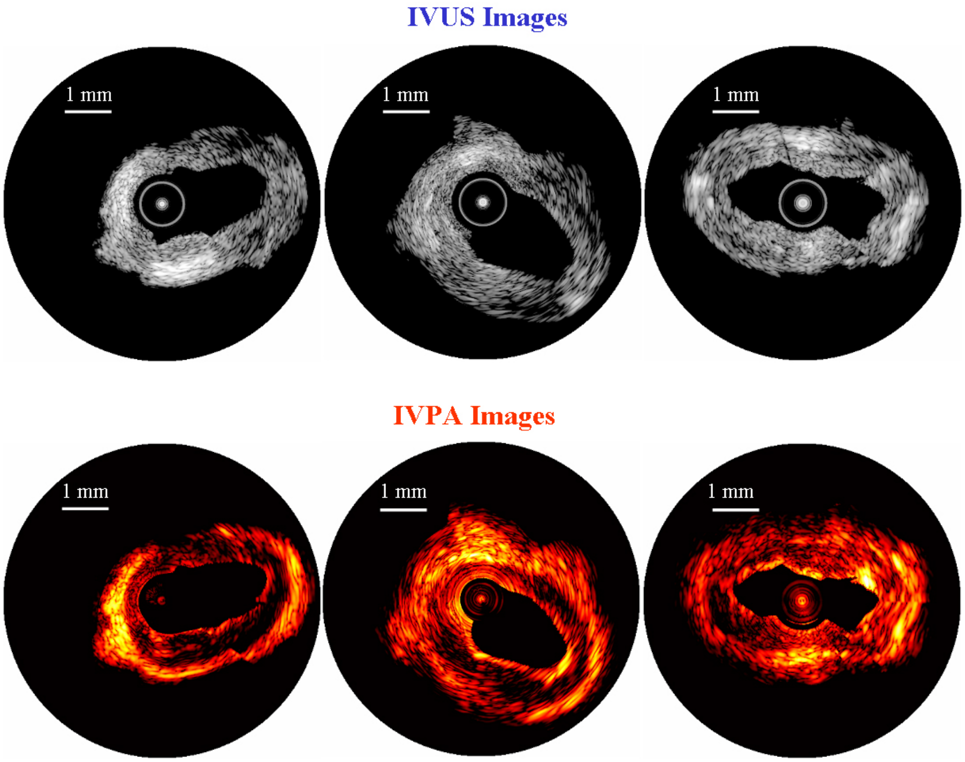

Figure 3.6: Cross-sectional IVUS (top) and IVPA (bottom) images at various sections along the rabbit aorta when the IVUS catheter is close to the tissue. The IVPA images reveal varying amounts of lipid content in the plaque.

The position of the catheter in the lumen of the artery affects the quality of IVPA images. In the IVUS and IVPA scans presented in Fig. 3.6, the catheter is off-center and close to the arterial wall. In such a scenario, the photoacoustic ring-down signals at the surface of the catheter interfere with the IVPA response from the tissue. The artifacts resulting from the transducer ring-down are evident in the IVPA image (center) in Fig. 3.6. These near-field artifacts are accentuated in our images because of the imaging configuration (forward mode) and the elevation of the signals close to the catheter by time gain compensation.

3.5.2 Effect of optical scattering

The photoacoustic signals generated in the tissue is a function of the optical absorption coefficient and the distribution of optical fluence. Generally, for highly scattering tissues the optical energy deposition and the generated photoacoustic response depends on both the absorption and scattering coefficients. Therefore, the contribution of optical scattering coefficient to the overall photoacoustic response needs to be examined. Furthermore, the mismatch in the refractive index at the boundaries (water-tissue and tissue-water) may contribute to high sub-surface fluence. To examine the effects mentioned above, we modeled the light transport in a multi-layered tissue structure using the Monte Carlo modeling approach. The effect of scattering on the absorbed optical fluence is illustrated in Fig. 3.7. Specifically, an increase in scattering will contribute to an increase in the optical fluence absorbed by the arterial tissue. Furthermore, the results also indicate the presence of sub-surface fluence at the boundary facing the laser irradiation. At the boundary further away from the incident laser beam, the effect of an increase in sub-surface fluence is negligible and does not contribute to the increased photoacoustic response.

The above analysis confirms the increase in IVPA response in the arterial tissue as a result of high scattering structures (Figs. 3.4, 3.5 and 3.6). However, the lack of contribution from sub-surface fluence in the lumen-artery boundary may indicate the generation of the photoacoustic response due to absorption (e.g. inflammatory neo-intimal micro blood vessels).

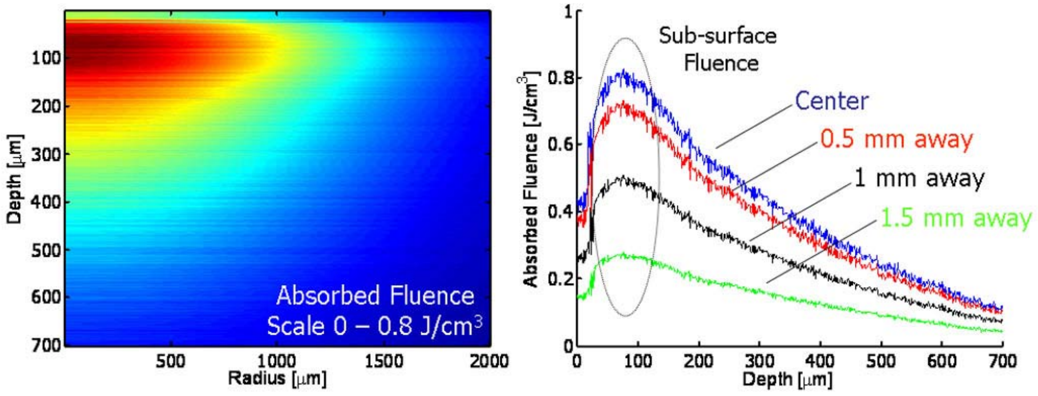

Model Parameters

Gaussian Laser Pulse Radius=2 mm
Laser Energy = 30 mJ
Laser Wavelength = 532 nm

532 nm	μa	μs	g	Size (μm)
Adventitia	13	283	0.79	200
Media	5	418	0.91	400
Intima	10	250	0.84	100

Layers

Adventitia, Media and Intima layers of the arterial tissue with water as the surrounding medium.

Refractive Index – water = 1.335
tissue = 1.5

Figure 3.7: Monte Carlo model of light distribution in a layered arterial tissue. The sub-surface fluence accumulated in the boundary due to a mis-match in the refractive index (between water and tissue) and the scattering dominated arterial tissue.

3.5.3 Collagen in IVPA images

The extracellular matrix of the arterial wall is mainly comprised of fibronectin, elastin, collagen, proteoglycans and water. Collagen constitutes up to 60% of the total plaque proteins and is responsible for plaque stability, growth and stenosis. The amount of collagen can also influence macrophage functions [32], SMC proliferation [33] and migration [34] and could stimulate thrombus formation [35]. Therefore, it is important to investigate the capability of IVPA imaging to detect collagen. A consistent observation in both the control aorta and the fibrous plaque containing different structural forms of collagen is the relatively higher magnitude of photoacoustic response. In the visible and near infrared spectral region, the aorta is dominated by scattering. The absorption values suggested by researchers vary and are generally 10-100 times greater than lipids and decrease with the increase in wavelength [36-39]. At the wavelength of 532 nm used in our experiments, signal contribution from water is minimal. However, water could be the only major absorber present in the fibrous region. The normal aorta shows nearly homogeneous photoacoustic response. Similar observation is noted in the healthy tissue matrix of the lesion infested vessel containing collagen as well as other fibrous components of the plaque. For example, the presence of bright pixels in both the IVPA and IVUS images most often indicates fibrous tissue. The location of the bright signals in circumferential regions close to the lumen also correlates well with the fibrous cap containing thick collagen fibers (yellow-red in Picrosirius red stained image). These high magnitude signals could be a result of absorption by micro-vessels containing blood and the highly scattering collagen fibers. Additional studies are required to determine the contribution of collagen to the overall photoacoustic signal from a fibrous region.

3.5.4 Importance of the IVUS image

In addition to portraying the overall morphology of the arterial tissue, the IVUS image also helps in determining the useful signals in an IVPA image. For example, in Fig. 3.8, the scan converted IVPA image shown in the top panel reveals photoacoustic response from areas outside the arterial wall. There could be several reasons for this observation. First, the presence of any strong optical absorber (e.g. residual blood stain) may result in a temporal ring-down of the photoacoustic response. Second, fibrous tissue overlying the outer surface of the vessel could produce photoacoustic response. The light in our imaging configuration was incident from outside the tissue; hence, photoacoustic signals from these extra-arterial structures could not be avoided. Third, there were instances in our imaging studies when the optical energy on the transducer surface produced ultrasound pulses. These ultrasound echoes from structures close to the transducer could produce signals and corrupt the photoacoustic response.

Therefore, in the absence of a well-defined structure in the IVPA image, the IVUS image was utilized as a structural reference. The bottom panel in Fig. 3.8 further illustrates the image where, the photoacoustic response was corrected for the exponential decrease in light distribution. The signal compensation curve was applied within the boundaries of the arterial wall demarcated by the IVUS image.

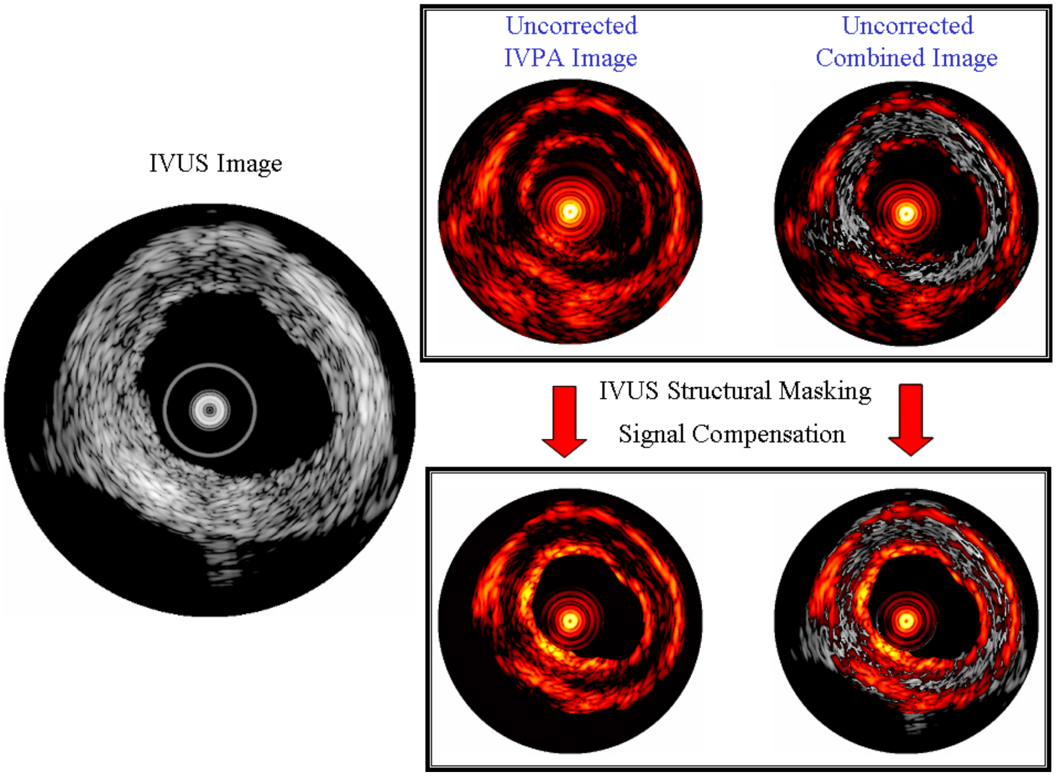

Figure 3.8: An example illustrating the importance of the IVUS image in identifying the structural boundaries in the IVPA image. The boundaries were further utilized for applying signal compensation to account for the exponential decease in optical energy. The corrected images are shown in the bottom panel.

3.5.5 Effect of luminal blood

The *ex vivo* experiments were performed in saline to eliminate the absorption effects of blood at the laser excitation wavelength of 532 nm. Indeed, the absorption of light by blood would decrease the laser energy incident on the aorta. The effect of light attenuation could be minimized if the laser illumination is performed in the optical diagnostic window of 680 nm – 800 nm. To test and illustrate the effect of blood on the photoacoustic imaging, we performed studies on a dissected carotid artery with plaque at a laser excitation wavelength of 700 nm. The images shown in Fig. 3.9 are the ultrasound B-scan image and photoacoustic scans of the artery compared in the presence of saline and blood. The ultrasound echo (Figs. 3.9(a) and 3.9(c)) and photoacoustic response (Figs. 3.9(b) and 3.9(d)) were detected using a single element, focused, 4 mm aperture, 5.8 mm focal length 48 MHz ultrasound probe. The images indicate that plaque could be reliably detected in the presence of blood. The magnitude of the photoacoustic response from the tissue in the presence of blood shown in Fig. 3.9(d) was lesser than the response in the presence of saline in Fig. 3.9(b). Indeed, the attenuation of light through blood leads to a decrease in the laser energy incident on the artery. However, the depth dependent correction of the photoacoustic response in the artery to compensate for the light attenuation by blood resulted in an image similar to that obtained in saline. The ability to obtain photoacoustic response and detect the plaque using a 700 nm laser illumination in the presence of blood (Fig. 3.9(d)) suggests that clinical implementation of intravascular photoacoustic imaging is possible.

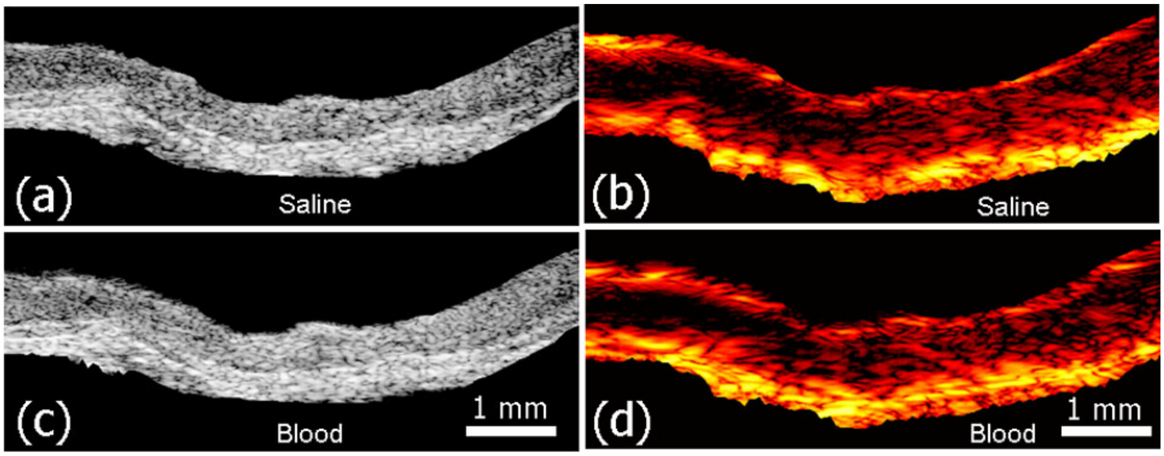

Figure 3.9: Ultrasound and photoacoustic image of the carotid artery with plaque immersed in (a-b) saline, (c-d) blood. The images were obtained at the same cross-section and measure 6.4 mm by 2.1 mm.

3.6 SUMMARY

This chapter details the ex vivo photoacoustic imaging studies to detect plaques. We performed combined IVUS and IVPA imaging studies on ex vivo samples of the atherosclerotic aorta using an IVUS imaging catheter. The photoacoustic response from the lesion supplemented with the IVUS image and histopathological analysis indicates the ability of IVPA imaging to detect plaques. The IVPA image obtained with a 532-nm pulsed laser illumination clearly delineated a concentric region containing lipid and invading foam cells. Furthermore, the lesion showed a region of high photoacoustic signal from the tissue-lumen boundary. These bright signals indicate the ability of IVPA imaging to detect the fibrous cap with thick collagen fibers. Finally, the photoacoustic scan of the plaque at 700 nm in the presence of clinically relevant environment (forward mode configuration in the presence of blood) suggests that in vivo implementation of IVPA imaging is possible.

3.7 REFERENCES

[1] A. G. Bell, "On the production and reproduction of sound by light," *Am. J. Sci.*, vol. 20, pp. 305-324, 1880.

[2] A. A. Oraevsky and A. A. Karabutov, "Optoacoustic Tomography," in *Biomedical Photonics Handbook*, T. Vo-Dinh, Ed.: CRC Press, 2003, pp. 34-1 - 34-34.

[3] X. Wang, Y. Pang, G. Ku, X. Xie, G. Stoica, and L. V. Wang, "Noninvasive laser-induced photoacoustic tomography for structural and functional in vivo imaging of the brain," *Nat Biotechnol*, vol. 21, pp. 803-6, 2003.

[4] S. Y. Emelianov, S. R. Aglyamov, J. Shah, S. Sethuraman, W. G. Scott, R. Schmitt, M. Motamedi, A. Karpiouk, and A. Oraevsky, "Combined ultrasound, optoacoustic and elasticity imaging," *Proceedings of the 2004 SPIE Photonics West Symposium: Photons Plus Ultrasound: Imaging and Sensing*, vol. 5320, pp. 101-112, 2004.

[5] R. I. Siphanto, K. K. Thumma, R. G. M. Kolkman, T. G. van Leeuwen, d. M. F.F.M., J. W. van Neck, L. N. A. van Adrichem, and W. Steenbergen, "Serial noninvasive photoacoustic imaging of neovascularization in tumor angiogenesis," *Optics Express*, vol. 13, pp. 89-95, 2004.

[6] S. Sethuraman, S. R. Aglyamov, J. H. Amirian, R. W. Smalling, and S. Y. Emelianov, "Intravascular photoacoustic imaging to detect and differentiate atherosclerotic plaques," *Proceedings of the 2005 IEEE International Ultrasonics Symposium*, pp. 133-136, 2005.

[7] J. A. Ambrose, M. A. Tannenbaum, D. Alexopoulos, C. E. Hjemdahl-Monsen, J. Leavy, M. Weiss, S. Borrico, R. Gorlin, and V. Fuster, "Angiographic progression of coronary artery disease and development of myocardial infarction," *J. Am. Col. Cardiol.*, vol. 12, pp. 56-62, 1998.

[8] W. C. Little, M. Constantinescu, R. J. Applegate, M. A. Kutcher, M. T. Burrows, F. R. Kahl, and W. P. Santamore, "Can coronary angiography predict the site of a subsequent myocardial infarction in patients with mild-to-moderate coronary artery disease?," *Circulation*, vol. 78, pp. 1157-66, 1988.

[9] M. Naghavi, P. Libby, E. Falk, S. W. Casscells, S. Litovsky, J. Rumberger, J. J. Badimon, C. Stefanadis, P. Moreno, G. Pasterkamp, Z. Fayad, P. H. Stone, S. Waxman, P. Raggi, M. Madjid, A. Zarrabi, A. Burke, C. Yuan, P. J. Fitzgerald, D. S. Siscovick, C. L. de Korte, M. Aikawa, K. E. Juhani Airaksinen, G. Assmann, C. R. Becker, J. H. Chesebro, A. Farb, Z. S. Galis, C. Jackson, I. K. Jang, W. Koenig, R. A. Lodder, K. March, J. Demirovic, M. Navab, S. G. Priori, M. D. Rekhter, R. Bahr, S. M. Grundy, R. Mehran, A. Colombo, E. Boerwinkle, C. Ballantyne, W. Insull, Jr., R. S. Schwartz, R. Vogel, P. W. Serruys, G. K.

Hansson, D. P. Faxon, S. Kaul, H. Drexler, P. Greenland, J. E. Muller, R. Virmani, P. M. Ridker, D. P. Zipes, P. K. Shah, and J. T. Willerson, "From vulnerable plaque to vulnerable patient: a call for new definitions and risk assessment strategies: Part I," *Circulation*, vol. 108, pp. 1664-72, 2003.

[10] R. Virmani, F. D. Kolodgie, A. P. Burke, A. Farb, and S. M. Schwartz, "Lessons from sudden coronary death: a comprehensive morphological classification scheme for atherosclerotic lesions," *Arterioscler Thromb Vasc Biol*, vol. 20, pp. 1262-75, 2000.

[11] R. Ross, "The pathogenesis of atherosclerosis: a perspective for the 1990's," *Nature*, vol. 362, pp. 801-809, 1993.

[12] R. Ross, "Atherosclerosis--an inflammatory disease," *N Engl J Med*, vol. 340, pp. 115-26, 1999.

[13] E. Falk, P. K. Shah, and V. Fuster, "Coronary plaque disruption," *Circulation*, vol. 92, pp. 657-71, 1995.

[14] P. Libby, P. M. Ridker, and A. Maseri, "Inflammation and atherosclerosis," *Circulation*, vol. 105, pp. 1135-43, 2002.

[15] P. R. Moreno, E. Falk, I. F. Palacios, J. B. Newell, V. Fuster, and J. T. Fallon, "Macrophage infiltration in acute coronary syndromes. Implications for plaque rupture," *Circulation*, vol. 90, pp. 775-8, 1994.

[16] P. Libby and R. Ross, "Cytokines and growth regulatory molecules," in *Atherosclerosis and coronary artery disease*, vol. 1, V. Fuster, R. Ross, and E. J. Topol, Eds. Philadelphia: Lippincott-Raven, 1996, pp. 585-94.

[17] E. W. Raines, M. E. Rosenfeld, and R. Ross, "The role of macrophages," in *Atherosclerosis and coronary artery disease*, vol. 1, V. Fuster, R. Ross, and E. J. Topol, Eds. Philadelphia: Lippincott-Raven, 1996, pp. 539-55.

[18] P. K. Shah, "Mechanisms of plaque vulnerability and rupture," *J Am Coll Cardiol*, vol. 41, pp. 15S-22S, 2003.

[19] M. D. Rekhter, "Collagen synthesis in atherosclerosis: too much and not enough," *Cardiovasc Res*, vol. 41, pp. 376-84, 1999.

[20] Z. A. Fayad and V. Fuster, "Clinical imaging of the high-risk or vulnerable atherosclerotic plaque," *Circ Res*, vol. 89, pp. 305-16, 2001.

[21] S. Sethuraman, S. R. Aglyamov, J. H. Amirian, R. W. Smalling, and S. Y. Emelianov, "Intravascular Photoacoustic Imaging Using an IVUS Imaging

Catheter," *IEEE Transactions on Ultrasonics Ferroelectrics, and Frequency Control*, vol. 54, pp. 978-986, 2007.

[22] S. Sethuraman, S. R. Aglyamov, J. H. Amirian, R. W. Smalling, and S. Y. Emelianov, "Development of a combined intravascular ultrasound and photoacoustic imaging system," *Proceedings of the 2006 SPIE Photonics West Symposium: Photons Plus Ultrasound: Imaging and Sensing*, vol. 6086, pp. F1-F10, 2006.

[23] M. Overturf and D. Loose-Mitchell, "In vivo model system: the choice of experimental model for analysis of lipoproteins and atherosclerosis," *Curr. Opin. Lipidology*, vol. 3, pp. 179-185, 1992.

[24] M. E. Rosenfeld, A. Chait, E. L. Bierman, W. King, P. Goodwin, C. E. Walden, and R. Ross, "Lipid composition of aorta of Watanabe heritable hyperlipemic and comparably hypercholesterolemic fat-fed rabbits. Plasma lipid composition determines aortic lipid composition of hypercholesterolemic rabbits," *Arteriosclerosis*, vol. 8, pp. 338-47, 1988.

[25] S. J. Daley, E. Herderick, J. F. Cornhill, and K. A. Rogers, "Cholesterol-fed and casein-fed rabbit models of atherosclerosis. Part 1: Differing lesion area of volume despite equal plasma cholesterol levels," *Arteroscler. Thromb.*, vol. 14, pp. 95-104, 1994.

[26] J. R. Guyton and K. F. Klemp, "Early extracellular lipid deposits in aorta of cholesterol-fed rabbits," *Am. J. Pathol.*, vol. 141, pp. 925-936, 1992.

[27] S. J. Daley, E. Herderick, J. F. Cornhill, and K. A. Rogers, "Cholesterol-fed and casein-fed rabbit models of atherosclerosis. Part 2: Differing lesion area of volume despite equal plasma cholesterol levels," *Arteroscler. Thromb.*, vol. 14, pp. 105-114, 1994.

[28] J. B. Atkinson, R. L. Hoover, K. K. Berry, and L. L. Swift, "Cholesterol-fed heterozygous watanabe heritable hyperlipidemic rabbit: A new model for Atherosclerosis," *Atherosclerosis*, vol. 78, pp. 123-126, 1989.

[29] M. Overturf, H. Sybers, J. Schapers, and H. Taegtmeyer, "Hypertension and atherosclerosis in cholesterol-fed rabbits. Part 1. Mild, two kidney one-clip goldblatt hypertension treated with enlapril," *Atherosclerosis*, vol. 59, pp. 283-299, 1986.

[30] R. L. P. a. S. van Veen, H.J.C.M., A. Pifferi, A. Torricelli, and R. Cubeddu, "Determination of visible near-IR absorption coefficients of mammalian fat using time- and spatially resolved diffuse reflectance and transmission spectroscopy," *Journal of Biomedical Optics*, vol. 10, pp. 0540041-0540046, 2005.

[31] B. J. Tromberg, N. Shah, R. Lanning, A. Cerussi, J. Espinoza, T. Pham, L. Svaasand, and J. Butler, "Non-invasive in vivo characterization of breast tumors using photon migration spectroscopy," *Neoplasia*, vol. 2, pp. 26-40, 2000.

[32] R. B. Wesley, 2nd, X. Meng, D. Godin, and Z. S. Galis, "Extracellular matrix modulates macrophage functions characteristic to atheroma: collagen type I enhances acquisition of resident macrophage traits by human peripheral blood monocytes in vitro," *Arterioscler Thromb Vasc Biol*, vol. 18, pp. 432-40, 1998.

[33] H. Koyama, E. W. Raines, K. E. Bornfeldt, J. M. Roberts, and R. Ross, "Fibrillar collagen inhibits arterial smooth muscle proliferation through regulation of Cdk2 inhibitors," *Cell*, vol. 87, pp. 1069-78, 1996.

[34] E. F. Rocnik, B. M. Chan, and J. G. Pickering, "Evidence for a role of collagen synthesis in arterial smooth muscle cell migration," *J Clin Invest*, vol. 101, pp. 1889-98, 1998.

[35] H. E. Roald, T. Lyberg, H. Dedichen, M. Hamers, P. Kierulf, A. B. Westvik, and K. S. Sakariassen, "Collagen-induced thrombus formation in flowing nonanticoagulated human blood from habitual smokers and nonsmoking patients with severe peripheral atherosclerotic disease," *Arterioscler Thromb Vasc Biol*, vol. 15, pp. 128-32, 1995.

[36] M. J. C. van Gemert, R. Verdaasdonk, E. G. Stassen, G. A. Schets, G. H. Gijsbers, and J. J. Bonnier, "Optical properties of human blood vessel wall and plaque," *Lasers Surg Med*, vol. 5, pp. 235-237, 1985.

[37] W. Cheong, S. A. Prahl, and A. J. Welch, "A review of optical properties of biological tissue," *IEEE J. Quantum Electronics*, vol. 26, pp. 2166-2183, 1990.

[38] A. A. Oraevsky, S. L. Jacques, and F. K. Tittel, "Measurement of tissue optical properties by time-resolved detection of laser-induced transient stress," *Appl. Opt.*, vol. 36, pp. 402-415, 1997.

[39] M. J. C. van Gemert, A. J. Welch, S. L. Jacques, Q. F. Cheong, and W. M. Star, "Light distribution, optical properties, and cardiovascular tissues," in *Lasers in cardiovascular medicine and surgery: Fundamentals and techniques*, G. S. Abela, Ed. Norwell, MA: Kluwer Academic Publishers, 1990.

Chapter 4: Spectroscopic Intravascular Photoacoustic Imaging

4.1 ABSTRACT

The potential of intravascular photoacoustic (IVPA) imaging to detect atherosclerosis was previously demonstrated using a 532 nm nanosecond pulsed laser and an intravascular ultrasound (IVUS) catheter. However, the composition of plaques is needed to differentiate vulnerable plaques. Therefore, we introduce a multi-wavelength photoacoustic imaging method to distinguish various types of plaques. Spectroscopic IVPA imaging was performed on ex vivo samples of a rabbit aorta (normal and plaque) at several wavelengths within 680-900 nm range. The spectral variation of photoacoustic response was extracted and a spectroscopic analysis was performed. The results of our preliminary study suggest that the spectroscopic intravascular photoacoustic imaging technique can be used to differentiate fibrous and lipid components of the plaque.

4.2 INTRODUCTION

The vulnerability of an atherosclerotic plaque to rupture causing acute coronary syndromes is primarily dependent on the plaque composition. The major contribution to a vulnerable plaque is extracellular lipid accumulation. However, the inflammatory response to atherosclerosis is often responsible for the development of several other types of vulnerable plaques with varied composition [1, 2]. The complex biochemical pathways following hypercholesterolemic conditions could potentially determine the fate of an atherosclerotic lesion (calcification, collagen synthesis or degradation, blood thrombus, endothelial degradation). For example, the internalization of modified lipoproteins by macrophage cells and subsequent release of matrix metalloproteinase (MMP) lead to a degradation of collagen and other connective tissue matrix proteins [1]. In addition, the choice of appropriate therapy also requires the knowledge of plaque composition. The current challenges in the studies of plaque regression are to identify, and preferably quantify, changes in response to treatment. Therefore, there is a need for an imaging technique in interventional laboratories to detect and differentiate atherosclerosis.

Biomedical optoacoustic (also referred as photoacoustic) imaging is a technique relying on the contrast generated by the optical absorption property of the tissues [3, 4]. The imaging technique involves the detection of photoacoustic signals generated in response to absorption of pulsed laser illumination. In our earlier work [5, 6], we demonstrated photoacoustic imaging for intravascular imaging applications. Such a technique, in conjunction with intravascular ultrasound has immense potential in interventional applications, specifically, vulnerable plaque detection [7]. The basis for the differentiation of a heterogeneous lesion using photoacoustic imaging is the difference in the optical absorption coefficients of common plaque components (lipid, water, blood, and collagen) in the aortic tissue [8].

In this chapter, we investigate the potential of multi-wavelength IVPA imaging to differentiate atherosclerosis. Specifically, a rabbit model of atherosclerosis was utilized for this *ex vivo* study. The laser excitation wavelength range of 680 nm – 900 nm was chosen since the optical absorption coefficient of fat shows a characteristic increase in this range [9, 10]. In addition, this wavelength range is appropriate for in vivo implementation of IVPA imaging where luminal blood absorption is minimized. The wavelength dependent variation of the photoacoustic signal magnitude could possibly encode the spectral information specific to a constituent of the plaque. A simple, derivative-based spectroscopic analysis of the variation of the time-resolved IVPA signals was employed to test the multi-wavelength photoacoustic imaging approach. The spectroscopic IVPA images of the atherosclerotic aorta are presented and compared with images obtained from the control aortic tissue samples. The preliminary results indicate the potential of IVPA imaging to detect the lipid and fibrous components of the vulnerable plaque.

4.3 MATERIALS AND METHODS

The photoacoustic imaging studies were performed on a section of a plaque-rich aorta obtained from a rabbit subjected to a 0.15% cholesterol diet for 10 months. The low cholesterol dietary regimen was utilized to induce fibro-cellular lesions comprised of inflammatory macrophage cells, lipids and deposits of thick collagen type I. The excised tissue was stored in saline for no more than 4 hours prior to the imaging experiments. The control sample for the imaging studies was obtained from a rabbit subjected to a normal diet for the same period of time.

The prototype of the intravascular photoacoustic (IVPA) imaging system designed for the *ex vivo* studies was described in detail previously [5, 6]. Briefly, a tunable ($\lambda = 680$ nm – 900 nm) Nd:YAG pumped optical parametric oscillator (OPO) pulsed laser source (Vibrant B, Opotek, Inc.) provided the optical illumination for photoacoustic imaging. The collimated laser beam was directed to the tissue sample from the outside using an optical system containing a prism and lens. The optically induced acoustic response generated through a temporal thermal confinement of laser energy was detected using a coronary IVUS imaging catheter (40 MHz, 2.5 French, Atlantis™ SR Plus, Boston Scientific, Inc). Initially, the optical beam and photoacoustic sensing element were somewhat aligned to obtain the maximum photoacoustic signal from the aorta. Subsequently, the intravascular ultrasound (IVUS) and photoacoustic (IVPA) scans were performed by incrementally rotating the sample. A complete rotation of the sample containing 250 photoacoustic beams was obtained to image an entire cross-section of the aorta. Each photoacoustic A-line signal (or beam) was digitized at a sampling rate of 200 MHz. The IVPA scanning was repeated for multiple laser wavelengths (680, 700, 720, 740, 760, 780, 800, 850 and 900 nm). The location of the imaging plane was noted and the imaged cross-section was sliced for histological examination. The cross-sections were stained using Hematoxylin and Eosin (structural information of plaque deposition), RAM-11 (macrophage cells) and Picrosirius red (collagen). The histology images obtained from these staining methods were examined under a microscope and digitized for correlation with the IVPA images.

The photoacoustic response in the polar system of coordinates (angle and depth) was corrected for the depth dependent attenuation of optical energy using an exponential time gain compensation curve. We assumed an exponential decrease in the optical fluence governed by the effective optical attenuation coefficient. The exponential compensation factor with a coefficient of 20.5893 cm^{-1} was utilized based on the absorption and reduced scattering coefficient reported for an advanced fibrous atheroma [8]. Further, the images were normalized to compensate for the wavelength dependence of the laser source energy. To obtain the change in the energy with wavelength of the laser source, we utilized the magnitude of the photoacoustic signal generated on the surface of the IVUS imaging catheter and is plotted in Fig. 4.1. After applying a digital band pass filter (25 MHz – 45 MHz), the images were scan converted to the cartesian system of coordinates and visualized using the same display dynamic range of 45 dB. To analyze the spectral variation in the absorption of the various plaque and tissue constituents, a simple method utilizing linear approximation of wavelength dependence of the optical absorption was employed. The first derivative was computed using the finite difference approach

$$\left(\frac{ds}{d\lambda}\right)_i \approx \frac{s(\lambda_i) - s(\lambda_j)}{\lambda_i - \lambda_j}, \tag{4.1}$$

where s is the magnitude of the photoacoustic response, λ_i is the wavelength at which the derivative is computed and λ_j is the reference wavelength. The finite approximation was used to obtain a coarse estimation of the first derivative between two discrete wavelengths. For detailed analysis of the multi-wavelength photoacoustic response in the regions of interest (ROI) demarcated by histology, the relative energy (integral or area under the curve) of the photoacoustic response was calculated. A 1D trapezoidal numerical integration was evaluated for the envelope of the IVPA response in each of the 20 beams (28.8^0 azimuthal) covering a depth of 30 samples (225 μm radial). These values of the relative energy were estimated for multiple wavelengths within 680 nm – 900 nm range.

Finally, the IVPA imaging and spectroscopic analysis were repeated for the control aorta that contained no obvious plaques and compared with the images obtained from the atherosclerotic aorta.

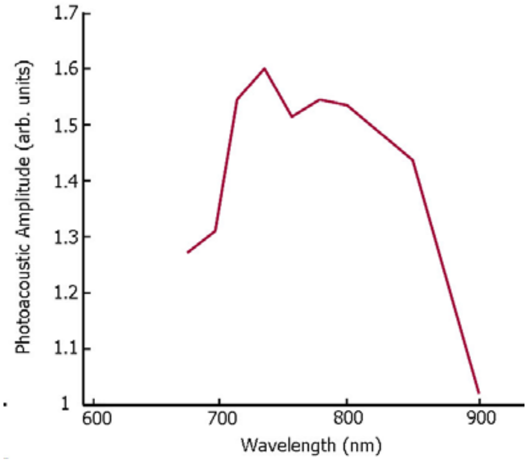

Figure 4.1: Variation of the laser energy with wavelength estimated from the amplitude of the photoacoustic response on the transducer.

4.4 RESULTS

The IVPA images obtained at multiple wavelengths between 680 nm and 900 nm are presented in Fig. 4.2(a). The cross-sectional images of the aorta indicate a significant thickening of the wall as a result of the plaque deposition. All images are shown using the same display range and a field of view of 6.75 mm diameter. A characteristic feature in the IVPA images is the change in the amplitude of the photoacoustic signal at different wavelengths. For example, the region in the image at 2 o'clock shows minimum photoacoustic response at 680 nm with progressive increase in the signal magnitude towards 900 nm. The histology of the cross section of the aorta is presented in Fig. 4.2(b-d). The H&E, RAM11 and Picrosirius red stained images show significant plaque formation with intimal thickening leading to 20% stenosis, presence of macrophage foam cells in a lipid pool and fibrous deposits of collagen (type I and III). There is good correlation between histology and IVPA images.

The IVPA images of the control aorta covering a field of view of 6 mm in diameter are presented in Fig. 4.3. In comparison to the images of the atherosclerotic aorta, the normal aorta shows a thin wall with nearly homogeneous photoacoustic response. Further, the difference in the magnitude of the photoacoustic signal at various wavelengths of laser excitation is minimal. The histology images (H&E, RAM11 and Picrosirius red) confirm the absence of plaques and the presence of thin fibrous collagen type III.

(a)

(b) (c) (d)

Figure 4.2: Multi-wavelength intravascular photoacoustic (IVPA) imaging of a plaque-laden aorta. (a) IVPA images obtained at multiple excitation wavelengths in the 680 – 900 nm range with a field of view of 6.75 mm in diameter and photomicrograph of the histology sections stained with (b) H&E, (c) RAM-11 and (d) Picrosirius red.

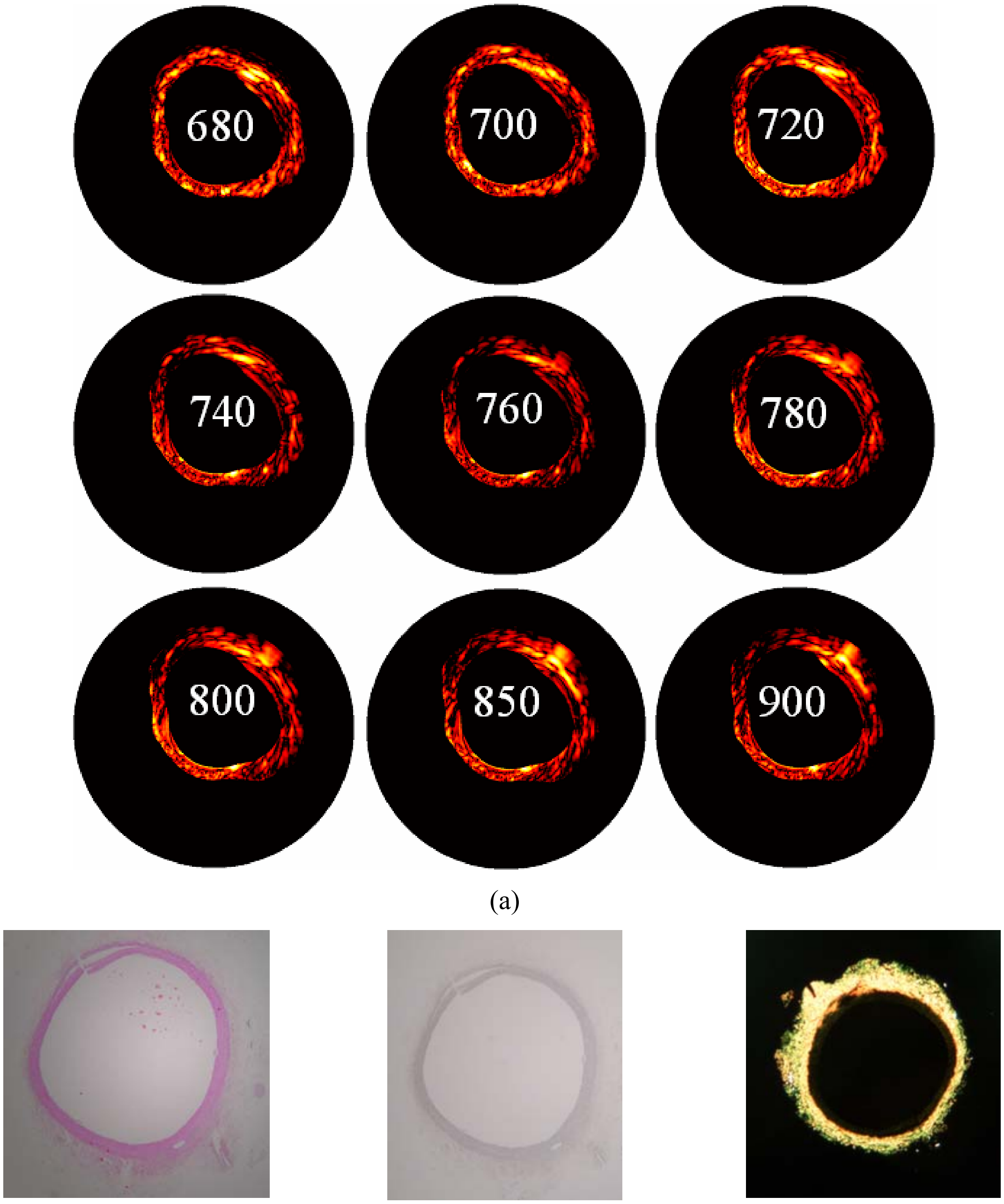

(a)

(b) (c) (d)

Figure 4.3: Multi-wavelength intravascular photoacoustic (IVPA) imaging of the normal aorta. (a) IVPA images at multiple laser wavelengths in the 680- 900 nm range with a field of view of 6 mm in diameter and photomicrograph of the histology sections stained with (b) H&E, (c) RAM-11 and (d) Picrosirius red

Figure 4.4 presents the spectroscopic IVPA images of the atherosclerotic and normal aorta computed using the finite differences approach at λ_i = 900 nm and λ_j = 680 nm. The map of the plaque-rich aorta is fairly heterogeneous with positive and negative values of the first derivative. For example, three regions with distinctly different slopes are indicated by the arrows in Fig. 4.4(a). The region 1 contains positive slope due to an increase in the absorption of light with increase in the optical wavelength. The region 3 with negative slope indicates a decrease in optical absorption coefficient while the region 2 with negative slope and values close to zero suggests no significant change in optical absorption. Compared to the atherosclerotic vessel, the spectroscopic image of the control aorta in Fig. 4.4(b) is nearly homogeneous with regions largely containing slope values close to zero.

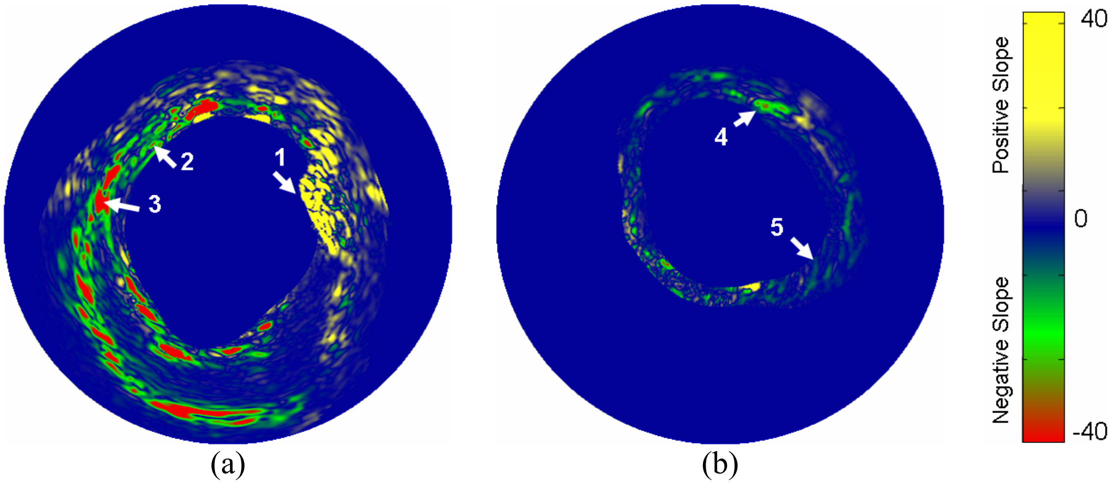

Figure 4.4: The spectroscopic (first derivative) IVPA images of (a) the atherosclerotic (field of view: 6.75 mm diameter) and (b) control aorta (field of view: 6 mm diameter) calculated at 900 nm using a finite differences approach. The reference image for evaluating the first derivative was obtained at 680 nm.

Furthermore, the energy of the photoacoustic response in several representative regions of atherosclerotic vessel and normal aorta was analyzed (Fig. 4.5). Clearly, there are significant spatial and spectral variations in the energy of the photoacoustic signal within the plaque-rich vessel. The spatially-averaged relative photoacoustic energy in the regions 1 and 3 in Fig. 4.5(a) correspond to areas with positive and negative slope respectively. Further, the energy of the photoacoustic signal in region 2 in Fig. 4.5(a) show minimal variation and is characteristically similar to the values obtained in the regions 4 and 5 in Fig. 4.5(b).

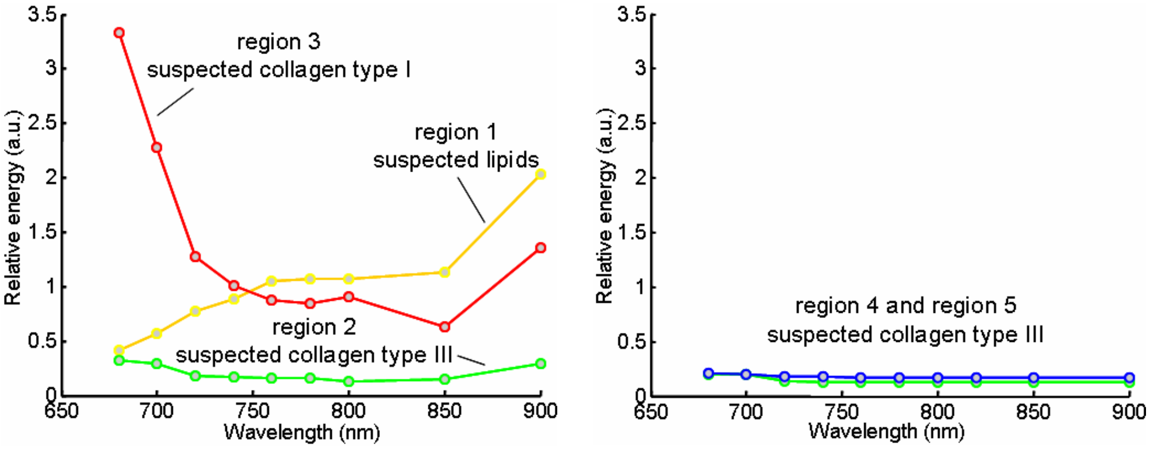

(a) (b)

Figure 4.5: Variation in the relative energy of the photoacoustic response with wavelength observed in (a) atherosclerotic and (b) control aorta. The energy values were calculated from the regions marked 1, 2, 3, 4 and 5 in Fig. (4.4).

4.5 DISCUSSION AND CONCLUSIONS

Intravascular photoacoustic images of atherosclerotic aorta (Fig. 4.2) indicate the presence of plaques and are clearly different from the IVPA images of normal aorta (Fig. 4.3) although the composition of the plaque is not easily discernable from the photoacoustic images. However, the spectroscopic IVPA images (Fig. 4.4) and the variation of the energy of the photoacoustic response (Fig. 4.5) identified the constituents of the plaque and tissue as evident from the histological slices of the tissue.

Notable in the spectroscopic photoacoustic images is the presence of regions with different slopes indicating an increase or decrease in the absorption with wavelength. The optical absorption coefficient of lipids increases towards 900 nm [9, 10]. Therefore, to target the detection of lipids which is the major constituent of vulnerable plaques, we specifically chose to evaluate the spectroscopic behavior of the photoacoustic signal near 900 nm where the differences in slopes are largest. Our observation of positive slope values in the spectroscopic IVPA images and the presence of lipids in the histology suggests that the intravascular photoacoustic spectroscopy could possibly detect fat deposits in the plaque. Further, the regions of negative slope in the spectroscopic IVPA images correlate with the thickened fibrous deposits of collagen type I. This structural change in the collagen is an important indicator that determines the stability of a plaque. The rest of the plaque and the normal aorta contain thin fibrillar structures of collagen type III and the spectroscopic IVPA images in these regions show a negligible change in the slope (Fig. 4.5). The role of collagen in the photoacoustic signal generation in the 680 nm – 900 nm wavelength range is not yet clear as the fibrous proteins are highly scattering with a peak absorption in the ultraviolet range of the spectrum [11]. However, there is a possibility of a heterogeneous mixture of water, collagen and elastin producing photoacoustic signals of a relatively low magnitude and negligible change with wavelength. The thickening of the collagen and an absence of smooth muscle cells in the plaque during inflammation could possibly vary the optical properties of the lesion. The wavelength dependence of the relative energy obtained by the integral of the photoacoustic signal corroborates the observation in the first derivative images.

In this chapter, the photoacoustic response of the lipid and fibrous collagen-rich components of the vulnerable atherosclerotic lesion was investigated. The multi-wavelength IVPA imaging technique could be useful in monitoring the response of the lesion to lipid lowering therapy as well as the staging of atherosclerosis. Furthermore, IVPA imaging utilizing the variation in the optical absorption of hemoglobin may play a major role in the detection of thrombus.

In conclusion, we obtained multi-wavelength intravascular photoacoustic images of the excised sample of an aortic tissue with plaques. The wavelength dependent change in the optical absorption resulted in the variation in photoacoustic response from the diseased atherosclerotic aorta. The difference in the slopes of this variation of photoacoustic response generated the contrast to differentiate and identify the lipid and collagen in the plaque. These initial investigations using spectroscopic IVPA imaging of plaques suggest the possibility to simultaneously image and differentiate plaques.

4.6 REFERENCES

[1] R. Ross, "Atherosclerosis--an inflammatory disease," *N. Engl. J. Med.*, vol. **340**, pp. 115-26, 1999.

[2] P. Libby, P. M. Ridker, and A. Maseri, "Inflammation and atherosclerosis," *Circulation*, vol. **105**, pp. 1135-43, 2002.

[3] A. A. Oraevsky and A. A. Karabutov, "Optoacoustic Tomography," in *Biomedical Photonics Handbook*, T. Vo-Dinh, Ed.: CRC Press, 2003, pp. 34-1 - 34-34.

[4] P. C. Beard and T. N. Mills, "Characterization of post mortem arterial tissue using time-resolved photoacoustic spectroscopy at 436, 461 and 532 nm," *Phys Med Biol*, vol. **42**, pp. 177-98, 1997.

[5] S. Sethuraman, S. R. Aglyamov, J. H. Amirian, R. W. Smalling, and S. Y. Emelianov, "Intravascular Photoacoustic Imaging Using an IVUS Imaging Catheter," *IEEE Transactions on Ultrasonics Ferroelectrics, and Frequency Control*, vol. 54, pp. 978-986, 2007.

[6] S. Sethuraman, S. R. Aglyamov, J. H. Amirian, R. W. Smalling, and S. Y. Emelianov, "Development of a combined intravascular ultrasound and photoacoustic imaging system," in *Photons Plus Ultrasound: Imaging and Sensing 2006: The Seventh Conference on Biomedical Thermoacoustics, Optoacoustics, and Acousto-optics*, vol. 6086, A. A. Oraevsky and L. V. Wang, Eds., 2006, pp. F1-F10.

[7] S. Sethuraman, S. Mallidi, S. R. Aglyamov, J. H. Amirian, S. Litovsky, R. W. Smalling, and S. Y. Emelianov, "Intravascular photoacoustic imaging of atherosclerotic plaques: ex vivo study using a rabbit model of atherosclerosis," in *Photons Plus Ultrasound: Imaging and Sensing 2007: The Eighth Conference on Biomedical Thermoacoustics, Optoacoustics and Acousto-Optics*, vol. 6437, A. A. Oraevsky and L. V. Wang, Eds., 2007, pp. 6437291-6437299.

[8] S. A. Prahl, "Optical Properties Spectra compiled by Scott Prahl," Oregon Medical Laser Center, 2001.

[9] B. J. Tromberg, N. Shah, R. Lanning, A. Cerussi, J. Espinoza, T. Pham, L. Svaasand, and J. Butler, "Non-invasive in vivo characterization of breast tumors using photon migration spectroscopy," *Neoplasia*, vol. **2**, pp. 26-40, 2000.

[10] R. L. P. van Veen, H. J. C. M. Sterenborg, A. Pifferi, A. Torricelli, and R. Cubeddu, "Determination of visible near-IR absorption coefficients of mammalian fat using time- and spatially resolved diffuse reflectance and transmission spectroscopy," *Journal of Biomedical Optics*, vol. **10**, pp. 0540041-0540046, 2005.

[11] A. Vogel and V. Venugopalan, "Mechanisms of pulsed laser ablation of biological tissues," *Chem Rev*, vol. **103**, pp. 577-644, 2003.

Chapter 5: Temperature Estimation in Intravascular Photoacoustic Imaging

5.1 ABSTRACT

Intravascular photoacoustic (IVPA) imaging involves the detection of laser-induced acoustic waves generated from the arterial tissue under appropriate conditions of optical excitation. Generally, the laser radiant fluence levels during photoacoustic imaging are kept low (20 mJ/cm^2) to conform to general standards for safe use of lasers on biological tissues. However, laser safety standards in intravascular photoacoustic imaging are not yet fully established. Consequently, monitoring spatio-temporal temperature changes associated with laser-tissue interaction is important to address and confirm thermal safety during IVPA imaging. In this study we utilize the IVUS echo strains to estimate the laser induced temperature increase. Temporal changes in temperature were estimated on a poly(vinyl alcohol) based vessel phantom and an excised sample of an arterial tissue using a cross correlation based time delay estimator and compared at different laser fluence levels. For arterial tissues, temperature elevation of 1.1°C was observed for a laser fluence of 60 mJ/cm^2 and lesser than 1^{o}C for lower energy levels normally associated with IVPA imaging.

5.2 INTRODUCTION

Photoacoustic or optoacoustic effect [1] is a result of an opto-thermal process where, under laser irradiation conditions of thermal and stress confinement, the absorption of light produces acoustic waves. The acoustic transients detected using an ultrasonic detector are used to form photoacoustic images depicting the spatial distribution of optical absorbers [2-5]. Photoacoustic imaging can be performed using an intravascular ultrasound (IVUS) imaging catheter and has the potential to image the composition and functional properties of the arterial wall [6]. The imaging technique was shown to be applicable for intraluminal imaging [7]. Further, the synergistic combination of intravascular photoacoustic (IVPA) imaging with IVUS is expected to play an important role in detecting and differentiating vulnerable atherosclerotic plaques [7, 8]. Indeed, the difference in the optical absorption coefficient between various components of the heterogeneous plaque (lipids, calcium, macrophages, blood, and collagen) could provide the contrast in IVPA imaging.

In photoacoustic imaging, the tissue is subjected to sub-ablation threshold laser pulses of small, 5-10 ns, time duration. During such a short laser pulse, there is minimal conduction of heat and pressure away from the incident region. Furthermore, the energy fluence of optical irradiation is maintained low to conform to laser safety standards for biological applications [9]. However, the maximum permissible exposure for IVPA imaging is not yet established. Therefore, there is a need to monitor the temporal and spatial distribution of temperature following laser excitation and to investigate any possible clinical concerns regarding thermal safety of IVPA imaging.

The extent of thermal tissue damage is dependent on the characteristics of the laser irradiation that includes magnitude, duration and the spatial incidence of the optical energy. However, the amount of heat deposited depends to a large extent on the optical absorption and scattering properties of the tissue. Typically, light distribution can be modeled using the radiative transport equation, Monte Carlo method, the diffusion approximation or Beer’s law which generally describe an exponential distribution of photons in the tissue [10-16]. Subsequent change in the temperature distribution over time can be explained by thermal diffusion of the absorbed energy and modeled using finite difference or finite element techniques [14]. The distribution of thermal energy and its spatio-temporal variation would be a major determinant of tissue damage. Several optical-thermal models for estimating the temperature increase have been previously suggested and discussed [17]. A commonly used parameter for estimating the thermal damage is the thermal relaxation time - the time required for the peak temperature rise to decrease to 37% of the total rise [18]. Generally, if the laser pulse duration is substantially shorter than the thermal relaxation time (as is the case with photoacoustic imaging), thermal damage to the surrounding tissue is minimized. However, in certain cases high temperatures could cause localized damage even after the thermal relaxation time has elapsed.

Ultrasound has been used as a means to determine temperature changes in biological tissues. Several parameters have been investigated to utilize ultrasound for temperature estimation that include measurement of change in speed of sound [19-21], attenuation coefficient [22-25], ultrasound echo-shift [23, 26-29] and backscatter energy [30]. In this work, we utilize the ultrasound-based strain estimates of temperature change as a method to determine thermal effects during photoacoustic imaging. The increase in temperature of the sample result in a shift in the ultrasound echoes. The apparent shift in the echoes is caused by the change in speed of sound and thermal expansion of the material [31-34]. However, for the relatively low (upto 10°C) temperature increases, the displacements produced by the thermal expansion in the tissue are negligible and the relative shift of the echo signals is primarily determined by the temperature changes in the speed of sound [26, 32]. In IVPA imaging, the pulsed laser excitation is expected to cause a very small increase in the temperature of the sample. The differential displacement or strain observed in the sample is a function of the speed of sound change with temperature, and the thermal change can be monitored using ultrasound. Indeed, using IVUS imaging, the temperature induced strain can be measured and related to the actual temperature increase.

Clinically, the successful implementation of IVPA imaging is dependent on multiple factors [7]. One of the important criteria is the amount of laser fluence required to generate photoacoustic images with acceptable signal to noise ratio. Therefore, it is utmost important to control the laser energy and maximize the photoacoustic signal while maintaining safety standards. While the radiant energy of the laser can be controlled externally, the temperature generated at the site of laser incidence is unknown. The purpose of this study was to establish the safety of IVPA imaging by measuring the temperature increase following laser incidence on arterial tissues. During the imaging of atherosclerosis, IVPA imaging is generally performed along with IVUS imaging to obtain the optical absorption map of the vessel with respect to the structural content of the arterial wall. Therefore the ultrasound based temperature estimation was performed using an IVUS imaging transducer. Initially, phantom studies were carried out to test the ability of the system to obtain temporal variation in laser induced temperature change. The temperature increase in photoacoustic imaging is dependent on the radiant energy incident on a sample. Therefore, the changes in laser-induced temperature over time were compared for different levels of laser fluence. Finally, the two dimensional spatio-temporal estimation of temperature increase was performed on an excised sample of an arterial tissue.

5.3 ULTRASOUND BASED ESTIMATION OF TEMPERATURE

5.3.1 Arterial vessel samples

The method of remotely estimating temperature using intravascular ultrasound was initially tested on vessel phantoms made out of polyvinyl alcohol. Several materials were investigated for the preparation of the phantoms and polyvinyl alcohol (PVA) was chosen since PVA phantoms are resilient and can be stored for a long time [35]. Further, the ultrasonic [36], optical [37], mechanical [38] and thermal [39] properties of polyvinyl alcohol are well characterized and the material is suitable for multi-modal imaging studies. The thermal properties of polyvinyl alcohol are compared with the aorta tissue and presented in Table 5.1. Generally, the composite vascular phantoms in our studies contained an inclusion embedded into an otherwise homogeneous vessel wall. The inclusion was prepared by mixing 8% (by weight) PVA granules in hot water. To elevate optical absorption needed for photoacoustic contrast, 0.08%, 30 μm diameter graphite flakes were added. The graphite flakes also act as acoustic scatterers in ultrasound imaging. The viscous solution was poured into a mold and subjected to 3-4 freeze-thaw cycles (each cycle consisted of freezing for 12 hours and thawing for 12 hours) to produce a 1 mm diameter cylindrical inclusion. The vessel wall was built using 8% PVA solution mixed with 15 μm diameter silica particles acting as optical and ultrasonic scatterers. This solution was subsequently poured into an 8 mm diameter cylindrical mold where a 2 mm diameter rod was placed in the center of the mold to create the lumen, and the solidified inclusion was embedded into the 3 mm thick vessel wall. The composite intravascular arterial phantom underwent 2-3 freeze-thaw cycles necessary to crosslink the background PVA solution. A photograph of the cylindrical phantom is shown in Fig. 5.1(a).

Table 5.1: Thermal properties of aorta and polyvinyl alcohol [39, 40].

	Thermal Conductivity ($Wm^{-1}K^{-1}$)	*Specific Heat ($Jg^{-1}K^{-1}$)*
Aorta Tissue	*0.476*	*3.72*
Polyvinyl Alcohol	*0.2*	*1.6 – 1.67*

In addition, remote temperature measurement studies following IVPA imaging were performed on excised samples of a rabbit artery. The arterial sample was obtained from a rabbit used in an on-going collaborative study approved by the Animal Welfare Committee at The University of Texas Health Science Center at Houston. The tissue samples from a healthy rabbit were stored in saline for 4 hours prior to the experiment. The size of the artery was approximately 5 mm in diameter (Fig. 5.1(b)).

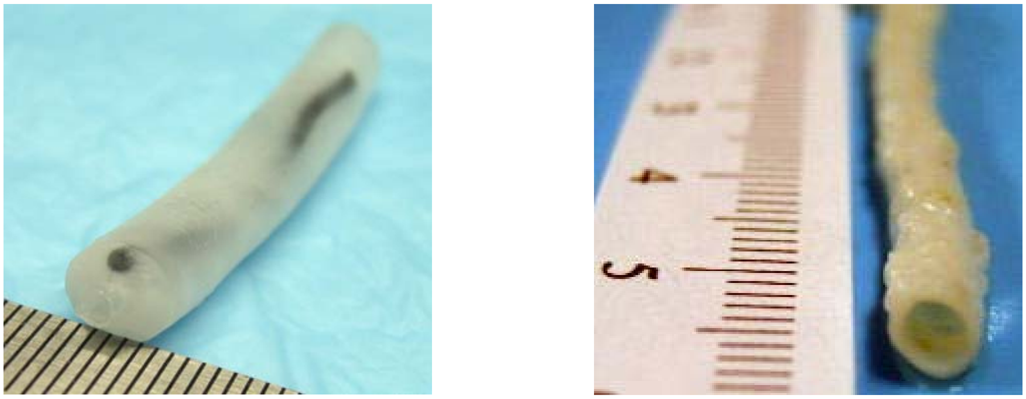

(a) (b)

Figure 5.1: Samples used in the intravascular ultrasound-based temperature monitoring studies. (a) PVA vessel phantom, (b) sample of an excised rabbit artery.

5.3.2 Intravascular imaging system

The block diagram of the experimental setup for temperature estimation during intravascular photoacoustic (IVPA) imaging is illustrated in Fig. 5.2. The vessel phantom or arterial sample was immersed in a water tank for acoustic coupling. A Q-switched pulsed Nd:YAG laser operating at a second harmonic wavelength (λ=532 nm) delivered short laser pulses (up to 27 mJ per pulse) subsequently heating the sample and producing photoacoustic waves. An ultrasonic pulser/receiver was interfaced with the laser and IVUS catheter to receive the IVPA signals and perform IVUS pulse-echo imaging. Both the photoacoustic response and the ultrasound backscattered echoes were detected using a single element, high frequency (40 MHz) intravascular ultrasound imaging catheter (Boston Scientific Atlantis™ SR *PLUS* coronary imaging catheter) inserted in the lumen of the modeled vessel or arterial sample.

In addition to performing IVUS and IVPA imaging, a sequence of ultrasound signals (Fig. 5.3) was captured to obtain the time varying temperature distribution maps. The radiofrequency (RF) signals were acquired using a data acquisition system operating at 200 MHz sampling frequency. A digital pulse generator controlled the acquisition sequence to collect the IVUS and IVPA beams. The trigger signal from the pulse generator was utilized to control the firing of the laser pulse. The same trigger signal after a user specified delay controlled a function generator. The function generator operating in the pulse-burst mode triggered the ultrasonic pulser and initiated multiple pulse-echo IVUS signals (reference and tracking beams) interrogating the same location of the sample. Indeed, the multiple IVUS A-lines are required for measuring the strain and, therefore, for monitoring the temporal changes in the temperature. Once the baseline IVUS signal (reference beam) was captured, the optical pulse for IVPA imaging was generated after 200 μs delay. Then, the sequence of IVUS pulse-echo A-lines (tracking beams) was initiated and captured. The tracking beams were delayed such that the photoacoustic response was obtained between the reference beam and first tracking beam. Therefore, a single acquisition (Fig. 5.3) consisted of the reference IVUS beam, IVPA response and tracking IVUS beams. Since the ultrasonic pulses were generated at 10 kHz pulse repetition frequency (PRF), a temporal resolution of 100 μs was achieved to allow monitoring of rapid changes in temperature.

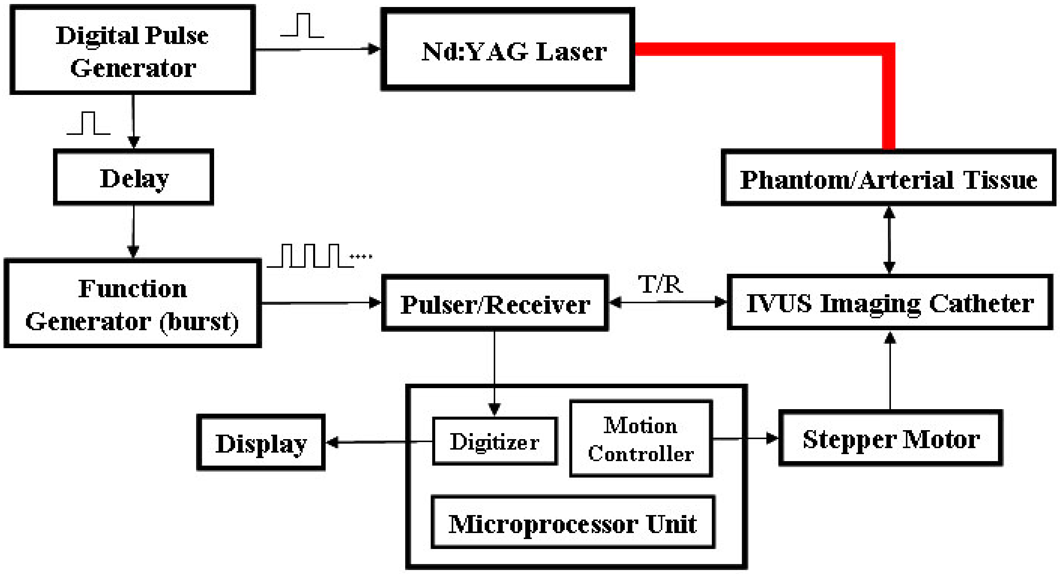

Figure 5.2: Block diagram of the experimental setup for ultrasound-based estimation of temperature during IVPA imaging.

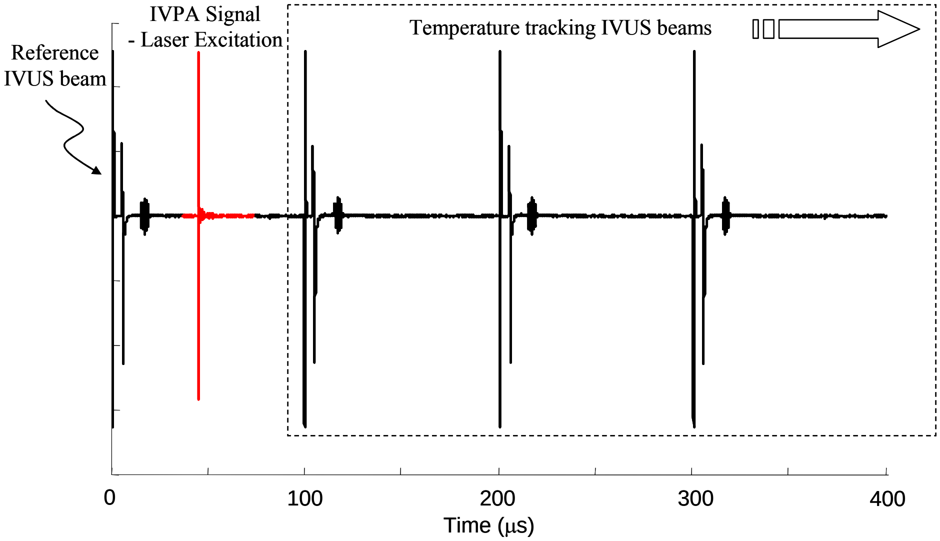

Figure 5.3: Data acquisition sequence illustrating the reference beam, photoacoustic response, and multiple tracking beams. The IVUS tracking beams were obtained at 10 kHz pulse repetition frequency.

5.3.3 Temperature monitoring in the arterial phantom

Laser produced depositions of heat were studied at different (30 mJ/cm^2, 60 mJ/cm^2, and 85 mJ/cm^2) levels of energy fluence. Specifically, temporal behavior of temperature after a laser pulse was monitored along a single radial line intersecting the inclusion. The experiments were performed at the room temperature. Prior to measurements, the transducer in the IVUS imaging catheter was aligned with the laser beam. Then, a single IVUS pulse-echo reference beam was captured. Subsequently, a single laser pulse irradiated the sample, and multiple IVUS beams were acquired immediately following the single laser pulse. Approximately 1000 beams were acquired covering a total time period of 100 ms. The experimental setup was undisturbed and sufficient time was allowed for the temperature to return to the room temperature before repeating the measurements at different energy levels. Thermally induced strain was measured using a 1D cross-correlation based delay estimator [41]. The spatial location producing the maximum strain was used to estimate the highest temperature attained after laser excitation. A high order polynomial fit was used for the calculation of the standard deviation of the measured temperature.

5.3.4 Temperature monitoring in arterial tissue

To estimate the maximum temperature increase in the tissue subjected to laser incidence during IVUS/IVPA imaging, two dimensional temperature monitoring studies were performed using an excised sample of a rabbit artery. Furthermore, we analyzed the spatio-temporal behavior of temperature at the spot of laser incidence on the tissue to confirm thermal safety in IVPA imaging.

The ends of an excised arterial tissue sample were fastened to the rotational assembly and the IVUS imaging catheter inserted into the lumen. The 532 nm wavelength laser beam with 60 mJ/cm^2 laser energy fluence and an approximate beam diameter of 4 mm irradiated a segment of the arterial wall from the outside. The reference IVUS beam, IVPA signal and 300 tracking IVUS beams were acquired at a single azimuthal (or angular) location in the tissue. The IVUS transducer was then rotated incrementally to obtain subsequent A-lines and 250 such acquisitions were performed to image the entire vessel. A time delay of 10 seconds was introduced between acquisitions so that there was no residual temperature when the subsequent measurements were performed.

The reference and tracking IVUS images were formed retrospectively by parsing and re-arranging the captured IVUS reference and temperature tracking beams. In addition, an image of the photoacoustic response was generated from the captured data. For display purpose, the signals were bandpass filtered, envelope detected and scan converted to obtain the IVUS and IVPA images. To estimate the thermally induced displacements and strains in arterial tissue, a two-dimensional cross-correlation technique [41] was implemented in polar system of coordinates using complex basebanded IVUS frames. A hanning-weighted correlation kernel measuring 110 μm radially and 5^o angularly was used to obtain the normalized cross-correlation coefficients. To improve the signal to noise ratio in the displacement estimates, a correlation hanning filter measuring 440 μm by 18^o was applied. Derivatives of the displacement in the radial direction were calculated to obtain the thermal strain images. The strain artifacts occurring in the vicinity of the IVUS catheter due to transducer ring down were filtered using a median filter. Further, a third order polynomial fit was employed in the temporal data to reduce temporal variation of thermal strain. Typically, 300 temperature maps were obtained at 100 μs increments covering a total time period of 30 ms.

5.3.5 Temperature calibration and noise analysis

The shift in the IVUS echoes during IVPA imaging arises from the change in speed of sound and thermal expansion of the material. To quantify the relationship between the externally induced temperature change and the observed thermal induced strain in the PVA phantom and arterial tissue sample, the calibration experiments were needed. Other researchers have previously demonstrated water-bath experiments to generate a calibration curve for liver, muscle, kidney and prostate tissues [23, 42, 43]. We performed similar calibration for polyvinyl alcohol and the arterial tissue. Although for small temperature increases the major contribution to the echo-shifts and apparent strain is the change in the speed of sound, our calibration experiments take into account both the change in speed of sound and negligibly small mechanical strain. The temperature-strain calibration was performed on 5 similar PVA phantoms and 3 sections of an aorta excised from a healthy rabbit. Further, the heating was repeated twice after allowing sufficient time for the temperature to return to the baseline room temperature. The calibration and imaging were performed at the same spatial location in the sample. A single pulse-echo IVUS signal was acquired at the baseline temperature (21°C) to obtain the reference beam. Then, the temperature of the water and, therefore, the sample was steadily increased by an influx of pre-heated water. During the heating process, the true temperature was measured using an external digital thermometer placed close to the IVUS imaging catheter in the lumen of the arterial sample. Simultaneously, IVUS pulse-echo measurements were performed at a constant beam sampling rate of 1 Hz to obtain the tracking beams. The IVUS beam number was synchronized with the elapsed time to match each beam with the associated temperature increase. Finally, cross-correlation based displacement estimation algorithm was used to track the displacements in the IVUS signals and to determine the temperature induced strain as a function of the temperature increase.

Figure 5.4 presents the temperature vs. strain calibration performed on the phantom with an optically absorbing inclusion (Fig. 5.4(a)) and an arterial tissue (Fig. 5.4(b)). Both the phantom and the arterial tissue are primarily water-based and the speed of sound increases with the increase in temperature (up to 50°C). We observed thermal strains of –0.075 and –0.175 percent per degree centigrade in the phantom and the tissue, respectively. For a few degrees in the increase in temperature from the baseline room temperature, the observed thermal strain has a near-linear increase. The rate of heating was constant and slow to make sure that the entire sample underwent a uniform increase in temperature.

Noise in the temperature monitoring system was analyzed by acquiring IVUS signals at a constant room temperature over a 10 second long period of time. During the experiment, the temperature was also independently recorded externally using a high precision (traceable to NIST standards) digital thermometer with an accuracy of ±0.1°C. The analysis of strain variance suggests that the temperature monitoring was unreliable at low thermal strain values of approximately ±0.02% corresponding to temperature values of ±0.3°C.

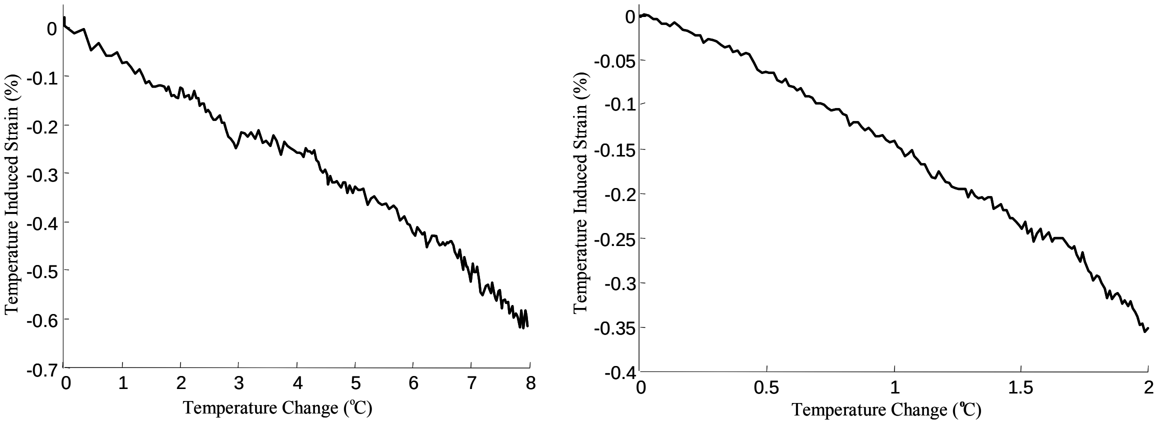

(a) (b)

Figure 5.4: Calibration curves for (a) PVA phantom, and (b) arterial tissue.

5.4 RESULTS

The results of the temperature monitoring in the phantom are presented in Fig. 5.5. The M-mode representation of the temporal variation in temperature monitored along a single radial line passing through the inclusion is shown in Figs. 5.5(a), 5.5(c) and 5.5(e) for laser radiant energies of 30 mJ/cm^2, 60 mJ/cm^2 and 85 mJ/cm^2, respectively. The horizontal axis in these plots represents a total time of 100 ms and the vertical axis is the depth (4 mm) measured from the IVUS transducer element in the catheter. The M-mode images are presented such that the IVUS transducer element is at the top and the laser excitation site is at the bottom since the laser irradiation was applied from the external surface of the phantom. The circular inclusion of graphite particles is approximately centered at a distance 3.75 mm away from the catheter and is close to the outer edge of the vessel phantom. Clearly, the increase in temperature due to light absorption is predominant in the inclusion containing graphite particles, and there is a negligible increase in temperature outside of the inclusion. The maximum temperature and temperature dynamics following a single laser pulse are shown quantitatively in

Figs. 5.5(b), 5.5(d) and 5.5(f). The temperature was measured in the small region within the inclusion located near edge of the inclusion facing the laser irradiation – given the geometry of the phantom, inclusion and laser beam, this region should correspond to the location of maximum temperature increase. The maximum temperatures measured after the laser pulse for radiant energies of 30 mJ/cm^2, 60 mJ/cm^2 and 85 mJ/cm^2 are (0.7±0.3) °C, (2.9±0.2) °C and (5.0±0.2) °C, respectively. The temperature induced in the sample is expected to have a linear dependence on laser fluence. However, the observed deviation could be attributed to the approximate measurement of optical energy. Subsequently, an exponential decrease in temperature due to thermal diffusion was observed. The thermal relaxation time measured by the time required for the temperature to decrease exponentially to 1/e (or 37%) of the maximum value was approximately 5 ms for the above radiant energy conditions. Over time, the temperature does not stabilize at the baseline temperature due to the heat diffusion from the areas adjacent to the imaged A-line.

Spatio-temporal monitoring of temperature was performed in tissue sample. The B-Scan IVUS image of the normal rabbit artery before IVPA imaging, and therefore, before laser deposition of the heat is presented in Fig. 5.6(a). The laser beam irradiated a segment of the arterial wall located between 12 o'clock to 1 o'clock as shown pictorially in Fig. 5.6(a). The IVPA image in Fig. 5.6(b) further outlines the site of laser-tissue interaction. Indeed, the photoacoustic signals occur only in the region illuminated by the laser beam. The temperature distribution following laser irradiation is overlaid on the IVPA response in Fig. 5.6(c) and the spatial extent confirms that the localized temperature increase is limited to a very small region corresponding to the area of high intensity in the laser beam profile. The rest of the tissue exposed to laser irradiation produces photoacoustic signals with negligible increase in temperature.

The temperature maps showing the spatial distribution of temperature in the arterial tissue following IVPA imaging at a laser radiant energy of 60 mJ/cm^2 are presented in Fig. 5.6(d-i). These images were acquired 0.1 ms, 1 ms, 5 ms, 10 ms, 15 ms and 20 ms after pulsed laser excitation. The temperature increase in the 12-1 o'clock region is consistent with the region containing photoacoustic signals in the IVPA image. As expected, the rest of the tissue does not show any increase in the temperature. The maximum temperature increase obtained 0.1 ms after the laser pulse was 1.1°C suggesting negligible temperature rise associated laser-tissue interaction needed for photoacoustic imaging. Subsequently, there is an exponential decrease of temperature due to thermal diffusion and the temperature reaches the baseline at approximately 20 ms following the laser pulse.

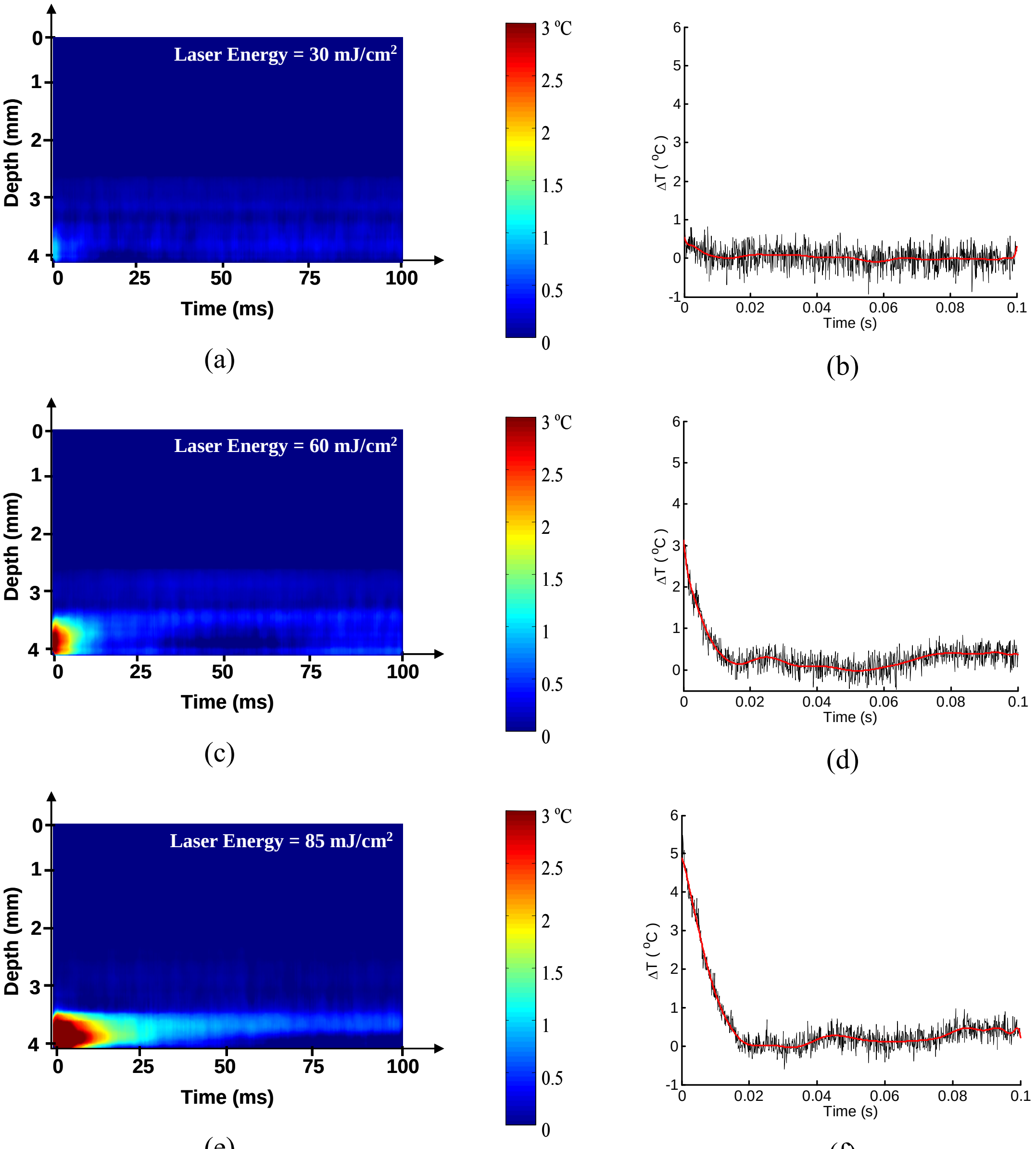

(a)

(b)

(c)

(d)

(e)

(f)

Figure 5.5: Spatio-temporal IVUS estimation of temperature in arterial phantom following laser excitation. The M-mode image representation and the 1-D maximum temperature profile through the inclusion at laser energies (a-b) 30 mJ/cm^2, (c-d) 60 mJ/cm^2, (e-f) 85 mJ/cm^2 monitored for 100 ms following laser excitation shows an exponential decay.

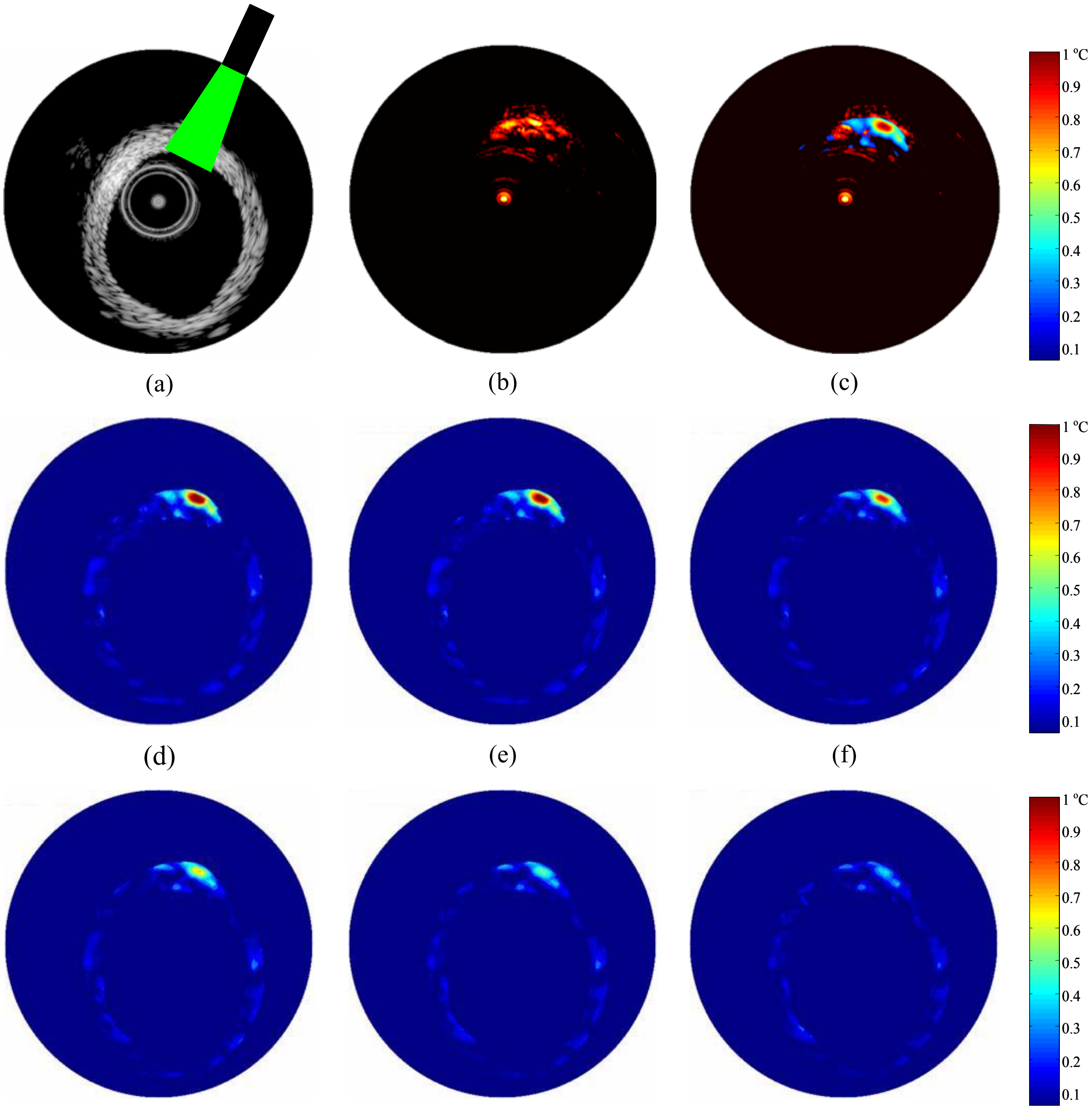

(a) (b) (c)

(d) (e) (f)

(g) (h) (i)

Figure 5.6: (a) IVUS B-Scan image of a normal arterial tissue with the laser illumination in the 12 o'clock to 1 o'clock region, (b) Image of the photoacoustic response from the region of laser incidence, (c) Image displaying the temperature increase immediately following the laser excitation overlaid on the photoacoustic response, (d-i) Temperature maps obtained from the arterial tissue at 0.1, 1, 5, 10, 15 and 20 ms following IVPA imaging. The maximum temperature observed is 1.1°C. The region of the arterial tissue was subject to a laser radiant exposure of 60 mJ/cm^2.

5.5 DISCUSSION

Temperature measurements were performed on sections of a normal artery. The magnitude of the temperature observed in the normal artery is a true worst-case scenario of the temperature increase that will be observed during IVPA imaging. Generally, vulnerable atherosclerotic plaques contain lipids that have lower optical absorption coefficient compared to the normal tissues [44]. Consequently, the presence of the plaque will only lower the maximum temperature in the wall of the arteries. Further, convection effects on the arterial wall due to the flow of luminal blood will mitigate the thermal effects due to laser incidence [45, 46]. Hence, our measurements further suggest the thermal safety of in-vivo IVPA imaging.

5.5.1 Thermal damage analysis

A potential source of damage to the tissues during laser-tissue interaction is the heat generation and subsequent diffusion of heat. Thermal damage, quantified using the Arrhenius damage coefficient analysis, depends on both the maximum temperature attained and the time of exposure [47, 48]. The Arrhenius rate process equation describing unimolecular kinetics can be expressed as

$$\Omega(t) = \ln\left(\frac{C(0)}{C(t)}\right) = A\int_0^t \exp\left(-\frac{E_a}{RT(t)}\right)d\tau \qquad (5.1)$$

where Ω is a dimensionless thermal damage coefficient, C is the concentration of molecules in the native state, t is the exposure time (s), T is the temperature (K), R is the universal gas constant (8.3134 J/mol/K), E_a is the activation energy needed for cell denaturation (J/mole) and A is the frequency factor which is a measure of molecular collisions (s^{-1}). As follows from equation (5.1), the damage coefficient is a function of the ratio of the initial concentration of tissue components to the final concentration after the damage has occurred. A damage coefficient value of 1.0 is the threshold for tissue necrosis with 63% of the tissue undergoing denaturation. The damage analysis was performed for the arterial tissue with the initial temperature distribution taken from the temperature map (Fig. 5.6) at time t =0.1 ms, and the rate process coefficients for arterial tissue ($A = 5.6 \cdot 10^{63}$, $E_a = 430$ KJ/mol) obtained from the literature [49]. The accumulated damage coefficient for the temperature distribution observed after 25 ms is $6.4 \cdot 10^{-11}$ which suggest that the temperature increase and the exposure time is less and does not cause any significant thermal change in the artery tissue following IVPA imaging.

5.5.2 Limitations of the study

A limitation of our technique is the inability to determine temperature change for low radiant energy exposures encountered in IVPA imaging. The strain based temperature estimation has a noise of ±0.3°C and, therefore, cannot be used as an accurate estimation of the temperature changes produced by the low laser energy fluence. A major factor contributing to the noise is the finite signal to noise ratio in the cross-correlation based tracking algorithm for measurements of low magnitude displacements and strains. However, the low energy fluence and therefore the low temperature increase are not expected to cause any thermal degradation of the aorta.

A potential concern is the accumulation of heat with the application of multiple laser pulses at a high repetition rate. Multiple laser pulses could lead to superposition of temperature. In such a scenario, thermal relaxation of the tissue could be several times longer than that for a single pulse [18]. A reason for this effect could be the presence of residual temperature when the next laser pulse is incident on the sample. However, this effect would not be too pronounced in the IVPA imaging of arterial tissue in vivo. First, the radiant energy could be limited to 20 mJ/cm^2, which according to our experiments is sufficient to generate photoacoustic signals within physiologically acceptable levels of thermal buildup. Second, the blood flow in the arteries will increase the rate of thermal diffusion and cause the temperature to decrease faster [46].

A calibration was required only to obtain the exact magnitude of temperature distribution. However, in the clinical setting, this technique can be applied to set a threshold of laser energy levels in the combined IVUS/IVPA imaging. Indeed, in this scenario, it would suffice to use an approximate calibration curve and no other additional calibration will be required.

5.5.3 Modeling temperature distribution at low optical fluence

Although the intensity of the short, 5 ns duration laser pulse incident on the arterial tissue during our photoacoustic imaging experiments was high, the maximum temperature change was on the order of 1°C (Fig. 5.6). Further, the measurements were performed at a laser fluence of 60 mJ/cm^2, which is much higher than the energies needed in IVPA imaging. Thermal measurements were also performed at energy fluence levels of less than 20 mJ/cm^2. However, the temperature change was lower than 0.3^{o}C and our experimental method could not detect low temperature rise.

We utilized an optical-thermal model to predict the temperature distribution in the artery at energy fluence below 20 mJ/cm^2. The block diagram of the model presented in Fig. 5.7 includes a Monte Carlo light distribution component followed by an explicit finite difference solution for heat diffusion. The arterial vessel at the point of laser incidence can be considered as a three-layered heterogeneous slab with semi-infinite boundaries. The semi-infinite boundary assumption is a reasonable approximation when considering the spatial extent of photon distribution. A cartesian co-ordinate system was used to trace the photon packets with the x-y plane being the surface of the vessel facing the lumen. The laser light delivery was assumed to be from inside the lumen through optical fibers. The other parameters of the pulsed laser excitation include an optical wavelength of 532 nm, energy per pulse of 4 mJ and a laser spot size diameter of 4 mm.

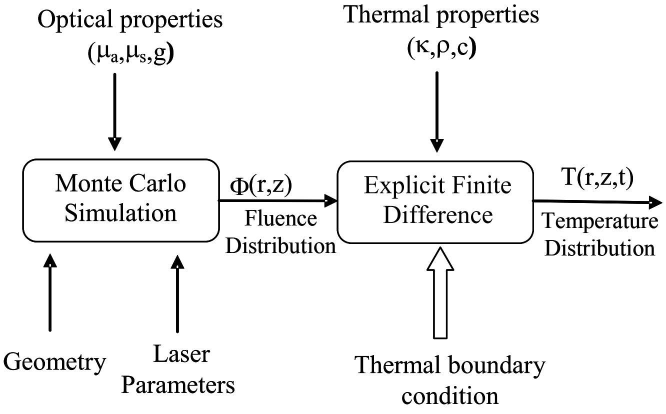

Figure 5.7: Block diagram of the optical-thermal model to obtain the temperature distribution in the artery. The inputs to the model include optical absorption (μ_a), scattering (μ_s) and anisotropy (g) coefficients, laser energy fluence and spot size, density and thermal conductivity of the medium.

The Monte Carlo simulations provide a random walk assessment of the migration of photons at a specific wavelength in an optically heterogeneous absorbing and scattering medium. The simulation used in this model was adapted and performed with the ANSI standard C code (MCML) developed by Wang and Jacques [12, 50, 51]. In the simulations, the size of the grid was 0.0001 cm in the radial and lateral directions. The absorption coefficient, scattering coefficient, and anisotropy factor for the arterial tissue layers were obtained from Keijzer et. al. [52] and are presented in Table 5.2. The absorption per area as a function of depth was normalized by the number of incident photons (1 million) to obtain the probability of the absorption event per unit volume.

Table 5.2: Optical and thermal properties of arterial layers [52, 53]

	Optical Properties			Thermal Properties	
	μ_a [cm^{-1}]	μ_s' [cm^{-1}]	G	ρ [g/cm^3]	C [J/g/K]
Intima	10.04	38.49	0.846	1.09	3.35
Media	5.32	37.44	0.911	1.09	3.35
Adventitia	13.29	59.97	0.988	1.09	3.35

An explicit finite difference technique was utilized to solve the two-dimensional form of the heat conduction equation (equation 5.2), where T is the temperature at time t and (r, z) are the spatial cylindrical coordinates in the radial and azimuthal directions.

$$\frac{\partial T}{\partial t} = \kappa \frac{\partial^2 T}{\partial r^2} + \kappa \frac{\partial^2 T}{\partial z^2} \tag{5.2}$$

Heat conduction by blood and any other adjoining tissue were not considered. For simplicity, an insulating boundary condition was assumed where the boundary and the surrounding medium have the same temperature. The discretized grid and the corresponding steady state temperature distribution obtained from the Monte Carlo simulations serve as the initial condition for the thermal diffusion model.

The temperature distribution maps at a laser fluence of 8 mJ/cm^2 and various time intervals in the intimal layer is shown in Fig. 5.8. In IVPA imaging, the laser incidence would be the highest in the inner most layer of the artery (intima). The steady state temperature elevation observed immediately following the pulsed laser excitation indicate a maximum temperature rise of 0.1 ^{0}C. The magnitude of temperature elevation at 8 mJ/cm^2 suggests and confirms that IVPA imaging is clinically safe.

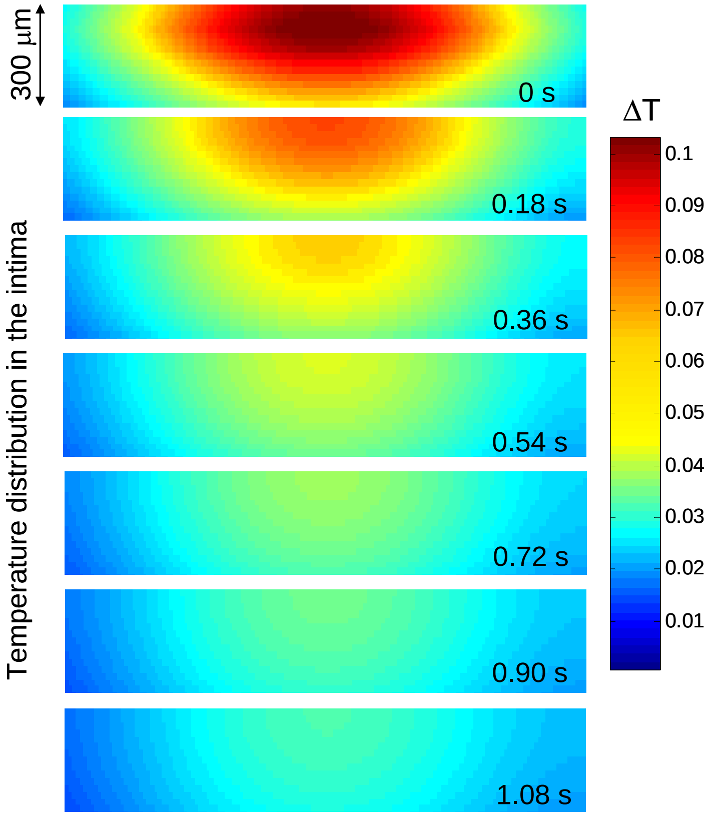

Figure 5.8: The temperature distribution maps obtained using an optical-thermal model. The laser energy fluence of 8 mJ/cm^2 and optical excitation wavelength of 532 nm were chosen for the simulations.

5.5.4 Applications

Although the present study was not focused at continuous and accurate monitoring of temperature *in vivo*, a potential intravascular application would be to differentiate plaque components based on thermal heterogeneity. Indeed, feasibility studies using thermal strain imaging have demonstrated the promise of the technique for intravascular plaque detection [28, 54]. Another application of the developed ultrasound technique is the ability to obtain the optical properties of the tissue while performing combined IVUS/IVPA imaging of the arterial vessel. Indeed, the observed exponential distribution of the thermally induced apparent strain is a function of the optical energy deposition. Therefore, we can utilize the temporal thermal strain distribution to extract the absorption and effective scattering coefficients of tissue components.

5.6 SUMMARY

The results of our study outline the ability of IVUS imaging to measure and monitor temperature during intravascular photoacoustic imaging. Remote temperature monitoring using an ultrasound based approach does not require any additional system and can be performed simultaneously during the IVUS/IVPA imaging of the arterial cross-section. The magnitude of temperature increase observed following laser excitation of arterial tissues indicates that IVPA imaging is thermally safe.

5.7 REFERENCES

[1] A. G. Bell, "art. XXXIV on the production and reproduction of sound by light," *Am. J. Sci.*, vol. 20, pp. 305-324, 1880.

[2] A. A. Oraevsky and A. A. Karabutov, "Optoacoustic Tomography," in *Biomedical Photonics Handbook*, T. Vo-Dinh, Ed.: CRC Press, 2003, pp. 34-1 - 34-34.

[3] S. Y. Emelianov, S. R. Aglyamov, J. Shah, S. Sethuraman, W. G. Scott, R. Schmitt, M. Motamedi, A. Karpiouk, and A. Oraevsky, "Combined ultrasound, optoacoustic and elasticity imaging," *Proceedings of the 2004 SPIE Photonics West Symposium: Photons Plus Ultrasound: Imaging and Sensing*, vol. 5320, pp. 101-112, 2004.

[4] X. Wang, Y. Pang, G. Ku, X. Xie, G. Stoica, and L. V. Wang, "Noninvasive laser-induced photoacoustic tomography for structural and functional in vivo imaging of the brain," *Nat Biotechnol*, vol. 21, pp. 803-6, 2003.

[5] P. C. Beard and T. N. Mills, "Characterization of post mortem arterial tissue using time-resolved photoacoustic spectroscopy at 436, 461 and 532 nm," *Phys Med Biol*, vol. 42, pp. 177-98, 1997.

[6] S. Sethuraman, S. R. Aglyamov, J. H. Amirian, R. W. Smalling, and S. Y. Emelianov, "Intravascular photoacoustic imaging to detect and differentiate

atherosclerotic plaques," *Proceedings of the 2005 IEEE International Ultrasonics Symposium*, pp. 133-136, 2005.

[7] S. Sethuraman, S. R. Aglyamov, J. H. Amirian, R. W. Smalling, and S. Y. Emelianov, "Development of a combined intravascular ultrasound and photoacoustic imaging system," *Proceedings of the 2006 SPIE Photonics West Symposium: Photons Plus Ultrasound: Imaging and Sensing*, vol. 6086, pp. F1-F10, 2006.

[8] S. Sethuraman, S. R. Aglyamov, J. H. Amirian, R. W. Smalling, and S. Y. Emelianov, "Intravascular photoacoustic imaging using an IVUS imaging catheter," *IEEE Trans Ultrasonics Ferroelectrics and Frequency Control*, vol. 54, pp. 978-986, 2007.

[9] ANSI, *American National Standard for Safe Use of Lasers, ANSI Z136.1*. Orlando: Laser Institute of America, 2000.

[10] S. L. Jacques and L. V. Wang, "Monte Carlo modelling of light transport in tissues," in *Optical-Thermal Response of Laser-Irradiated Tissue*, A. J. Welch and M. J. van Gemert, Eds. Newyork: Plenum, 1995, pp. 73-100.

[11] S. A. Prahl, "The diffusion approximation in three dimensions," in *Optical-Thermal Response of Laser-Irradiated Tissue*, A. J. Welch and M. J. van Gemert, Eds. Newyork: Plenum, 1995, pp. 207-231.

[12] M. Keijzer, S. L. Jacques, S. A. Prahl, and A. J. Welch, "Light distributions in artery tissue: Monte Carlo simulations for finite-diameter laser beams," *Lasers Surg Med*, vol. 9, pp. 148-54, 1989.

[13] S. T. Flock, M. S. Patterson, B. C. Wilson, and D. R. Wyman, "Monte Carlo modeling of light propagation in highly scattering tissue--I: Model predictions and comparison with diffusion theory," *IEEE Trans Biomed Eng*, vol. 36, pp. 1162-8, 1989.

[14] J. Roider and B. Birngruber, "Solution of the heat conduction equation," in *Optical-Thermal Response of Laser-Irradiated Tissue*, A. J. Welch and M. J. van Gemert, Eds. New York: Plenum, 1995.

[15] A. Sagi, A. Shitzer, A. Katzir, and S. Akselrod, "Heating of biological tissue by laser irradiation: Theoretical model," *Opt Eng*, vol. 31, pp. 1417-1424, 1992.

[16] B. Anvari, S. Rastegar, and M. Motamedi, "Modeling of intraluminal heating of biological tissue: implications for treatment of benign prostatic hyperplasia," *IEEE Trans Biomed Eng*, vol. 41, pp. 854-64, 1994.

[17] A. J. Welch, "The thermal response of laser irradiated tissue," *IEEE J. Quantum Electronics*, vol. QE-20, pp. 1471-1481, 1984.

[18] B. Choi and A. J. Welch, "Analysis of thermal relaxation during laser irradiation of tissue," *Lasers Surg Med*, vol. 29, pp. 351-9, 2001.

[19] T. Bowen, W. G. Connor, R. L. Nasoni, A. E. Pifer, and R. R. Sholes, "Measurement of the temperature dependence of the velocity of ultrasound in soft tissues," *Ultrasonic Tissue Characterization II*, vol. Spec Publ 525, pp. 57-61, 1979.

[20] B. Rajagopalan, J. F. Greenleaf, P. J. Thomas, S. A. Johnson, and R. C. Bahn, "Variation of acoustic speed with temperature in various excised human tissues studied by ultrasound computerized tomography," *Ultrasonic tissue characterization II*, vol. Spec Publ 525, pp. 227-233, 1979.

[21] R. L. Nasoni and T. Bowen, "Ultrasound speed as a parameter for noninvasive thermometry," *Noninvasive temperature measurement*, pp. 95-107, 1989.

[22] N. L. Bush, I. Rivens, G. R. ter Haar, and J. C. Bamber, "Acoustic properties of lesions generated with an ultrasound therapy system," *Ultrasound Med Biol*, vol. 19, pp. 789-801, 1993.

[23] T. Varghese, J. A. Zagzebski, Q. Chen, U. Techavipoo, G. Frank, C. Johnson, A. Wright, and F. T. Lee, Jr., "Ultrasound monitoring of temperature change during radiofrequency ablation: preliminary in-vivo results," *Ultrasound Med Biol*, vol. 28, pp. 321-9, 2002.

[24] C. A. Damianou, N. T. Sanghvi, F. J. Fry, and R. Maass-Moreno, "Dependence of ultrasonic attenuation and absorption in dog soft tissues on temperature and thermal dose," *J Acoust Soc Am*, vol. 102, pp. 628-34, 1997.

[25] M. Ribault, J. Y. Chapelon, D. Cathignol, and A. Gelet, "Differential attenuation imaging for the characterization of high intensity focused ultrasound lesions," *Ultrason Imaging*, vol. 20, pp. 160-77, 1998.

[26] R. Maass-Moreno and C. A. Damianou, "Noninvasive temperature estimation in tissue via ultrasound echo-shifts. Part 1. Analytical Model," *J Acoust. Soc. Amer.*, vol. 100, pp. 2514-2521, 1996.

[27] R. Seip, P. VanBaren, C. Cain, and E. S. Ebbini, "Noninvasive spatio-temporal temperature change estimation using diagnostic ultrasound," *IEEE Trans Ultrason Ferroelectr Freq Control*, vol. 43, pp. 1068-1078, 1996.

[28] Y. Shi, R. S. Witte, and M. O'Donnell, "Identification of vulnerable atherosclerotic plaque using IVUS-based thermal strain imaging," *IEEE Trans Ultrason Ferroelectr Freq Control*, vol. 52, pp. 844-50, 2005.

[29] M. J. Zohdy, C. Tse, J. Ye, and M. O'Donnell, "Acoustic estimation of thermal distribution in the vicinity of femtosecond laser-induced optical breakdown," *IEEE Trans on Biomedical Engineering*, vol. 53, pp. 2347-2355, 2006.

[30] W. L. Straube and R. M. Arthur, "Theoretical estimation of the temperature dependence of backscattered ultrasonic power for noninvasive thermometry," *Ultrasound Med Biol*, vol. 20, pp. 915-22, 1994.

[31] J. C. Bamber and C. R. Hill, "Ultrasound attenuation and propagation speed in mammalian tissues as a function of temperature," *Ultrasound Med. Biol.*, vol. 5, pp. 149-157, 1979.

[32] R. Seip and E. S. Ebbini, "Noninvasive estimation of tissue temperature response to heating fields using diagnostic ultrasound," *IEEE Trans Biomed Eng*, vol. 42, pp. 828-839, 1995.

[33] Z. Sun and H. Ying, "A multi-gate time-of-flight technique for estimation of temperature distribution in heated tissue: theory and computer simulation," *Ultrasonics*, vol. 37, pp. 107-22, 1999.

[34] C. Simon, P. vanBaren, and E. S. Ebbini, "Two-dimensional temperature estimation using diagnostic ultrasound," *IEEE Trans Ultrason Ferroelectr Freq Control*, vol. 45, pp. 1088-1099, 1998.

[35] C. M. Hassan and N. A. Peppas, "Structure and applications of poly(vinyl alcohol) hydrogels produced by conventional crosslinking or by freezing/thawing methods," *Advances in polymer science*, vol. 153, pp. 37-65, 2000.

[36] K. J. Surry, H. J. Austin, A. Fenster, and T. M. Peters, "Poly(vinyl alcohol) cryogel phantoms for use in ultrasound and MR imaging," *Phys Med Biol*, vol. 49, pp. 5529-46, 2004.

[37] A. Kharine, S. Manohar, R. Seeton, R. G. Kolkman, R. A. Bolt, W. Steenbergen, and F. F. de Mul, "Poly(vinyl alcohol) gels for use as tissue phantoms in photoacoustic mammography," *Phys Med Biol*, vol. 48, pp. 357-70, 2003.

[38] J. Fromageau, E. Brusseau, D. Vray, G. Gimenez, and P. Delachartre, "Characterization of PVA cryogel for intravascular ultrasound elasticity imaging," *IEEE Trans Ultrason Ferroelectr Freq Control*, vol. 50, pp. 1318-24, 2003.

[39] P. R. Sundararajan, "Poly(vinyl alcohol)," in *Polymer data handbook*, J. E. Mark, Ed. New York: Oxford University Press Inc., 1999, pp. 891-892.

[40] J. W. Valvano and B. Chitsabesan, "Thermal conductivity and diffusivity of arterial wall and atherosclerotic plaque," *Lasers Life Sci.*, vol. 1, pp. 219-229, 1987.

[41] M. A. Lubinski, S. Y. Emelianov, and M. O'Donnell, "Cross-correlation speckle tracking techniques for ultrasound elasticity imaging," *IEEE Transactions on Ultrasonics, Ferroelectrics and Frequency Control*, vol. 46, pp. 82-96, 1999.

[42] U. Techavipoo, T. Varghese, J. A. Zagzebski, T. Stiles, and G. Frank, "Temperature dependence of ultrasonic propagation speed and attenuation in canine tissue," *Ultrason Imaging*, vol. 24, pp. 246-60, 2002.

[43] T. Varghese and M. J. Daniels, "Real-time calibration of temperature estimates during radiofrequency ablation," *Ultrason Imaging*, vol. 26, pp. 185-200, 2004.

[44] R. L. P. a. S. van Veen, H.J.C.M., A. Pifferi, A. Torricelli, and R. Cubeddu, "Determination of visible near-IR absorption coefficients of mammalian fat using time- and spatially resolved diffuse reflectance and transmission spectroscopy," *Journal of Biomedical Optics*, vol. 10, pp. 0540041-0540046, 2005.

[45] L. Diamantopoulos, X. Liu, I. De Scheerder, R. Krams, S. Li, J. Van Cleemput, W. Desmet, and P. W. Serruys, "The effect of reduced blood-flow on the coronary wall temperature. Are significant lesions suitable for intravascular thermography?," *Eur Heart J*, vol. 24, pp. 1788-95, 2003.

[46] C. Stefanadis, K. Toutouzas, E. Tsiamis, I. Mitropoulos, C. Tsioufis, I. Kallikazaros, C. Pitsavos, and P. Toutouzas, "Thermal heterogeneity in stable human coronary atherosclerotic plaques is underestimated in vivo: the "cooling effect" of blood flow," *J Am Coll Cardiol*, vol. 41, pp. 403-8, 2003.

[47] J. Pearce and S. Thomsen, "Rate process analysis of thermal damage," in *Optical-thermal response of laser-irradiated tissue*, A. J. Welch and M. J. van Gemert, Eds. New York: Plenum Press, 1995.

[48] F. C. Henriques and A. R. Moritz, "Studies in thermal injury I. The conduction of heat to and through skin and the temperature attained therein. A theroretical and an experimental investigation.," *Am. J. Pathol.*, vol. 23, pp. 531-549, 1947.

[49] R. Agah, J. A. Pearce, A. J. Welch, and M. Motamedi, "Rate process model for arterial tissue thermal damage: implications on vessel photocoagulation," *Lasers Surg Med*, vol. 15, pp. 176-84, 1994.

[50] S. A. Prahl, M. Keijzer, S. L. Jacques, and A. J. Welch, "Monte Carlo model of light propagation in tissue," *SPIE Proceedings of Dosimetry of Laser Radiation in Medicine and Biology*, vol. IS 5, pp. 102-111, 1989.

[51] L. V. Wang and S. L. Jacques, "Monte Carlo modeling of photon transport in multi-layered tissues," *Computer Methods and Programs in Biomedicine*, vol. 47, pp. 131-146, 1995.

[52] M. Keijzer, R. R. Richards-Kortum, S. L. Jacques, and M. S. Feld, "Fluorescence spectroscopy of turbid media: autofluorescence of the human aorta," *Applied Optics*, vol. 28, pp. 4286-4292, 1989.

[53] J. W. Valvano and J. Pearce, "Temperature measurements," in *Optical-thermal response of laser-irradiated tissue*, A. J. Welch and M. J. van Gemert, Eds. New York: Plenum, 1995.

[54] Y. Shi, F. J. deAna, S. Chetcuti, and M. O'Donnell, "Motion artifact reduction for IVUS-based thermal strain imaging," *IEEE Trans Ultrason Ferroelectr Freq Control*, vol. 52, pp. 1312-1319, 2005.

Chapter 6: Conclusions and Future work

6.1 MOTIVATION

Atherosclerosis, the disease of the arteries, continues to be the primary cause of heart disease and stroke. Acute coronary syndromes such as angina pectoris, sudden cardiac death and myocardial infarction are primarily caused by thrombus formation resulting from an instantaneous rupture of a vulnerable coronary plaque. The term vulnerable plaque, has been synonymously used with high-risk plaque, thin-cap fibroatheroma, unstable plaque, and disrupted plaque and refers to a plaque at increased risk of causing thrombosis and lesion progression. Although there are no prospective studies to clearly establish a lesion as vulnerable to rupture, a consensus among researchers suggests certain vital characteristics of a vulnerable plaque.

- Accumulation of large lipid core (>40% of lesion area)
- Degrading fibrous cap overlying the lipid core (60 – 150 μm)
- Recruitment of inflammatory macrophage cells
- Other minor criteria include calcified nodule, endothelial dysfunction, intra-plaque hemorrhage and superficial platelet aggregation.

The high mortality rates in coronary heart disease are attributed to a sudden rupture of the lesion without prior clinical symptoms. Sometimes the first and the only manifestation of the disease could result in death. Several imaging techniques are under investigation to detect and diagnose the high-risk plaques. Owing to the lack of knowledge and evidence of the history of vulnerable plaques and the asymptomatic nature of plaque rupture, the impact of diagnostic imaging techniques in “early detection” of atherosclerosis has been minimal. Although the ultimate goal in diagnostic imaging is to develop non-invasive, inexpensive, real-time and safe techniques, the technical limitations (limited resolution, signal to noise ratio and sensitivity) have impeded their efficacy in imaging coronary vulnerable plaques. Therefore, extensive research on invasive techniques is required to detect, characterize, help therapeutic decision making and monitor the lesion. A successful intravascular plaque imaging technique could benefit existing vascular interventional procedures. Upon review of the major and minor criteria that describe a vulnerable lesion, the important characteristics required in an imaging technique for plaque detection include,

- High resolution to detect a vulnerable cap
- Imaging of inflammatory activity
- Contrast to identify the lipid core
- Capability to identify calcification, morphological changes, vasa-vasorum

A summary of the existing intravascular imaging techniques was presented in Chapter 1. Each of the techniques is aimed at imaging the plaque structure and composition with the overall goal of being able to detect and differentiate vulnerable plaques. However, the imaging techniques do not present comprehensive imaging capability. The myriad vulnerable plaque characteristics necessitate the development of a technique capable of simultaneous assessment of morphological, activity and mechanical information. In the absence of imaging modalities with comprehensive imaging capability, a combination of imaging techniques is required. Therefore, in accordance with our goal of developing a multi-modal intravascular imaging tool, we proposed the combination IVUS and IVPA imaging.

6.2 SUMMARY OF THE RESEARCH

The investigation of the applicability and ability of intravascular photoacoustic imaging to detect and differentiate atherosclerotic plaques was undertaken in a logical sequence.

Initially, we developed a laboratory prototype of the combined IVUS and IVPA imaging system (Chapter 2). The imaging was performed using an IVUS imaging catheter. Indeed, the common detector facilitated the integration. The work in this dissertation mainly involved the initial testing of IVPA imaging. Therefore, the optical excitation for photoacoustic imaging was incident from outside the sample. Such a configuration permitted an easier and efficient method of evaluating IVPA imaging through laboratory studies. The performance of the combined IVUS/IVPA imaging system was evaluated by imaging phantoms. The axial resolution of IVPA imaging was slightly better than IVUS imaging and limited by the narrow frequency band-width of the IVUS imaging transducer. In contrast, the lowering of the center frequency of the photoacoustic response resulted in a poor lateral resolution of IVPA imaging. The IVUS and IVPA images of the polyvinyl alcohol vessel phantom with an embedded inclusion highlighted the advantage of the combination. The optically absorbing inclusion was identified in the IVPA image, while the IVUS image showed the overall structure of the vessel phantom. The excellent contrast between the inclusion and the background displayed in the IVPA image was expected due to the differences in the optical absorption. Nevertheless, the study confirmed that photoacoustic images can be obtained using an IVUS imaging catheter. The artifacts in our images seen as abrupt change in signal magnitude between successive A-lines were mainly contributed by irregular mechanical rotation of the sample. The longitudinal and azimuthal alignment of the catheter with the area of optical incidence was critical to obtaining the photoacoustic signals.

The phantom imaging studies were followed by *ex-vivo* imaging studies on arteries obtained from a rabbit model of atherosclerosis (Chapter 3). The presence of lipids and inflammatory activity are major indicators of plaque vulnerability. Therefore, we utilized aorta tissue samples from rabbits subject to a long-term low cholesterol diet that produced fibro-cellular lesions containing macrophage foam cells, collagen and free lipids. The lipid-filled plaque was detected as low signal (dark) regions in the IVPA image obtained using a 532 nm laser excitation. The control IVPA image indicated a homogeneous photoacoustic response with no obvious presence of plaque. As discussed earlier, the quality and utility of clinical IVPA images will depend on the position of the catheter in the vessel, optical and acoustic beam alignment, optical excitation wavelength, and the influence of optical absorption by blood.

The ex vivo imaging studies were also extended to briefly explore spectroscopic IVPA imaging (Chapter 4). Indeed, photoacoustic imaging in the optical diagnostic window of 680 – 900 nm is essential to, 1) increase optical penetration through blood, 2) differentiate plaques based on the change in magnitude of the photoacoustic signal with wavelength and 3) utilize the high optical absorption of lipids at 920 nm. The first derivative of the spectral variation of magnitude of the IVPA signals displayed in the spectroscopic IVPA image of the plaque aorta suggested the ability to visualize multiple plaque components. In our studies, the spectroscopic IVPA image showed potential in differentiating the lipid from the fibrous regions in the plaque.

Finally, the safety of IVPA imaging was confirmed by an ultrasonic method of temperature measurement. Although the laser radiant exposure in photoacoustic imaging conformed to American National Standards (ANSI), the temperature at the site of opto-thermal response in the arterial tissue was unknown. We utilized the method of ultrasonic thermography, where temperature change was estimated from the apparent temperature induced strain. The low magnitude of temperature change (~1 ^{o}C) at a laser fluence of 60 mJ/cm^2 confirmed safety of IVPA imaging.

6.3 LIMITATIONS

The *ex vivo* studies revealed the potential of IVPA imaging to play a major role in the imaging of plaques. However, the results identified several limitations of this study.

6.3.1 Photoacoustic imaging configuration

Photoacoustic imaging can be performed either in the "forward" or "backward" imaging configurations. In the forward mode, the optical incidence and the imaging transducer are placed on either side of the tissue under investigation. While, in the backward imaging mode, the optical incidence and imaging transducer are on the same side of the tissue. The selection of the method depends on the clinical application. Figure 6.1 illustrates the forward and backward imaging configurations.

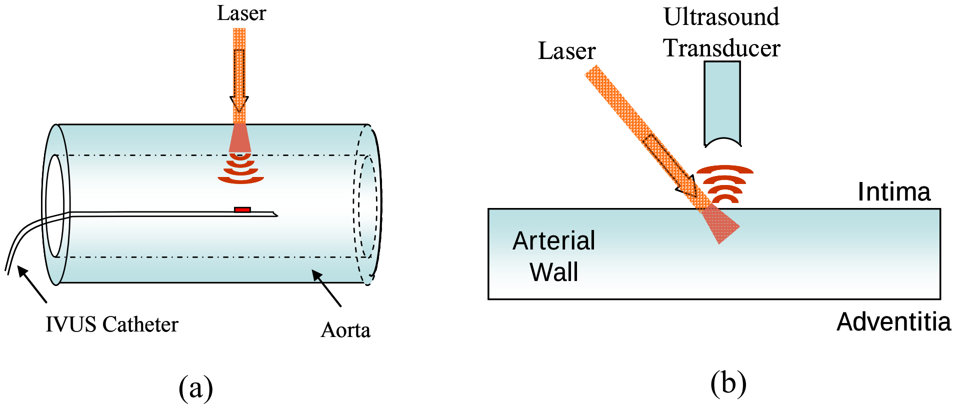

Figure 6.1: Illustration of the (a) forward and (b) backward scanning modes for photoacoustic imaging.

Clinically, in intravascular photoacoustic imaging of plaque, the absence of access to either sides of the artery necessitates the use of the backward imaging configuration. Therefore, the optical illumination and detection of the photoacoustic signals have to be performed inside the arterial lumen. However, in our ex vivo IVPA imaging studies we utilized the forward mode. There are several reasons that led to the choice of the forward mode imaging option. First, to test the feasibility of performing IVPA imaging, a simple system and configuration was acceptable. Second, a quick understanding of the photoacoustic response from the plaque in the laboratory studies was needed before adapting the technique for clinical studies. Therefore, our imaging studies were mainly focused on testing the ability of our technique to only image excised arteries with plaque.

6.3.2 Artifacts in IVPA images

In all our IVPA imaging studies, scanning was performed by mechanically rotating the vessel sample while the transducer and laser beam were approximately aligned. In the absence of a fiber-optic light delivery mechanism required to provide a 360^o illumination, the alternate laboratory method to perform IVPA imaging was by mechanically rotating the sample. Most noticeable artifacts arising from the irregular rotation of the sample were abrupt changes in the magnitude of the photoacoustic signal in adjacent beams. The problem includes an occasional misalignment of the transducer with the optical beam caused by the movement when the vessel wall gets too close to the catheter. Examples of these artifacts are provided and discussed in chapters 3 and 4.

6.3.3 Scanning time

Intravascular photoacoustic imaging using our laboratory prototype is still a slow technique. Currently it takes 30-45 minutes to acquire a single cross-sectional IVUS and IVPA image. For initial evaluation of the technique, the scanning time was acceptable.

However, the slow scan time could become a major limitation for time dependent imaging studies as well as for future clinical implementation. The major contribution to the slow acquisition is the presence of noise in the system. A high frequency noise overlapping the detection frequency was caused by the electromagnetic cross-talk between the high voltage motion control drive and the catheter system. Therefore, it was not possible to apply digital filters to remove the noise. Further, the long catheter also behaves as an antenna and is sensitive to noise from external sources. Effective grounding of electrical contacts minimized the noise. However, the signal to noise ratio (SNR) was still low, affecting the quality of the IVPA images. To improve the SNR at the expense of scanning time, we had to minimize the high current from the motor drive during the acquisition. This was achieved by de-activating the motion control system during the acquisition of IVUS and IVPA signals. Therefore, we introduced a delay of 1-2 s in the acquisition program. Furthermore, averaging of typically 20 records was performed to improve the SNR.

In the absence of the manually induced delay or averaging as described above, the minimum time required to acquire a single cross-sectional IVUS and IVPA image is dependent on the pulse repetition frequency of the laser. The maximum pulse repetition frequency of our Nd:YAG pulsed laser was 20 Hz. For a single-element transducer requiring mechanical rotation for scanning, a single pulse would be needed to obtain 1 IVPA scan line. Therefore, to acquire one complete image consisting of 250 IVPA scan lines, a minimum of 12.5 s is required. Clearly, the scan time can be reduced further by utilizing a multi-element array based IVUS catheter.

6.4 FUTURE DIRECTIONS

6.4.1 Fiber-optic light delivery for IVPA imaging

We can overcome the problems and limitations associated with the current IVPA imaging system with the development of a fiber-optic laser light delivery from inside the lumen of the arterial vessel. A major step in this direction would be to develop a probe where the optical fiber is integrated with the IVUS imaging catheter. An example of the design of an integrated IVUS/IVPA probe is illustrated in Fig. 6.2 using a single element as well as multi-element array based IVUS catheters. There are several factors to be considered before designing and developing the IVPA imaging probe. The factors to be considered are discussed below with an example.

Material and size of the optical fibers. As shown in Fig. 6.2, the IVUS imaging catheter is placed in the center of the probe. Therefore, optical fibers around the outer surface of the IVUS catheter are required for light delivery. The size and number of fibers depend on the diameter of the IVUS catheter. In a hexagonal packing configuration, the total number of fibers (T) in a bundle can be written as a function of the number of concentric layers (n),

$$T = (12 \times n - 5) \tag{6.1}$$

As an example, assuming a hexagonal packing arrangement of the all silica fiber bundle, individual fiber core diameter of 200 μm and outside diameter of 225 μm, then 12 fibers may be arranged in the bundle in the second layer of circular arrangement. The center fiber and first layer of 6 fibers could be removed for the insertion of the IVUS catheter (0.6 mm after stripping the sheath). Apart from the size, the use of an appropriate material and numerical aperture are important criterion in the selection of fibers.

Overall size of the integrated probe. The overall size of the integrated probe must be small enough to be able to image medium sized arteries. In the above example, the probe would include a layer of fiber contributing to a thickness of 0.450 mm, IVUS element of size 0.6 mm, a 0.35 mm guide wire and plastic sheath of thickness 0.2 mm forming a total diameter of 1.8 mm. the size of the optical components (lens) for directing the light could be chosen to match the size of a single fiber.

Light delivery angle. The light delivery angle is an important criterion in the selection of the prisms for the 360^{o} illumination of the artery. The angle of light incident on the artery, the position of the catheter in the arterial lumen, size of the artery investigated and the location of the IVUS element are all inter-dependent factors affecting IVPA imaging of the artery.

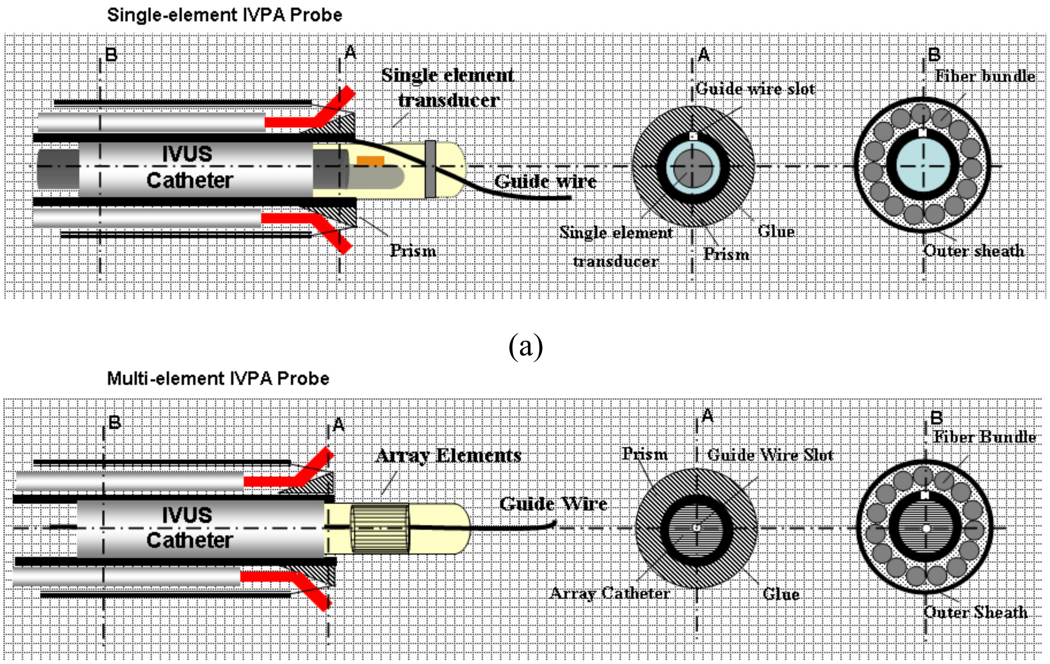

(a)

(b)

Figure 6.2: Illustration of the design of a fiber-optic based integrated IVUS/IVPA probe.

6.4.2 In vivo spectroscopic IVPA imaging

The initial goal of our study was to determine the feasibility of intravascular photoacoustic imaging to identify plaques. Further, we investigated the utility of a multi-wavelength photoacoustic imaging approach to differentiate plaques and identify plaque composition. Imaging studies presented in chapter 4 indicate a definite change in magnitude of the photoacoustic response from the plaque as a function of optical wavelength. The spectroscopic image also suggests the potential to identify lipids, macrophage foam cells and collagen. More studies are required to confirm the findings and also explore the ability to detect and differentiate other types of vulnerable plaques. The development of the fiber optic delivery system would enable clinical evaluation of the technique. Indeed, in clinical studies, luminal blood interference through absorption and attenuation of light is expected. Nevertheless, multi-wavelength IVPA imaging in the optical diagnostic window is expected to produce images with enhanced contrast between various tissue components, decrease in blood absorption and increase in lipid absorption with a maximum absorption at 920 nm.

6.4.3 IVPA imaging of vasa vasorum

Experimental research data suggests a significant role of vasa vasorum in the initiation and progression of different types of vascular disease [1-4]. An extensive network of micro-vessel is associated with acute and chronic inflammation in atherosclerotic plaques. These blood vessels serve to perfuse the arterial plaque in regions away from the blood lumen. Vasa vasorum may also facilitate the entry of macrophages into the lesion causing intra-plaque hemorrhage [5]. The appearance of new micro-vessels is increased in ruptured plaques in the human aorta [6]. One of the markers of plaque vulnerability is an abundance of neovascularization in the intima. Studies have also been reported on the increased vasa vasorum neovascularization in the adventitial layer before the development of vascular lesions [7-9]. Therefore, imaging the micro-vessels may provide an early indication of plaque development. IVPA imaging may play a vital role in imaging the proliferative neovasculature. Indeed, these vessels rich in blood could absorb light and produce a distinct photoacoustic signature. A major task in IVPA imaging is to decrease luminal blood absorption. This could be a deterrent for the imaging of vasa vasorum. In such a case, IVPA imaging with flushing of blood and optical excitation in the wavelength 400 – 500 nm range may simultaneously increase light penetration through luminal blood and increase absorption in the neo-intimal vessels.

6.4.4 Molecular IVPA imaging

In addition to the direct imaging of the pathology, a molecular imaging approach through selective targeting of molecular and cellular markers of plaque inflammation and angiogenesis may improve the detection of atherosclerosis. Selective cell targeting can be achieved by using light absorbing nanoparticles [10, 11]. Indeed, antibody coated gold nanoparticles that selectively target the vascular molecular receptors in the plaque could be a potential contrast agent for IVPA imaging. These molecular receptors may be involved in the pathological evolution of the plaque as well as through other processes that accompany plaque progression (e.g. vasa vasorum). The gold nanoparticles attached to a modified form of the biocompatible polymer poly(ethylene glycol) (PEG) may be useful as a contrast agent for IVPA molecular imaging. Potential sites for targeting with nanoparticles that may improve imaging of atherosclerosis are discussed below.

Neo-vascularization may promote intra-plaque hemorrhage (IPH) and subsequent plaque growth. The development of IPH is an indication of plaque vulnerability [12]. There is a suggestion of the over-expression of vascular cell adhesion molecule VCAM-1 by these vessels in the human atheroma [5]. VCAM-1 has been shown to mediate the adhesion of monocytes and T cells onto the endothelium. Studies have also suggested an active expression and role of VCAM-1 in the recruitment of inflammatory cells around the intimal and adventitial vasa vasorum [13]. Therefore, the selective targeting of VCAM-1 by functionalized gold nanoparticles could help in detecting the neo-vessels in the intima and the adventitia.

Proteins such as $\alpha_v\beta_3$ integrins specifically localize within the vasa vasorum and the plaque microvessels [14]. Therefore these are potential imaging agents for identifying atherosclerotic vessels with abundance of neovasculature. Several $\alpha_v\beta_3$ agents have been developed for ultrasound, PET, SPECT and MRI imaging of atherosclerosis [15-18].

Inflammation in atherosclerosis is accompanied by the recruitment of macrophages. Targeting of macrophages with RAM11 conjugated with gold nanoparticles may be useful. A class of enzymes belonging to the family of matrix metallo-proteinases (MMPs) is responsible for the degradation of collagen and elastin. The MMPs are released during the inflammatory reaction to invading macrophages in the plaque. Imaging of the MMP activity may also offer a method to detect the inflamed lesions.

6.4.5 Thermal imaging using combined IVUS/IVPA imaging

In our work presented in Chapter 5, temperature was estimated during IVPA imaging of the arterial tissue. The method was based on the principle of change in speed of sound with temperature [19]. Indeed, the change in temperature was manifested as temperature induced strain. We were able to measure the unknown laser-induced temperature by a time-delay estimation of the ultrasound echoes. The method can also be employed to utilize the difference in temperature dependence of speed of sound between fat and water based tissues. While the speed of sound in water increases with an increase in temperature, the opposite effect is seen in fat [20]. Therefore, an application of the

IVUS based temperature measurement during IVPA imaging would be to differentiate fat-filled plaque from the normal water based tissue. An indication of the contrast produced by this method of thermal strain imaging has been shown in the preliminary work on detecting thermal change using microwave excitation [21, 22].

6.5 CONCLUSIONS

Intravascular photoacoustic (IVPA) imaging is a new catheter based approach to arterial vascular wall imaging. The technique is based on the detection of acoustic waves generated by absorption of sub-ablation threshold nanosecond laser pulses. The IVPA images provide information based on optical absorption thereby interrogating the functional state of the tissue. The combined IVUS/IVPA imaging provides the necessary structural and functional imaging to detect and differentiate atherosclerotic plaques.

The photoacoustic response from the atherosclerotic aorta at 532 nm of optical excitation indicated the ability of IVPA imaging to detect the lipid content in the plaque. Further, the spectroscopic IVPA imaging performed at multiple wavelengths was useful in differentiating the fibrous and fibro-cellular atherosclerotic plaques. Further studies are required to confirm the ability of IVPA imaging to detect vulnerable plaques. The development of a fiber-optic based combined IVUS/IVPA imaging probe will enable in vivo evaluation of the technique. In addition, the combined imaging has potential applications in the molecular imaging of atherosclerosis.

6.6 REFERENCES

[1] T. P. Crotty, "The role of vasa vasorum in atherosclerosis," *Med Hypotheses*, vol. 28, pp. 233-43, 1989.

[2] A. C. Barger, R. Beeuwkes, 3rd, L. L. Lainey, and K. J. Silverman, "Hypothesis: vasa vasorum and neovascularization of human coronary arteries. A possible role in the pathophysiology of atherosclerosis," *N Engl J Med*, vol. 310, pp. 175-7, 1984.

[3] A. H. Cragg, S. Einzig, J. A. Rysavy, W. R. Castaneda-Zuniga, B. Borgwardt, and K. Amplatz, "The vasa vasorum and angioplasty," *Radiology*, vol. 148, pp. 75-80, 1983.

[4] S. G. Barker, B. E. Causton, P. A. Baskerville, S. Gent, and J. F. Martin, "The vasa vasorum of the rabbit carotid artery," *J Anat*, vol. 180 (Pt 2), pp. 225-31, 1992.

[5] K. D. O'Brien, T. O. McDonald, A. Chait, M. D. Allen, and C. E. Alpers, "Neovascular expression of E-selectin, intercellular adhesion molecule-1, and vascular cell adhesion molecule-1 in human atherosclerosis and their relation to intimal leukocyte content," *Circulation*, vol. 93, pp. 672-82, 1996.

[6] P. R. Moreno, K. R. Purushothaman, V. Fuster, D. Echeverri, H. Truszczynska, S. K. Sharma, J. J. Badimon, and W. N. O'Connor, "Plaque neovascularization is increased in ruptured atherosclerotic lesions of human aorta: implications for plaque vulnerability," *Circulation*, vol. 110, pp. 2032-8, 2004.

[7] M. R. Hayden and S. C. Tyagi, "Vasa vasorum in plaque angiogenesis, metabolic syndrome, type 2 diabetes mellitus, and atheroscleropathy: a malignant transformation," *Cardiovasc Diabetol*, vol. 3, pp. 1, 2004.

[8] S. G. E. Barker, J. E. Beesley, P. A. Baskerville, and J. F. Martin, "The influence of the adventitia on the presence of smooth muscle cells and macrophages in the arterial intima," *European Journal of Vascular and Endovascular Surgery*, vol. 9, pp. 222-227, 1995.

[9] F. D. Kolodgie, H. K. Gold, A. P. Burke, D. R. Fowler, H. S. Kruth, D. K. Weber, A. Farb, L. J. Guerrero, M. Hayase, R. Kutys, J. Narula, A. V. Finn, and R. Virmani, "Intraplaque hemorrhage and progression of coronary atheroma," *N Engl J Med*, vol. 349, pp. 2316-25, 2003.

[10] C. M. Pitsillides, E. K. Joe, X. Wei, R. R. Anderson, and C. P. Lin, "Selective cell targeting with light-absorbing microparticles and nanoparticles," *Biophys J*, vol. 84, pp. 4023-32, 2003.

[11] J. A. Copland, M. Eghtedari, V. L. Popov, N. Kotov, N. Mamedova, M. Motamedi, and A. A. Oraevsky, "Bioconjugated gold nanoparticles as a molecular based contrast agent: implications for imaging of deep tumors using optoacoustic tomography," *Mol Imaging Biol*, vol. 6, pp. 341-9, 2004.

[12] P. Libby, "Molecular bases of the acute coronary syndromes," *Circulation*, vol. 91, pp. 2844-50, 1995.

[13] T. A. Springer, "Adhesion receptors of the immune system," *Nature*, vol. 346, pp. 425-34, 1990.

[14] M. Hoshiga, C. E. Alpers, L. L. Smith, C. M. Giachelli, and S. M. Schwartz, "Alpha-v beta-3 integrin expression in normal and atherosclerotic artery," *Circ Res*, vol. 77, pp. 1129-35, 1995.

[15] D. B. Ellegala, H. Leong-Poi, J. E. Carpenter, A. L. Klibanov, S. Kaul, M. E. Shaffrey, J. Sklenar, and J. R. Lindner, "Imaging tumor angiogenesis with contrast ultrasound and microbubbles targeted to alpha(v)beta3," *Circulation*, vol. 108, pp. 336-41, 2003.

[16] R. Haubner, W. A. Weber, A. J. Beer, E. Vabuliene, D. Reim, M. Sarbia, K. F. Becker, M. Goebel, R. Hein, H. J. Wester, H. Kessler, and M. Schwaiger, "Noninvasive visualization of the activated alphavbeta3 integrin in cancer patients by positron emission tomography and [18F]Galacto-RGD," *PLoS Med*, vol. 2, pp. e70, 2005.

[17] D. F. Meoli, M. M. Sadeghi, S. Krassilnikova, B. N. Bourke, F. J. Giordano, D. P. Dione, H. Su, D. S. Edwards, S. Liu, T. D. Harris, J. A. Madri, B. L. Zaret, and A. J. Sinusas, "Noninvasive imaging of myocardial angiogenesis following experimental myocardial infarction," *J Clin Invest*, vol. 113, pp. 1684-91, 2004.

[18] D. A. Sipkins, D. A. Cheresh, M. R. Kazemi, L. M. Nevin, M. D. Bednarski, and K. C. Li, "Detection of tumor angiogenesis in vivo by alphaVbeta3-targeted magnetic resonance imaging," *Nat Med*, vol. 4, pp. 623-6, 1998.

[19] J. C. Bamber and C. R. Hill, "Ultrasound attenuation and propagation speed in mammalian tissues as a function of temperature," *Ultrasound Med. Biol.*, vol. 5, pp. 149-157, 1979.

[20] F. A. Duck, *Physical properties of tissue: a comprehensive reference book*. London: Academic, 1990.

[21] Y. Shi, R. S. Witte, and M. O'Donnell, "Identification of vulnerable atherosclerotic plaque using IVUS-based thermal strain imaging," *IEEE Trans Ultrason Ferroelectr Freq Control*, vol. 52, pp. 844-50, 2005.

[22] Y. Shi, F. J. deAna, S. Chetcuti, and M. O'Donnell, "Motion artifact reduction for IVUS-based thermal strain imaging," *IEEE Trans Ultrason Ferroelectr Freq Control*, vol. 52, pp. 1312-1319, 2005.

Bibliography

Optical properties of aorta compiled by Steven Jacques, Oregon Medical Laser Center. http://omlc.ogi.edu/spectra/aorta/index.html.

Agah R, Pearce JA, Welch AJ, et al. Rate process model for arterial tissue thermal damage: implications on vessel photocoagulation. Lasers Surg Med. 1994;15(2):176-184.

Ahmed JM, Mintz GS, Weissman NJ, et al. Mechanism of lumen enlargement during intracoronary stent implantation: an intravascular ultrasound study. Circulation. Jul 4 2000;102(1):7-10.

Ambrose JA, Tannenbaum MA, Alexopoulos D, et al. Angiographic progression of coronary artery disease and development of myocardial infarction. J. Am. Col. Cardiol. 1998;12(1):56-62.

Anderson RR, Parrish JA. Selective photothermolysis: precise microsurgery by selective absorption of pulsed radiation. Science. Apr 29 1983;220(4596):524-527.

ANSI. American National Standard for Safe Use of Lasers, ANSI Z136.1. Orlando: Laser Institute of America; 2000.

Anvari B, Rastegar S, Motamedi M. Modeling of intraluminal heating of biological tissue: implications for treatment of benign prostatic hyperplasia. IEEE Trans Biomed Eng. Sep 1994;41(9):854-864.

Ashforth-Frost S. Quantitative thermal imaging using liquid crystals. Journal of Biomedical Optics. 1996;1:18-27.

Atkinson JB, Hoover RL, Berry KK, et al. Cholesterol-fed heterozygous watanabe heritable hyperlipidemic rabbit: A new model for Atherosclerosis. Atherosclerosis. 1989;78:123-126.

Bamber JC, Hill CR. Ultrasound attenuation and propagation speed in mammalian tissues as a function of temperature. Ultrasound Med. Biol. 1979;5(2):149-157.

Barger AC, Beeuwkes R, 3rd, Lainey LL, et al. Hypothesis: vasa vasorum and neovascularization of human coronary arteries. A possible role in the pathophysiology of atherosclerosis. N Engl J Med. Jan 19 1984;310(3):175-177.

Barker SG, Causton BE, Baskerville PA, et al. The vasa vasorum of the rabbit carotid artery. J Anat. Apr 1992;180 (Pt 2):225-231.

Barker SGE, Beesley JE, Baskerville PA, et al. The influence of the adventitia on the presence of smooth muscle cells and macrophages in the arterial intima. European Journal of Vascular and Endovascular Surgery. 1995;9(2):222-227.

Beard PC, Mills TN. Characterization of post mortem arterial tissue using time-resolved photoacoustic spectroscopy at 436, 461 and 532 nm. Phys Med Biol. Jan 1997;42(1):177-198.

Bell AG. art. XXXIV on the production and reproduction of sound by light. Am. J. Sci. 1880;20:305-324.

Bell AG. On the production and reproduction of sound by light. Am. J. Sci. 1880;20:305-324.

Bowen T, Connor WG, Nasoni RL, et al. Measurement of the temperature dependence of the velocity of ultrasound in soft tissues. Ultrasonic Tissue Characterization II. 1979;Spec Publ 525:57-61.

Brennan JF, 3rd, Romer TJ, Lees RS, et al. Determination of human coronary artery composition by Raman spectroscopy. Circulation. Jul 1 1997;96(1):99-105.

Bush NL, Rivens I, ter Haar GR, et al. Acoustic properties of lesions generated with an ultrasound therapy system. Ultrasound Med Biol. 1993;19(9):789-801.

Casscells W, Hathorn B, David M, et al. Thermal detection of cellular infiltrates in living atherosclerotic plaques: possible implications for plaque rupture and thrombosis. Lancet. May 25 1996;347(9013):1447-1451.

Chandrasekhar S. Radiative transfer. New York: Dover; 1960.

Chen QX, Davies A, Dewhurst RJ, et al. Photo-acoustic probe for intra-arterial imaging and therapy. Electron. Lett. 1993;29:1632-1633.

Cheong W, Prahl SA, Welch AJ. A review of optical properties of biological tissue. IEEE J. Quantum Electronics. 1990;26:2166-2183.

Choi B, Pearce JA, Welch AJ. Modelling infrared temperature measurements: implications for laser irradiation and cryogen cooling studies. Phys Med Biol. Feb 2000;45(2):541-557.

Choi B, Welch AJ. Analysis of thermal relaxation during laser irradiation of tissue. Lasers Surg Med. 2001;29(4):351-359.

Cohn NA, Emelianov SY, Lubinski MA, et al. An Elasticity Microscope. Part 1: Methods. IEEE Trans Ultrason Ferroelectr Freq Control. 1997;44(6):1304-1319.

Copland JA, Eghtedari M, Popov VL, et al. Bioconjugated gold nanoparticles as a molecular based contrast agent: implications for imaging of deep tumors using optoacoustic tomography. Mol Imaging Biol. Sep-Oct 2004;6(5):341-349.

Cotran RS, Kumar V, Robbins SL, et al. Inflammation and repair. Pathologic basis of disease. Philadelphia: WB Saunders Company; 1994:51-93.

Cragg AH, Einzig S, Rysavy JA, et al. The vasa vasorum and angioplasty. Radiology. Jul 1983;148(1):75-80.

Crotty TP. The role of vasa vasorum in atherosclerosis. Med Hypotheses. Apr 1989;28(4):233-243.

Cybulsky MI, Gimbrone MA, Jr. Endothelial expression of a mononuclear leukocyte adhesion molecule during atherogenesis. Science. Feb 15 1991;251(4995):788-791.

Daley SJ, Herderick E, Cornhill JF, et al. Cholesterol-fed and casein-fed rabbit models of atherosclerosis. Part 1: Differing lesion area of volume despite equal plasma cholesterol levels. Arteroscler. Thromb. 1994;14:95-104.

Daley SJ, Herderick E, Cornhill JF, et al. Cholesterol-fed and casein-fed rabbit models of atherosclerosis. Part 2: Differing lesion area of volume despite equal plasma cholesterol levels. Arteroscler. Thromb. 1994;14:105-114.

Damianou CA, Sanghvi NT, Fry FJ, et al. Dependence of ultrasonic attenuation and absorption in dog soft tissues on temperature and thermal dose. J Acoust Soc Am. Jul 1997;102(1):628-634.

Davies MJ. A macro and micro view of coronary vascular insult in ischemic heart disease. Circulation. Sep 1990;82(3 Suppl):II38-46.

Davies MJ. The pathophysiology of acute coronary syndromes. Heart. Mar 2000;83(3):361-366.

de Korte CL, Pasterkamp G, van der Steen AF, et al. Characterization of plaque components with intravascular ultrasound elastography in human femoral and coronary arteries in vitro. Circulation. Aug 8 2000;102(6):617-623.

Diamantopoulos L. Arterial wall thermography. J Interv Cardiol. Jun 2003;16(3):261-266.

Diamantopoulos L, Liu X, De Scheerder I, et al. The effect of reduced blood-flow on the coronary wall temperature. Are significant lesions suitable for intravascular thermography? Eur Heart J. Oct 2003;24(19):1788-1795.

Duck FA. Physical properties of tissue: a comprehensive reference book. London: Academic; 1990.

Ellegala DB, Leong-Poi H, Carpenter JE, et al. Imaging tumor angiogenesis with contrast ultrasound and microbubbles targeted to alpha(v)beta3. Circulation. Jul 22 2003;108(3):336-341.

Emelianov SY, Aglyamov SR, Karpiouk AB, et al. Synergy and applications of combined ultrasound, elasticity and photoacoustic imaging. Proceedings of the 2006 IEEE International Ultrasonics Symposium. 2006:405-415.

Emelianov SY, Aglyamov SR, Shah J, et al. Combined ultrasound, optoacoustic and elasticity imaging. Proceedings of the 2004 SPIE Photonics West Symposium: Photons Plus Ultrasound: Imaging and Sensing. 2004;5320:101-112.

Eriksson EE, Xie X, Werr J, et al. Importance of primary capture and L-selectin-dependent secondary capture in leukocyte accumulation in inflammation and atherosclerosis in vivo. J Exp Med. Jul 16 2001;194(2):205-218.

Falk E, Shah PK, Fuster V. Coronary plaque disruption. Circulation. 1995;92(3):657-671.

Fayad ZA, Fuster V. Clinical imaging of the high-risk or vulnerable atherosclerotic plaque. Circ Res. Aug 17 2001;89(4):305-316.

Fitzgerald PJ, Yock PG. Mechanisms and outcomes of angioplasty and atherectomy assessed by intravascular ultrasound imaging. J Clin Ultrasound. Nov-Dec 1993;21(9):579-588.

Flock ST, Patterson MS, Wilson BC, et al. Monte Carlo modeling of light propagation in highly scattering tissue--I: Model predictions and comparison with diffusion theory. IEEE Trans Biomed Eng. Dec 1989;36(12):1162-1168.

Fromageau J, Brusseau E, Vray D, et al. Characterization of PVA cryogel for intravascular ultrasound elasticity imaging. IEEE Trans Ultrason Ferroelectr Freq Control. Oct 2003;50(10):1318-1324.

Fujimoto JG, Boppart SA, Tearney GJ, et al. High resolution in vivo intra-arterial imaging with optical coherence tomography. Heart. Aug 1999;82(2):128-133.

Fung YC. Biomechanics: Mechanical properties of living tissues. 2nd ed. New York: Springer-Verlag; 1993.

Fuster V. Lewis A. Conner Memorial Lecture. Mechanisms leading to myocardial infarction: insights from studies of vascular biology. Circulation. Oct 1994;90(4):2126-2146.

Grattan KTV, Zhang ZY. Fiber optic fluoresccence thermometry. London: Chapman & Hall; 1995.

Guyton JR, Klemp KF. Early extracellular lipid deposits in aorta of cholesterol-fed rabbits. Am. J. Pathol. 1992;141:925-936.

Hale GM, Querry MR. Optical constants of water in 200nm to 2000nm wavelength region. Appl. Opt. 1973;12(3):555-563.

Hansson GK. Immune mechanisms in atherosclerosis. Arterioscler Thromb Vasc Biol. Dec 2001;21(12):1876-1890.

Hassan CM, Peppas NA. Structure and applications of poly(vinyl alcohol) hydrogels produced by conventional crosslinking or by freezing/thawing methods. Advances in polymer science. 2000;153:37-65.

Haubner R, Weber WA, Beer AJ, et al. Noninvasive visualization of the activated alphavbeta3 integrin in cancer patients by positron emission tomography and [18F]Galacto-RGD. PLoS Med. Mar 2005;2(3):e70.

Hayakawa K, Takeda S, Kawabe K, et al. Acoustic Characteristics of PVA Gel. Proc. IEEE Ultrason. Symp. 1989:969-972.

Hayden MR, Tyagi SC. Vasa vasorum in plaque angiogenesis, metabolic syndrome, type 2 diabetes mellitus, and atheroscleropathy: a malignant transformation. Cardiovasc Diabetol. Feb 4 2004;3:1.

Henrichs PM, Meador JW, Fuqua JM, et al. Atherosclerotic plaque characterization with optoacoustic imaging. Proceedings of the 2005 SPIE Photonics West Symposium: Photons Plus Ultrasound: Imaging and Sensing. 2005;5697:217-223.

Henriques FC, Moritz AR. Studies in thermal injury I. The conduction of heat to and through skin and the temperature attained therein. A theroretical and an experimental investigation. Am. J. Pathol. 1947;23:531-549.

Hoelen CGA, de Mul FFM, Pongers R, et al. Three-dimensional photoacoustic imaging of blood vessels in tissue. Optics Letters. 1998;23(8):648-650.

Hoshiga M, Alpers CE, Smith LL, et al. Alpha-v beta-3 integrin expression in normal and atherosclerotic artery. Circ Res. Dec 1995;77(6):1129-1135.

Itoh A, Miyazaki S, Nonogi H, et al. Angioscopic prediction of successful dilatation and of restenosis in percutaneous transluminal coronary angioplasty. Significance of yellow plaque. Circulation. Mar 1 1995;91(5):1389-1396.

Jacques SL. Role of tissue optics and pulse duration on tissue effects during high-power laser irradiation. Journal of applied optics. 1993;32(13).

Jacques SL, Wang LV. Monte Carlo modelling of light transport in tissues. In: Welch AJ, van Gemert MJ, eds. Optical-Thermal Response of Laser-Irradiated Tissue. Newyork: Plenum; 1995:73-100.

Janeway CA, Jr., Medzhitov R. Innate immune recognition. Annu Rev Immunol. 2002;20:197-216.

Jonasson L, Holm J, Skalli O, et al. Regional accumulations of T cells, macrophages, and smooth muscle cells in the human atherosclerotic plaque. Arteriosclerosis. Mar-Apr 1986;6(2):131-138.

Keijzer M, Jacques SL, Prahl SA, et al. Light distributions in artery tissue: Monte Carlo simulations for finite-diameter laser beams. Lasers Surg Med. 1989;9(2):148-154.

Keijzer M, Richards-Kortum RR, Jacques SL, et al. Fluorescence spectroscopy of turbid media: autofluorescence of the human aorta. Applied Optics. 1989;28:4286-4292.

Kharine A, Manohar S, Seeton R, et al. Poly(vinyl alcohol) gels for use as tissue phantoms in photoacoustic mammography. Phys Med Biol. Feb 7 2003;48(3):357-370.

Kolkman RGM, Hondebrink E, Steenbergen W, et al. In vivo photoacoustic imaging of blood vessels using an extreme-narrow aperture sensor. IEEE Journal of Selected Topics in Quantum Electronics. 2003;9(2):343-346.

Kolodgie FD, Gold HK, Burke AP, et al. Intraplaque hemorrhage and progression of coronary atheroma. N Engl J Med. Dec 11 2003;349(24):2316-2325.

Komiyama N, Berry GJ, Kolz ML, et al. Tissue characterization of atherosclerotic plaques by intravascular ultrasound radiofrequency signal analysis: an in vitro study of human coronary arteries. Am Heart J. Oct 2000;140(4):565-574.

Korte CLd, Sierevogel MJ, Mastik F, et al. Identification of Atherosclerotic Plaque Components With Intravascular Ultrasound Elastography In Vivo - A Yucatan Pig Study. Circulation. 2002;105:1627-1630.

Koyama H, Raines EW, Bornfeldt KE, et al. Fibrillar collagen inhibits arterial smooth muscle proliferation through regulation of Cdk2 inhibitors. Cell. Dec 13 1996;87(6):1069-1078.

Kritharides L, Brieger D, Freedman SB, et al. Treatment of vulnerable plaques - current and future strategies. In: Khachigian LM, ed. High risk atherosclerotic plaques - mechanisms, imaging, models and therapy. New York: CRC Press; 2004.

Kruger RA, Reinecke DR, Kruger GA. Thermoacoustic computed tomography--technical considerations. Med Phys. Sep 1999;26(9):1832-1837.

Ku G, Wang LV. Scanning thermoacoustic tomography in biological tissue. Med Phys. May 2000;27(5):1195-1202.

Larose E, Yeghiazarians Y, Libby P, et al. Characterization of human atherosclerotic plaques by intravascular magnetic resonance imaging. Circulation. Oct 11 2005;112(15):2324-2331.

Leiner T, Gerretsen S, Botnar R, et al. Magnetic resonance imaging of atherosclerosis. Eur Radiol. Jun 2005;15(6):1087-1099.

Leitinger N. Oxidized phospholipids as modulators of inflammation in atherosclerosis. Curr Opin Lipidol. Oct 2003;14(5):421-430.

Lemons RA, Quate CF. Acoustic microscope-scanning version. Amer. Phys. Lett. 1974;24(4):163-165.

Libby P. Molecular bases of the acute coronary syndromes. Circulation. Jun 1 1995;91(11):2844-2850.

Libby P. Current Concepts of the Pathogenesis of the Acute Coronary Syndromes. Circulation. July 17, 2001 2001;104(3):365-372.

Libby P. Inflammation in atherosclerosis. Nature. Dec 19-26 2002;420(6917):868-874.

Libby P, Ridker PM, Maseri A. Inflammation and atherosclerosis. Circulation. Mar 5 2002;105(9):1135-1143.

Libby P, Ross R. Cytokines and growth regulatory molecules. In: Fuster V, Ross R, Topol EJ, eds. Atherosclerosis and coronary artery disease. Vol 1. Philadelphia: Lippincott-Raven; 1996:585-594.

Little WC, Constantinescu M, Applegate RJ, et al. Can coronary angiography predict the site of a subsequent myocardial infarction in patients with mild-to-moderate coronary artery disease? Circulation. Nov 1988;78(5 Pt 1):1157-1166.

Lubinski MA, Emelianov SY, O'Donnell M. Cross-correlation speckle tracking techniques for ultrasound elasticity imaging. IEEE Transactions on Ultrasonics, Ferroelectrics and Frequency Control. 1999;46:82-96.

Maass-Moreno R, Damianou CA. Noninvasive temperature estimation in tissue via ultrasound echo-shifts. Part 1. Analytical Model. J Acoust. Soc. Amer. 1996;100:2514-2521.

MacNeill BD, Lowe HC, Takano M, et al. Intravascular modalities for detection of vulnerable plaque: current status. Arterioscler Thromb Vasc Biol. Aug 1 2003;23(8):1333-1342.

Mahadevan-Jansen A, Follen MM, Ramanujam M, et al. Development of a fiber-optic probe to measure NIR Raman spectra of cervical tissue in vivo. Photochemistry and Photobiology. 1998;68(3):427-431.

Meoli DF, Sadeghi MM, Krassilnikova S, et al. Noninvasive imaging of myocardial angiogenesis following experimental myocardial infarction. J Clin Invest. Jun 2004;113(12):1684-1691.

Moreno PR, Falk E, Palacios IF, et al. Macrophage infiltration in acute coronary syndromes. Implications for plaque rupture. Circulation. Aug 1994;90(2):775-778.

Moreno PR, Purushothaman KR, Fuster V, et al. Plaque neovascularization is increased in ruptured atherosclerotic lesions of human aorta: implications for plaque vulnerability. Circulation. Oct 5 2004;110(14):2032-2038.

Naghavi M, Libby P, Falk E, et al. From vulnerable plaque to vulnerable patient: a call for new definitions and risk assessment strategies: Part I. Circulation. Oct 7 2003;108(14):1664-1672.

Nasoni RL, Bowen T. Ultrasound speed as a parameter for noninvasive thermometry. Noninvasive temperature measurement. 1989:95-107.

Niederhauser JJ, Jaeger M, Frenz M. Comparison of lsaer-induced and classical ultrasound. Proceedings of the SPIE The International Society for Optical Engineering. 2003;4960:118-123.

Nissen SE, Yock P. Intravascular Ultrasound : Novel Pathophysiological Insights and Current Clinical Applications. Circulation. January 30, 2001 2001;103(4):604-616.

O'Brien KD, McDonald TO, Chait A, et al. Neovascular expression of E-selectin, intercellular adhesion molecule-1, and vascular cell adhesion molecule-1 in human atherosclerosis and their relation to intimal leukocyte content. Circulation. Feb 15 1996;93(4):672-682.

O'Donnell M, Skovoroda AR, Shapo BM, et al. Internal displacement and strain imaging using ultrasonic speckle tracking. IEEE Transactions on Ultrasonics,Ferroelectrics and Frequency Control. 1994;41:314-325.

Oraevsky AA, Jacques SL, Pettit GH, et al. XeCl laser-induced fluorescence of atherosclerotic arteries. Spectral similarities between lipid-rich lesions and peroxidized lipoproteins. Circ Res. Jan 1993;72(1):84-90.

Oraevsky AA, Jacques SL, Tittel FK. Measurement of tissue optical properties by time-resolved detection of laser-induced transient stress. Appl. Opt. 1997;36:402-415.

Oraevsky AA, Jacques SL, Tittle FK. Determination of tissue optical properties by time-resolved detection of laser-induced stress waves. Paper presented at: Proc. of SPIE, 1993.

Oraevsky AA, Karabutov AA. Optoacoustic Tomography. In: Vo-Dinh T, ed. Biomedical Photonics Handbook: CRC Press; 2003:34-31 - 34-34.

Oraevsky AA, Karabutov AA, Solomatin SV, et al. Laser optoacoustic imaging of breast cancer in vivo. Biomedical Optoacoustics II in the Proceedings of the SPIE. 2001;4256:6-15.

Oraevsky AA, Letokhov VS, Ragimov SE, et al. Spectral properties of human atherosclerotic blood vessel walls. Laser Life Sci. 1988;2:275-288.

Overturf M, Loose-Mitchell D. In vivo model system: the choice of experimental model for analysis of lipoproteins and atherosclerosis. Curr. Opin. Lipidology. 1992;3:179-185.

Overturf M, Sybers H, Schapers J, et al. Hypertension and atherosclerosis in cholesterol-fed rabbits. Part 1. Mild, two kidney one-clip goldblatt hypertension treated with enlapril. Atherosclerosis. 1986;59:283-299.

Pasterkamp G, Falk E, Woutman H, et al. Techniques characterizing the coronary atherosclerotic plaque: influence on clinical decision making? J Am Coll Cardiol. Jul 2000;36(1):13-21.

Pearce J, Thomsen S. Rate process analysis of thermal damage. In: Welch AJ, van Gemert MJ, eds. Optical-thermal response of laser-irradiated tissue. New York: Plenum Press; 1995.

Pitsillides CM, Joe EK, Wei X, et al. Selective cell targeting with light-absorbing microparticles and nanoparticles. Biophys J. Jun 2003;84(6):4023-4032.

Prahl SA. The diffusion approximation in three dimensions. In: Welch AJ, van Gemert MJ, eds. Optical-Thermal Response of Laser-Irradiated Tissue. Newyork: Plenum; 1995:207-231.

Prahl SA. Optical Properties Spectra compiled by Scott Prahl. Oregon Medical Laser Center. Available at: http://omlc.ogi.edu/spectra/.

Prahl SA, Keijzer M, Jacques SL, et al. Monte Carlo model of light propagation in tissue. SPIE Proceedings of Dosimetry of Laser Radiation in Medicine and Biology. 1989;IS 5:102-111.

Prati F, Arbustini E, Labellarte A, et al. Correlation between high frequency intravascular ultrasound and histomorphology in human coronary arteries. Heart. May 2001;85(5):567-570.

Prince MR, Deutsch TF, Mathews-Roth MM, et al. Preferential light absorption in atheromas in vitro. Implications for laser angioplasty. J Clin Invest. Jul 1986;78(1):295-302.

Raines EW, Rosenfeld ME, Ross R. The role of macrophages. In: Fuster V, Ross R, Topol EJ, eds. Atherosclerosis and coronary artery disease. Vol 1. Philadelphia: Lippincott-Raven; 1996:539-555.

Rajagopalan B, Greenleaf JF, Thomas PJ, et al. Variation of acoustic speed with temperature in various excised human tissues studied by ultrasound computerized tomography. Ultrasonic tissue characterization II. 1979;Spec Publ 525:227-233.

Rekhter MD. Collagen synthesis in atherosclerosis: too much and not enough. Cardiovasc Res. Feb 1999;41(2):376-384.

Ribault M, Chapelon JY, Cathignol D, et al. Differential attenuation imaging for the characterization of high intensity focused ultrasound lesions. Ultrason Imaging. Jul 1998;20(3):160-177.

Roald HE, Lyberg T, Dedichen H, et al. Collagen-induced thrombus formation in flowing nonanticoagulated human blood from habitual smokers and nonsmoking patients with severe peripheral atherosclerotic disease. Arterioscler Thromb Vasc Biol. Jan 1995;15(1):128-132.

Rocnik EF, Chan BM, Pickering JG. Evidence for a role of collagen synthesis in arterial smooth muscle cell migration. J Clin Invest. May 1 1998;101(9):1889-1898.

Roider J, Birngruber B. Solution of the heat conduction equation. In: Welch AJ, van Gemert MJ, eds. Optical-Thermal Response of Laser-Irradiated Tissue. New York: Plenum; 1995.

Romer TJ, Brennan JF, 3rd, Puppels GJ, et al. Intravascular ultrasound combined with Raman spectroscopy to localize and quantify cholesterol and calcium salts in atherosclerotic coronary arteries. Arterioscler Thromb Vasc Biol. Feb 2000;20(2):478-483.

Rosamond W, Flegal K, Friday G, et al. Heart Disease and Stroke Statistics--2007 Update: A Report From the American Heart Association Statistics Committee and

Stroke Statistics Subcommittee. Circulation. February 6, 2007 2007;115(5):e69-171.

Rosenfeld ME, Chait A, Bierman EL, et al. Lipid composition of aorta of Watanabe heritable hyperlipemic and comparably hypercholesterolemic fat-fed rabbits. Plasma lipid composition determines aortic lipid composition of hypercholesterolemic rabbits. Arteriosclerosis. Jul-Aug 1988;8(4):338-347.

Ross R. The pathogenesis of atherosclerosis: a perspective for the 1990's. Nature. 1993;362:801-809.

Ross R. Atherosclerosis--an inflammatory disease. N Engl J Med. Jan 14 1999;340(2):115-126.

Ross R, Glomset JA. Atherosclerosis and the arterial smooth muscle cell: Proliferation of smooth muscle is a key event in the genesis of the lesions of atherosclerosis. Science. Jun 29 1973;180(93):1332-1339.

Sagi A, Shitzer A, Katzir A, et al. Heating of biological tissue by laser irradiation: Theoretical model. Opt Eng. 1992;31(7):1417-1424.

Schwartz CJ, Mitchell JR. Cellular infiltration of the human arterial adventitia associated with atheromatous plaques. Circulation. Jul 1962;26:73-78.

Schwarzacher SP, Fitzgerald PJ, Yock PG. Clinical use of intravascular ultrasound. Semin Interv Cardiol. Mar 1997;2(1):1-9.

Seip R, Ebbini ES. Noninvasive estimation of tissue temperature response to heating fields using diagnostic ultrasound. IEEE Trans Biomed Eng. 1995;42:828-839.

Seip R, VanBaren P, Cain C, et al. Noninvasive spatio-temporal temperature change estimation using diagnostic ultrasound. IEEE Trans Ultrason Ferroelectr Freq Control. 1996;43:1068-1078.

Sethuraman S, Aglyamov SR, Amirian JH, et al. Intravascular photoacoustic imaging to detect and differentiate atherosclerotic plaques. Proceedings of the 2005 IEEE International Ultrasonics Symposium. 2005:133-136.

Sethuraman S, Aglyamov SR, Amirian JH, et al. Development of a combined intravascular ultrasound and photoacoustic imaging system. Proceedings of the 2006 SPIE Photonics West Symposium: Photons Plus Ultrasound: Imaging and Sensing. 2006;6086:F1-F10.

Sethuraman S, Aglyamov SR, Amirian JH, et al. Development of a combined intravascular ultrasound and photoacoustic imaging system. In: Oraevsky AA, Wang LV, eds. Photons Plus Ultrasound: Imaging and Sensing 2006: The Seventh

Conference on Biomedical Thermoacoustics, Optoacoustics, and Acousto-optics. Vol 6086; 2006:F1-F10.

Sethuraman S, Aglyamov SR, Amirian JH, et al. Intravascular Photoacoustic Imaging Using an IVUS Imaging Catheter. IEEE Transactions on Ultrasonics Ferroelectrics, and Frequency Control. 2007;54(5):978-986.

Sethuraman S, Mallidi S, Aglyamov SR, et al. Intravascular photoacoustic imaging of atherosclerotic plaques: ex vivo study using a rabbit model of atherosclerosis. In: Oraevsky AA, Wang LV, eds. Photons Plus Ultrasound: Imaging and Sensing 2007: The Eighth Conference on Biomedical Thermoacoustics, Optoacoustics and Acousto-Optics. Vol 6437; 2007:6437291-6437299.

Shah PK. Mechanisms of plaque vulnerability and rupture. J Am Coll Cardiol. Feb 19 2003;41(4 Suppl S):15S-22S.

Shi Y, deAna FJ, Chetcuti S, et al. Motion artifact reduction for IVUS-based thermal strain imaging. IEEE Trans Ultrason Ferroelectr Freq Control. 2005;52(8):1312-1319.

Shi Y, Witte RS, O'Donnell M. Identification of vulnerable atherosclerotic plaque using IVUS-based thermal strain imaging. IEEE Trans Ultrason Ferroelectr Freq Control. May 2005;52(5):844-850.

Simon C, vanBaren P, Ebbini ES. Two-dimensional temperature estimation using diagnostic ultrasound. IEEE Trans Ultrason Ferroelectr Freq Control. 1998;45(4):1088-1099.

Siphanto RI, Thumma KK, Kolkman RGM, et al. Serial noninvasive photoacoustic imaging of neovascularization in tumor angiogenesis. Optics Express. 2004;13(1):89-95.

Sipkins DA, Cheresh DA, Kazemi MR, et al. Detection of tumor angiogenesis in vivo by alphaVbeta3-targeted magnetic resonance imaging. Nat Med. May 1998;4(5):623-626.

Skalen K, Gustafsson M, Rydberg EK, et al. Subendothelial retention of atherogenic lipoproteins in early atherosclerosis. Nature. Jun 13 2002;417(6890):750-754.

Springer TA. Adhesion receptors of the immune system. Nature. Aug 2 1990;346(6283):425-434.

Stary HC. Natural history and histological classification of atherosclerotic lesions: an update. Arterioscler Thromb Vasc Biol. May 2000;20(5):1177-1178.

Stary HC, Chandler AB, Dinsmore RE, et al. A definition of advanced types of atherosclerotic lesions and a histological classification of atherosclerosis. A report from the Committee on Vascular Lesions of the Council on Arteriosclerosis, American Heart Association. Circulation. Sep 1 1995;92(5):1355-1374.

Stary HC, Chandler AB, Glagov S, et al. A definition of initial, fatty streak, and intermediate lesions of atherosclerosis. A report from the Committee on Vascular Lesions of the Council on Arteriosclerosis, American Heart Association. Circulation. May 1994;89(5):2462-2478.

Stefanadis C, Diamantopoulos L, Dernellis J, et al. Heat production of atherosclerotic plaques and inflammation assessed by the acute phase proteins in acute coronary syndromes. J Mol Cell Cardiol. Jan 2000;32(1):43-52.

Stefanadis C, Diamantopoulos L, Vlachopoulos C, et al. Thermal heterogeneity within human atherosclerotic coronary arteries detected in vivo: A new method of detection by application of a special thermography catheter. Circulation. Apr 20 1999;99(15):1965-1971.

Stefanadis C, Toutouzas K, Tsiamis E, et al. Thermal heterogeneity in stable human coronary atherosclerotic plaques is underestimated in vivo: the "cooling effect" of blood flow. J Am Coll Cardiol. Feb 5 2003;41(3):403-408.

Stefanadis C, Vavuranakis M, Toutouzas P. Vulnerable plaque: the challenge to identify and treat it. J Interv Cardiol. Jun 2003;16(3):273-280.

Straube WL, Arthur RM. Theoretical estimation of the temperature dependence of backscattered ultrasonic power for noninvasive thermometry. Ultrasound Med Biol. 1994;20(9):915-922.

Sun Z, Ying H. A multi-gate time-of-flight technique for estimation of temperature distribution in heated tissue: theory and computer simulation. Ultrasonics. Feb 1999;37(2):107-122.

Sundararajan PR. Poly(vinyl alcohol). In: Mark JE, ed. Polymer data handbook. New York: Oxford University Press Inc.; 1999:891-892.

Surry KJ, Austin HJ, Fenster A, et al. Poly(vinyl alcohol) cryogel phantoms for use in ultrasound and MR imaging. Phys Med Biol. Dec 21 2004;49(24):5529-5546.

Techavipoo U, Varghese T, Zagzebski JA, et al. Temperature dependence of ultrasonic propagation speed and attenuation in canine tissue. Ultrason Imaging. Oct 2002;24(4):246-260.

Tromberg BJ, Shah N, Lanning R, et al. Non-invasive in vivo characterization of breast tumors using photon migration spectroscopy. Neoplasia. 2000;2(1-2):26-40.

Uchida Y, Nakamura F, Tomaru T, et al. Prediction of acute coronary syndromes by percutaneous coronary angioscopy in patients with stable angina. Am Heart J. Aug 1995;130(2):195-203.

Valvano JW, Chitsabesan B. Thermal conductivity and diffusivity of arterial wall and atherosclerotic plaque. Lasers Life Sci. 1987;1:219-229.

Valvano JW, Pearce J. Temperature measurements. In: Welch AJ, van Gemert MJ, eds. Optical-thermal response of laser-irradiated tissue. New York: Plenum; 1995.

van der Wal AC, Becker AE, van der Loos CM, et al. Site of intimal rupture or erosion of thrombosed coronary atherosclerotic plaques is characterized by an inflammatory process irrespective of the dominant plaque morphology. Circulation. Jan 1994;89(1):36-44.

van Gemert MJ, Verdaasdonk R, Stassen EG, et al. Optical properties of human blood vessel wall and plaque. Lasers Surg Med. 1985;5(3):235-237.

van Gemert MJC, Verdaasdonk R, Stassen EG, et al. Optical properties of human blood vessel wall and plaque. Lasers Surg Med. 1985;5(3):235-237.

van Gemert MJC, Welch AJ, Jacques SL, et al. Light distribution, optical properties, and cardiovascular tissues. In: Abela GS, ed. Lasers in cardiovascular medicine and surgery: Fundamentals and techniques. Norwell, MA: Kluwer Academic Publishers; 1990.

van Veen RLP, Sterenborg HJCM, Pifferi A, et al. Determination of visible near-IR absorption coefficients of mammalian fat using time- and spatially resolved diffuse reflectance and transmission spectroscopy. Journal of Biomedical Optics. 2005;**10**(5):0540041-0540046.

van Veen RLPaS, H.J.C.M., Pifferi A, Torricelli A, et al. Determination of visible near-IR absorption coefficients of mammalian fat using time- and spatially resolved diffuse reflectance and transmission spectroscopy. Journal of Biomedical Optics. 2005;10(5):0540041-0540046.

Varghese T, Daniels MJ. Real-time calibration of temperature estimates during radiofrequency ablation. Ultrason Imaging. Jul 2004;26(3):185-200.

Varghese T, Zagzebski JA, Chen Q, et al. Ultrasound monitoring of temperature change during radiofrequency ablation: preliminary in-vivo results. Ultrasound Med Biol. Mar 2002;28(3):321-329.

Viator JA, Choi B, Ambrose M, et al. In vivo port-wine stain depth determination with a photoacoustic probe. Applied Optics. 2003;42(16):3215-3224.

Virmani R, Burke AP, Kolodgie FD, et al. Pathology of the thin-cap fibroatheroma: a type of vulnerable plaque. J Interv Cardiol. Jun 2003;16(3):267-272.

Virmani R, Kolodgie FD, Burke AP, et al. Lessons from sudden coronary death: a comprehensive morphological classification scheme for atherosclerotic lesions. Arterioscler Thromb Vasc Biol. May 2000;20(5):1262-1275.

Vogel A, Venugopalan V. Mechanisms of pulsed laser ablation of biological tissues. Chem Rev. Feb 2003;**103**(2):577-644.

Wang LV, Jacques SL. Monte Carlo modeling of photon transport in multi-layered tissues. Computer Methods and Programs in Biomedicine. 1995;47:131-146.

Wang X, Pang Y, Ku G, et al. Noninvasive laser-induced photoacoustic tomography for structural and functional in vivo imaging of the brain. Nat Biotechnol. Jul 2003;21(7):803-806.

Wang X, Pang YJ, Ku G, et al. Three-dimensional laser-induced photoacoustic tomography. Optics Letters. 2003;28(19):1739-1741.

Welch AJ. The thermal response of laser irradiated tissue. IEEE J. Quantum Electronics. 1984;QE-20(12):1471-1481.

Wesley RB, 2nd, Meng X, Godin D, et al. Extracellular matrix modulates macrophage functions characteristic to atheroma: collagen type I enhances acquisition of resident macrophage traits by human peripheral blood monocytes in vitro. Arterioscler Thromb Vasc Biol. Mar 1998;18(3):432-440.

Wlodarczyk W, Hentschel M, Wust P, et al. Comparison of four magnetic resonance methods for mapping small temperature changes. Phys Med Biol. Feb 1999;44(2):607-624.

Xu M, Wang LV. Time-domain reconstruction of thermoacoustic tomography in a spherical geometry. IEEE Transactions on Medical Imaging. 2002;21:814-822.

Yabushita H, Bouma BE, Houser SL, et al. Characterization of human atherosclerosis by optical coherence tomography. Circulation. Sep 24 2002;106(13):1640-1645.

Zohdy MJ, Tse C, Ye J, et al. Acoustic estimation of thermal distribution in the vicinity of femtosecond laser-induced optical breakdown. IEEE Trans on Biomedical Engineering. 2006;53(11):2347-2355.

Vita

Shriram Sethuraman was born to Mrs. B.S. Banu and Mr. R. Sethuraman, Tiruchirapalli, India on March 4, 1979. He attended the Birla Institute of Technology and Science, Pilani, India (1996-2001) and received his undergraduate dual degrees in Biological Sciences and Electronics and Instrumentation. Shriram received a masters degree in Biomedical Engineering from The University of Texas at Austin in 2003. During this period, he worked on optical coherence tomography for the detection of atherosclerotic plaques. In the summer of 2002, he completed an internship at The University of Maryland Medical System, Baltimore, Maryland.

For his doctoral studies at The University of Texas at Austin (2003-2007), Shriram concentrated on a multi-modality imaging approach for the detection of atherosclerotic disease. His work in intravascular imaging involved combining ultrasound and photoacoustic imaging techniques. The results of his work were presented at 8 international conferences. He wrote 4 first-author publications and was a contributor to a few other articles. He was a recipient of the best Teaching Assistant Award in the Department of Biomedical Engineering (2004) and the University Continuing Fellowship (2006-2007) at The University of Texas at Austin.

Permanent address: 30/31 VGP Avenue
Dr. Seethapathy Nagar, Velachery
Chennai – 600042, India.

This dissertation was typed by Shriram Sethuraman.